ALMA MATER STUDIORUM · UNIVERSITÀ DI BOLOGNA

SCUOLA DI SCIENZE

Dipartimento di Fisica e Astronomia "Augusto Righi"

Corso di Laurea Magistrale in Astrofisica e Cosmologia

The THESEUS mission and the XGIS instrument: verification of the scientific requirements with testing of the first ORION front-end electronics prototypes

Relatore:

Prof. Cristian Vignali

Candidato:

Edoardo Borciani

Correlatori:

Dr. Ezequiel J. Marchesini
Dr. Claudio Labanti
Dr. Riccardo Campana

Anno Accademico 2022-2023

I Appello

Abstract

The *Transient High-Energy Sky and Early Universe Surveyor*, THESEUS, is a proposed space mission developed by a large European collaboration, submitted in 2016 to theEuropean Space Agency (ESA), for the M5 call within the Cosmic Vision Program. In 2018, THESEUS, along with other two mission concepts, was selected by ESA for a 3-year Phase A assessment study, but in 2021 it was not selected for launch. However, THESEUS has been re-proposed in 2022 for the M7 call. Currently, it has just concluded the preliminary phase 0, which included the CDF (Concurrent Design Facility) study, and is pending for the ESA decision for admission to the next phases of the selection.

THESEUS will provide a wide and deep sky monitoring in a very broad energy band (0.3 keV – 10 MeV), focusing capabilities in the soft X-ray band, large grasp (the product of effective area and FoV) and high positional accuracy ($\leq$2 arcmin in the 0.3–5 keV band), with on board near-IR capabilities for immediate transient identification, arcsecond localization, and redshift determination; furthermore, it will provide a high-degree of spacecraft autonomy and agility, along with the capability of promptly transmitting to ground transient trigger information. The instruments onboard THESEUS are XGIS (*X-Gamma rays Imaging Spectrometer*), a set of two coded-mask monitor cameras using monolithic SDD (Silicon Drift Device) and CsI(Tl) scintillator-based X-ray and gamma-ray detectors dedicated to the detection of Gamma-ray bursts (GRB), performing imaging up to 150 keV and spectroscopy up to 10 MeV; SXI (*Soft X-ray Imager*), two lobster-eye monitors dedicated to the follow-up in soft X-ray and imaging after the detection of XGIS; and IRT (*InfraRed Telescope*) with imaging and spectroscopy capabilities dedicated to the follow-up in the infrared waveband and the measure of the redshift of the GRB.

In this thesis we characterized the first prototypes of the ORION ASIC (*Application Specific Integrated Circuit*), a multi-chip readout circuit designed for XGIS. In particular my work concerns the characterization of two detector prototypes with ORION, to test if they are compliant with the official ESA requirements; these prototypes are thought to maximize the scientific production of the XGIS detector. The first part of this work (Chapter 4) addresses the experimental tests on the test board with ORION I, a single channel version of the ASIC. We completely characterized ORION I, verifying its functionality and deriving its performance parameters, both at room temperature and under a thermal cycle. We concluded that future versions of this prototype should include a SDD more similar to the one specifically designed for XGIS, to avoid the thermal expansion coefficients of each material in the detector being too different. Moreover, we concluded that the test equipment should be improved to lower its noise contribution, e.g., by using a serial communication protocol instead of a parallel one.

In the second part of this work (Chapter 5), we proceed with the characterization of a second prototype (ORION IV), which implemented the THESEUS SDD, as following our previous results, closer to the final XGIS design. This version includes 4 channels and a complete version of the ORION internal logic. We performed both functionality and performance tests on ORION IV. We observed that, compared to the previous prototype (ORION I), ORION IV shows an increment on its performance of a factor of 2, with better energy resolution (3.2% against 7.9% of ORION I) and lower electonic noise by 63.9%. We completed the test with the calculations for the capacitance, observing a value that is almost (10% below requirements) compliant with the requirements.

The ORION IV is still being tested. However, the improvement with respect to ORION I is already noticeable. The next step will include a scintillation crystal in the detector chain, to have a complete characterization of the XGIS acquisition process. We also plan to increase the number of channels with each new prototype design, thus increasing the complexity of the acquisition chain, until a full XGIS prototype module can be achieved, which is foreseen to handle 64 channels.

The scope of the XGIS monitor cameras within the THESEUS mission is to extend the redshift limit up to which we are able to detect GRBs, and to observe them in the full high-energy band with a monolithic detector. Moreover, it should be able to quickly pinpoint the counterparts to the gravitational wave events, that will be detected in the future. In this context, forthcoming experimental testing should also include sensitivity and timing accuracy performance.

The thesis is organized as follows: Chapter 1 provides a general introduction to GRBs, Overview of different emission types and theories behind their origins and a presentation of the detection of GW170817, the first GW event associated with an electromagnetic counterpart. Chapter 2 gives an overview of the principal observatories that have observed/are currently detecting GRBs, reporting the main properties of the instruments onboard each mission, including THESEUS. Chapter 3 describes in detail the XGIS, semiconductors, and scintillators, with a focus on the readout electronics (ORION chipset) which is the basis of the new detector. Chapter 4 describes the tests performed on the first prototype (ORION I), and Chapter 5 reports the tests performed on the second prototype (ORION IV). I present the conclusion of my work and plans for future developments in Chapter Conclusions.

Sommario

THESEUS, *Transient High-Energy Sky and Early Universe Surveyor* è una proposta di missione spaziale sviluppata da un'ampia collaborazione europea, presentata nel 2016 all'Agenzia Spaziale Europea (ESA) per il bando M5 del Programma Cosmic Vision. Nel 2018, THESEUS, insieme ad altre due missioni, è stata selezionata dall'ESA per uno studio di valutazione (Phase A) della durata di 3 anni, ma nel 2021 non è stato selezionato per il lancio. Tuttavia è stato è stato riproposto nel 2022 per il bando M7. Attualmente, ha appena concluso lo studio preliminare, (Phase 0), che comprendeva l'analisi CDF (Concurrent Design Facility), ed è in attesa della decisione dell'ESA per l'ammissione alle fasi successive della selezione. THESEUS monitorerà il cielo in una banda di energia molto ampia (0.3 keV – 10 MeV), con capacità di focalizzazione nella banda dei raggi X soffici (0.3–5 keV), un grande *grasp* (prodotto di area efficace e campo di vista) e un'elevata *positional accuracy* ($\leq$2 arcmin in 0.3–5 keV), con la capacità di identificazione a bordo dei transienti. La localizzazione, dell'ordine dell'arcosecondo, e la determinazione del redshift averrà con un telescopio operante nel vicino infrarosso. Sarà un veicolo spaziale con un alto grado di autonomia e agilità, con la capacità di trasmettere tempestivamente a terra le informazioni sui transienti. Gli strumenti a bordo di THESEUS sono XGIS (*X-Gamma Imaging Spectrometer*), due camere con maschera codificata che utilizzano come rivelatori per raggi X e γ sia SDD (*Silicon Drift Detectors*) che scintillatori CsI(Tl), dedicati all'osservazione di *Gamma Ray Burst* (GRB), tali camere possono fare *imaging* fino a 150 keV e spettroscopia fino a 10 MeV; SXI(*Soft X-ray Imager*), due monitor *Lobster Eye* dedicati all'osservazione nei soft X e all'*imaging* in seguito al rilevamento da parte di XGIS; IRT (*InfraRed Telescope*) con la capacità di *imaging* e di fare spettroscopia, dedicato all'osservazione nella banda infrarossa e alla misura del redshift dei GRB.

Nella mia tesi ho caratterizzato i primi due prototipi dell'ASIC (*Application Specific Integrated Circuit*) ORION, un circuito elettronico di lettura multi-chip disegnato per

XGIS.

La mia tesi (Capitolo 4) riguarda la caratterizzazione di due rilevatori con ORION, per verificare se sono conformi ai requisiti richiesti dall'ESA; questi prototipi sono pensati per ottimizzare la produzione scientifica del rivelatore XGIS. La prima parte di questo lavoro riguarda i test sperimentali sulla scheda di prova ORION I, verificandone la funzionalità e ricavandone i parametri di prestazione, sia a temperatura ambiente che in un ciclo termico. Abbiamo concluso che le future versioni di questo prototipo debbano includere una SDD più simile a quella disegnata appositamente per XGIS, per evitare problemi legati ai diversi coefficienti di espansione termica del sistema. Inoltre, abbiamo concluso che la strumentazione di test utilizzata dovrebbe essere migliorata per ridurre il suo contributo al rumore, ad esempio usando un protocollo di comunicazione seriale invece di uno in parallelo come su questa scheda.

Nella seconda parte del mio lavoro (Capitolo 5), si è proceduto con la caratterizzazione di un secondo prototipo (ORION IV), che implementa una SDD più vicina al disegno finale per XGIS, come suggerito dai risultati precedenti. Questa iterazione comprende 4 canali e una versione completa della logica interna di ORION. Abbiamo eseguito test di funzionalità e prestazioni su ORION IV. Abbiamo osservato che rispetto al prototipo precedente (ORION I), ORION IV mostra un incremento delle prestazioni di una fattore 2, con una migliore risoluzione in energia (3.2% contro 7.9% di ORION I) e una riduzione del rumore elettronico del 63.9%. Abbbiamo completato la caratterizzazione con la misura del valore della capacità di test, osservando un valore quasi conforme ai requisiti (10% in meno).

ORION IV è ancora in fase di test. Risulta tuttavia evidente il miglioramento rispetto a ORION I. Il prossimo passo sarà l'inserimento di un cristallo scintillatore, per avere una caratterizzazione completa della catena di acquisizione di XGIS. Si prevede inoltre ad aumentare il numero di canali con ogni nuovo prototipo, aumentando così la complessità della catena di acquisizione, fino ad ottenere un prototipo completo del modulo base di XGIS, che dovrà gestire 64 canali.

Lo scopo della missione THESEUS è quello di estendere il limite in redshift fino al quale siamo in grado di osservare GRB, e di osservarli nell'intera banda di alta energia con un unico rivelatore. Inoltre, sarà in grado di effettuare *follow-up* a rapida cadenza temporale delle controparti degli eventi di onde gravitazionali che verranno osservati nei prossimi anni. In questo contesto, le caratterizzazioni sperimentali sui prototipi includeranno misure di sensibilità e sulle *performance* nella misura dell'informazione temporale.

Questa tesi è organizzata come segue: il capitolo 1 fornisce un'introduzione generale ai GRB, una panoramica dei diversi tipi di emissione, delle teorie alla base della loro origine e una breve presentazione del primo evento di onde gravitazionali associato a una controparte elettromagnetica (GW170817). Il capitolo 2 presenta quelli che sono attualmente e che sono stati i principali esperimenti spaziali che hanno osservato i GRB, con una descrizione delle caratteristiche dei vari strumenti a bordo, e una introduzione alla missione THESEUS e ai suoi strumenti. Il capitolo 3 descrive in dettaglio lo strumento XGIS, i semiconduttori, i cristalli scintillatori, con un focus sull'elettronica di lettura (ORION) che è alla base del rivelatore. Il capitolo 4 descrive i test effettuati sul primo prototipo (ORION I) e il capitolo 5 illustra i test effettuati sul secondo prototipo (ORION IV). Presento poi le conclusioni del mio lavoro e i piani per sviluppi futuri nel capitolo Conclusion.

Contents

Chapter 1

Gamma-Ray Bursts

1.1 Gamma-Ray Burst Physics

The γ-ray sky is populated by highly energetic transient events called Gamma-Ray Bursts (GRBs). GRBs are short flashes of γ-rays. It is impossible to predict when and from where they will arrive. They are so bright ($\sim 10^{50--52}$erg s^{-1}) that they can outshine all other gamma-ray sources during their short lifetime (Vedrenne et al. 2010). The spectra of the GRBs are heterogeneous. While some events display a smooth evolution, others show variability at millisecond timescales (Gehrels et al. 2009). Some are characterized by multiple flares, some rise very rapidly and others are instead quite shallow (see Figure 1.1). These burst last between 0.01 and 100 seconds.

These events are distributed isotropically, showing no sign of a disk component, see Figure 1.2. Of all the various models, proposed over the years, only those invoking sources at cosmological distances, or in the solar neighbourhood (at a distance smaller than the disk scale-height $\sim$ 100pc) were consistent with these observational facts (Gehrels et al. 2009).

Their nature as distant luminous extragalactic objects was established once it was realised that they have significant afterglows at X-ray, optical and infrared wavelengths which enabled their positions to be determined accurately (Longair 2011). These bursts are associated with extremely violent events involving stellar-mass objects in distant galaxies (Vedrenne et al. 2010).

The analysis of GRB duration is bimodal, with two broad peaks: short events (SGRBs), lasting less than two seconds, and long events (LGRBs), of longer duration, of up to 100

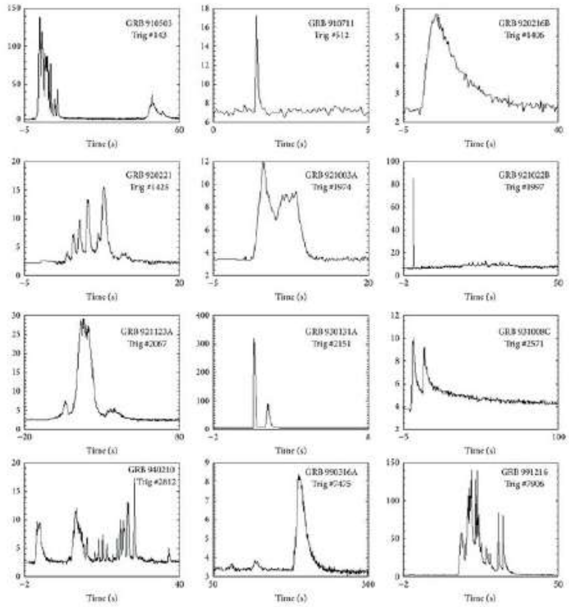

Figure 1.1: A selection of the variety of temporal profiles of GRBs, as detected by Swift-BAT. Note the wide range of durations and morphologies of the bursts, highlighting the diversity of the prompt GRB emission (Pe'er 2015).

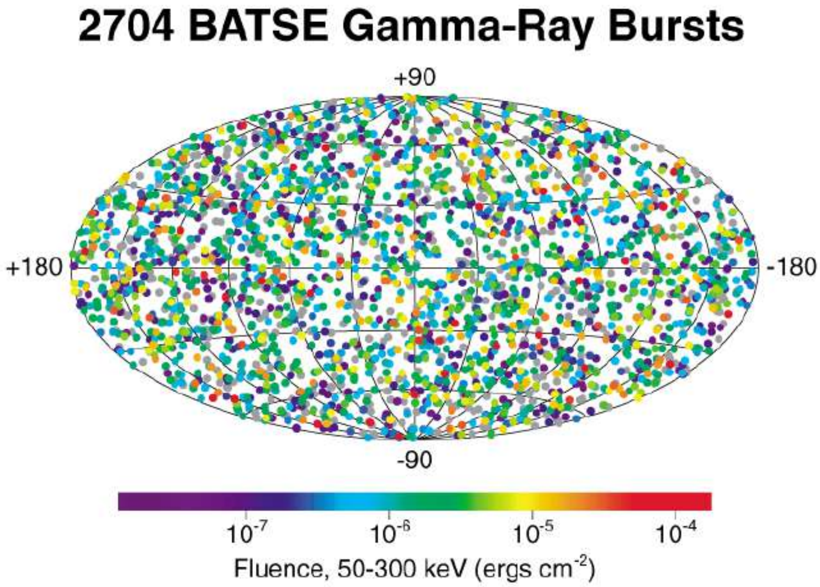

Figure 1.2: 2704 Gamma-Ray Bursts Including Fluence. Credit: BATSE Team [1].

seconds.

The most common measure of duration is T_{90}, defined as the time during which the cumulative counts increase from 5% to 95% above background, thus encompassing 90%

[1] `https://heasarc.gsfc.nasa.gov/docs/cgro/batse`

of the total GRB counts. T_{50} is defined similarly to include 50% of the counts (Kouveliotou et al. 1993). The times thus defined are an intensity-independent measure of duration, unlike previous definitions. Both distributions in Figure 1.3 show a dip around 2 s (Kouveliotou et al. 1993).

Examination of the spectral properties of the two populations suggests that short bursts emit more high-energy radiation, while long bursts somewhat less. This is often encapsulated in the so-called hardness ratio, the ratio between the observed photon flux at high (100–300 keV) and low energies (50–100 keV) (Pe'er 2015).

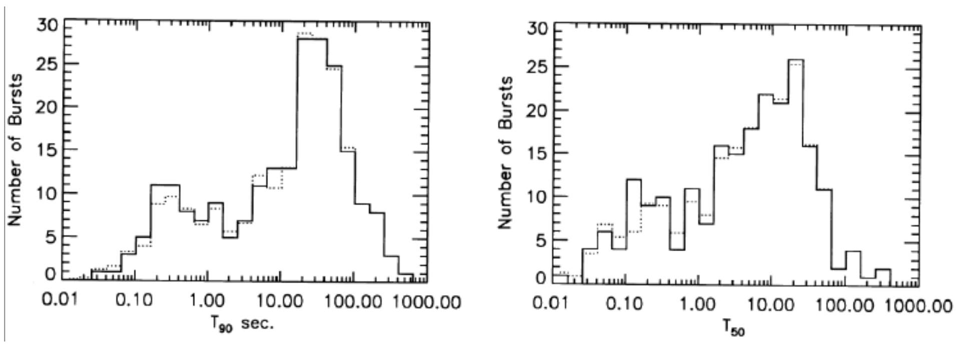

Figure 1.3: Left: Distribution of T_{90} for the 222 GRBs of the first BATSE catalogue. Right: Distribution of T_{50} for the same GRBs set. Images taken from Kouveliotou et al. (1993).

GRBs are defined by the two phases of their emission, called prompt emission and afterglow. While the prompt emission is closely related to the burst event itself, the afterglow is crucial to determine the redshift of the source and thus to identify the host galaxy (Levan 2018).

1.1.1 Prompt Emission

The prompt emission spectra of GRBs is non-thermal. In general, they can be modelled with the Band function (Band et al. 1993). This function is described in energy space, as:

$$F_E = \begin{cases} A(\frac{E}{100keV})^{\alpha} e^{-E(2+\alpha)/E_{\text{peak}}}, & \text{if } E < \frac{(\alpha-\beta)E_{\text{peak}}}{(2+\alpha)} \equiv E_{\text{break}} \\ A[\dfrac{(\alpha-\beta)E_{\text{peak}}}{100keV(2+\alpha)}]e^{((\beta-\alpha)(E/100keV)^{\beta})}, & \text{if } E \geq \frac{(\alpha-\beta)E_{\text{peak}}}{(2+\alpha)} \end{cases} \tag{1.1}$$

which in practice smoothly joins the low energy (α) and high energy (β) spectral slope (Levan 2018). The break in the two slopes occurs at $E_{break} = \frac{(\alpha-\beta)E_{peak}}{(2+\alpha)}$, but a more commonly used parameter is the E_{peak} which defines the peak of the $\nu F_{\nu} = EF_{E} = E^2 N_E$ spectrum where N_E is the number of photons and an overall normalization, A $(1/E^2 N_E)$. This is the photon energy at the peak of the spectrum where the most of the energy from the burst is emitted (Levan 2018).

1.1.2 Afterglow

The prompt emission quickly transitions into the decaying afterglow (Gehrels et al. 2009). In 1997, the X-ray telescope onboard BeppoSAX was pointed at the position of γ-ray burst GRB 970228 within 8 hours of the event has taken place, thus detecting the first ever afterglow (Costa et al. 1997a). Subsequently, afterglows were observed throughout the electromagnetic spectrum. These observations enabled a precise position for the burst to be determined and the association of this burst with a very faint galaxy was established by observations with the Hubble Space Telescope. This observation confirmed that the γ-ray bursts form a population of extragalactic objects (Longair 2011).
Representative X-ray afterglow light curves are shown in Figure 1.4 for both long and short GRBs. These X-ray light curves start as early as 100 s after the GRB trigger and cover up to five decades in time (Gehrels et al. 2009). The complex behaviour can be summarized in five stages: a distinct component of rapid decay (I), a shallow decay component (II), a normal decay component (III), a jet-breaking component (IV) and X-ray flares (V).

I *Steep decay*: Bright rapidly-falling afterglow immediately after the prompt emission, with a decay slope in the range [3;10];

II *Shallow decay*: Shallow transition with a decay slope flat (in this case called *plateau*). This may relate to ongoing central engine activity;

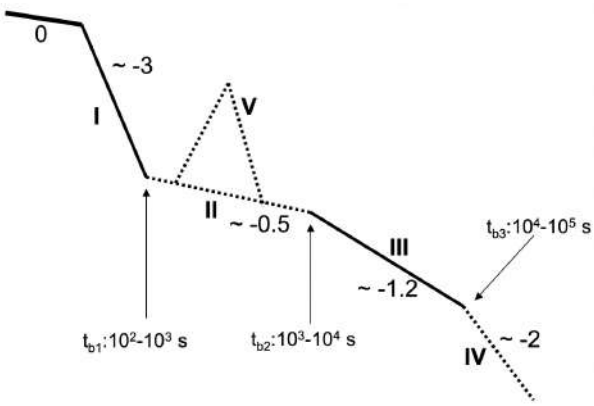

Figure 1.4: A synthetic diagram X-ray lightcurve based on observational data from the Swift XRT. The phase "0" denotes the prompt emission. Four power law lightcurve segments along with a flaring component are identified in the afterglow phase. The segments I and III are the most common, and they are marked with solid lines. The other three components are only observed in a fraction of bursts, so they are marked as dashed lines. Typical temporal indices in the four segments are indicated in the figure. The flares (segment V) have similar spectra as the segment I, and time evolution of the spectral index during the flares has been observed in some bursts (e.g. GRB 050502B) (Zhang et al. 2006).

III *Normal decay*: Normal decay ($\sim$ 1) is consistent with the interpretation in according to which the first break occurs when the slowly decaying emission from the forward shock dominates over the steeply decaying tail emission of the prompt γ-rays as seen from large angles. This may occur on timescales of tens of seconds, up to timescales of several days in extreme cases.

IV *Rapid decay*: A temporal break in which the decay steepens. Beyond this point, the flux of the counterpart typically decays with a decay slope $\sim$2. This temporal break is often referred to as the jet break.

V *Flares*: During this plateau phase (or potentially earlier or later), bursts can exhibit small or large X-ray flares. These flares are due to the same mechanism responsible for the prompt emission, which is usually attributed to the activity of the central engine.

About 50% of well-localized GRBs show optical and IR afterglow. A observed optical afterglow is typically around 19-20 mag one day after the burst. Many afterglow light curves show an achromatic break to a steeper decline with $\alpha \sim 2$. Radio afterglow was

detected in $\sim$ 50% of the well-localized bursts ($\sim$1 arcsecond or preferably subarcsecond (Gehrels et al. 2009)). Most observations are carried out at about 8 GHz since the detection falls off drastically at higher and lower frequencies (Piran 1999).
Once afterglows were discovered, it was possible to use them to precisely locate bursts in the sky and to identify any underlying source. Formally, the presence of absorption lines only means that the burst lies at a redshift higher than that of the absorption. However, the absorber is usually ascribed to the host galaxy of the burst. This direct redshift measurement immediately rules out all Galactic models for long GRB production, and implies they are highly energetic cosmological explosions. This makes the GRBs powerful cosmological probes, to study the interstellar and intergalactic medium enabled by their afterglows. Furthermore, there have been suggestions that the very first generation of stars, pristine systems made only of hydrogen and helium (often referred to as Population III stars) could be the progenitors of GRBs. Therefore these γ-rays sources can be an ideal probe to locate the very first stellar collapses (Levan 2018).
The detection of GRBs, a rapid follow-up at longer waveband (X-ray and IR), and the identification of the redshift by space missions can be a strong test of the hypothesis that reionization was brought about by star light.
This can be done by the mission proposal THESEUS, as will be explained in more detail in Chapter 2.3.1.

1.1.3 Fireball model

The prompt emission and the afterglow can be explained with the *Fireball* model proposed by Cavallo & Rees (Cavallo & Rees 1978).
A time-scale of the variability of the order of milliseconds indicates that the energy of the GRBs must originate from regions less than about 10^5 km in size Longair (2011), and their fluxes imply huge energies which can reach 10^{54} erg if the emission is isotropic Vedrenne et al. (2010).
From the energy and scale of the emitting region, it follows that the source region must expand relativistically, hence, just as in the extreme extragalactic γ -ray sources, the γ-ray bursts must involve relativistic bulk motions. In the simplest picture, the source is taken to be a relativistic fireball, meaning a highly relativistic expanding sphere which heats the surrounding gas and drives a relativistic shock wave into it. The radiative

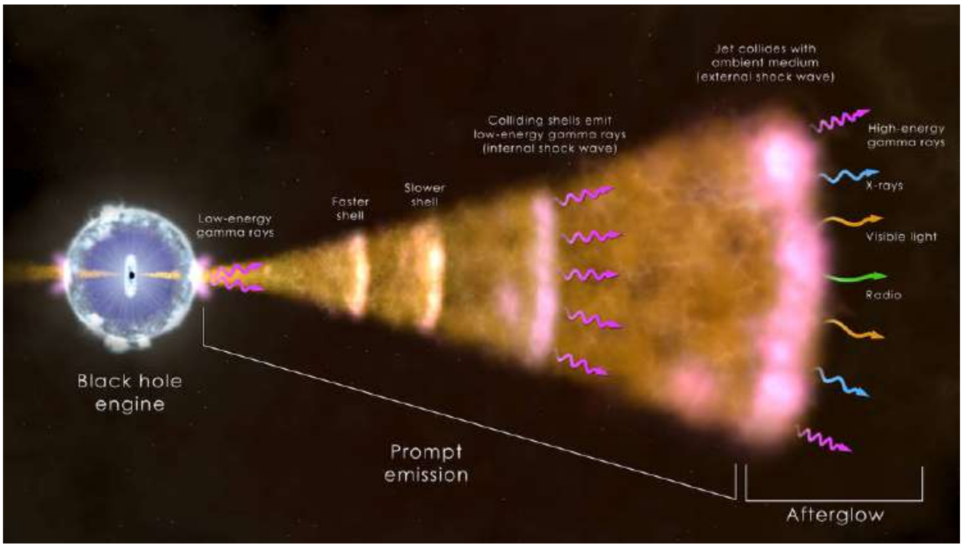

Figure 1.5: Artist's impression of the Fireball model. The light across the spectrum arises from hot gas near the black hole, collisions within the jet, and from the jet's interaction with its surroundings. Credits: NASA's Goddard Space Flight Center[2].

efficiency of a GRB shock is a function of the bulk Lorentz factor, the magnetic field strength, the particle acceleration mechanism and the density of the external medium. An artistic impression is shown in Figure 1.5

In the case of a baryon-loaded fireball, the sound speed in the ejecta may be low, and the reverse shock will be strong and at least mildly relativistic. If the fireball is magnetically dominated, it will have a large outward Lorentz factor even relative to the frame of the contact discontinuity.

The radiative efficiency and spectrum depend on several factors, including the physical nature of the outflow material, the efficiency of field growth and particle acceleration behind the shocks, and the degree of mixing across the contact discontinuity. If an adeguate magnetic field is present (10^{14--15} G (Piran 2005)), either through shock amplification or because it is frozen into the ejecta, each shock contributes a synchrotron component, and a higher energy component due to IC scattering of the synchrotron photons by the same electrons. If both reverse shock and blast wave acceleration are efficient, a third additional IC component arises, due to up scattering of reverse synchrotron photons by a blast wave electrons Meszaros & Rees (1993). The fireball would expand and adiabatically cool as it converts its internal into kinetic energy, and its kinetic energy could

[2]`https://www.nasa.gov/content/goddard/nasa-sees-watershed-cosmic-blast-in-unique-detail`

be reconverted into radiation as it impacts the external medium, the highest efficiency (for non-relativistic expansion) being achieved when the fireball swept up an amount of external matter comparable to the fireball mass Meszaros (2019).
The GRB radiation, which started concentrated in the γ-ray range during the burst, is expected to progressively evolve into an afterglow radiation which peaks in the X-rays, then UV, optical, IR and radio wavebands (Figure 1.5). The afterglow properties, made in advance of the observations, agreed well with subsequent detections at these photon energies, followed up over periods of up to months Gehrels et al. (2009).
This emission mechanism could also be responsible for the smooth curvature characterizing GRB average spectra Amati (2006).

1.2 Origin

Much of what we know about GRBs comes from the study of their afterglows, how they illuminate the circumburst surroundings and from the study of their host galaxies. An understanding of the nature of the GRBs sources is strongly linked to the way through which gravity, spin, and energy can combine to form collimated, ultrarelativistic outflows. These elements are few and fragile, and the tapestry is as yet a poor image of the real Universe (Gehrels et al. 2009). The following sections provide a summary of the origins of the two categories of GRBs.

1.2.1 Long GRBs

The long bursts are associated with active star formation and, in particular, the deaths of massive stars Longair (2011).
One of the most accepted models is the *collapsar model*. The collapsar model is referred to rotating massive stars, isolated or in a binary system whose iron core eventually collapses directly to form a black hole (BH) Woosley (1993). In the seconds/minutes following the collapse, the black hole accretes the residual matter of the core and emits a powerful relativistic jet. The progenitors of collapsars, likely Wolf-Rayet stars, are closely related to the progenitors of hydrogen-deficient supernovae (SNe), i.e. type Ib/Ic supernovae Woosley & MacFadyen (1999). This collapsar model requires three essential ingredients:

a massive core, the removal of the hydrogen envelope, and a high angular momentum in the core. This last ingredient is important to achieve an efficient energy conversion and create a natural rotation axis free of matter, along which a jet and an expanding blast wave will be able to escape Vedrenne et al. (2010). A diagram impression is shown in 1.6.

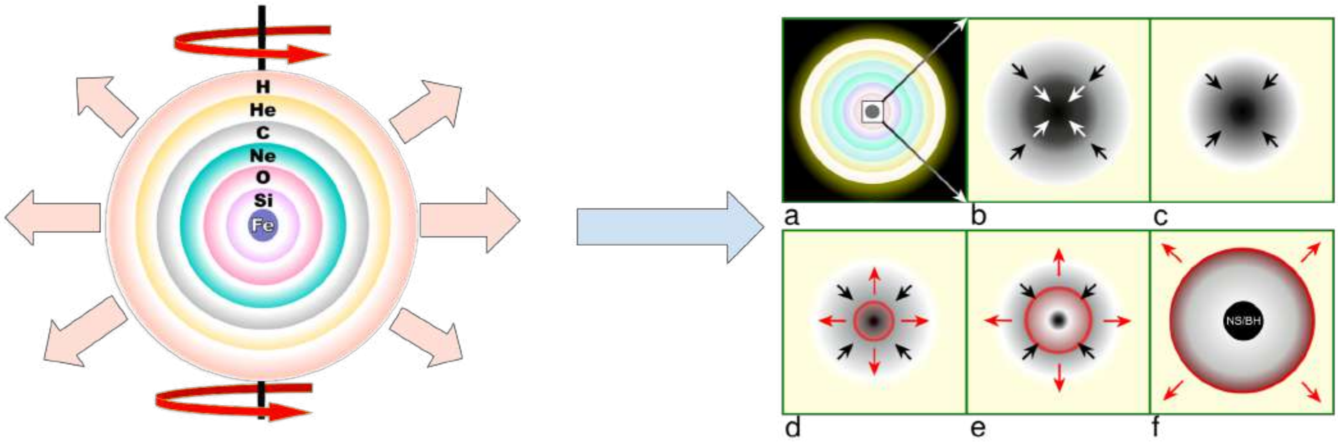

Figure 1.6: Left: This diagram shows a simplified (not to scale) cross-section of a massive, evolved star, It depicts multiple shells, each housing distinct elements. Additionally, it highlights the expansion of the outer hydrogen layer and signifies the star's high angular momentum through its rotation on its axis. Right: The diagram provides a close-up on the core's transformation from an Fe core to either a NS or a Black Hole BH. Illustration by R.J. Hall [3]. Right: Simplified core collapse scenario. Illustration by R.J. Hall [4].

A star of 25–35 $M_\odot$ in the main sequence and with a helium core of 9–14 $M_\odot$ is a good candidate to become a *failed supernova*. The rapidly rotating helium star collapses into a neutron star (NS) and then promptly into a black hole. The in-falling matter in the equatorial plane is slowed by rotation and piles up into a disk. The matter falls in from the outer edge of the core in a few seconds, resulting in a considerably lower density region within the funnel near the BH horizon, creating the conditions for the launching of a jet. This implies a low-density, highly relativistic jet, injected by the central engine at the base of the outflow Mészáros & Rees (2001). This first outflow can take several seconds because the jet cannot develop as long as polar accretion continues at high rates. After several seconds the poles are sufficiently clean for a reversal of the flow to become possible. Energy is dissipated in the disk by baryons annihilation focused by density

[3] https://commons.wikimedia.org/wiki/File:Evolved_star_fusion_shells.svg
[4] https://commons.wikimedia.org/wiki/File:Core_collapse_scenario.svg

and pressure into jets. Energy deposition blows a low-density bubble, avoiding baryonic contamination. Momentum and energy continue to be deposited in these bubbles.

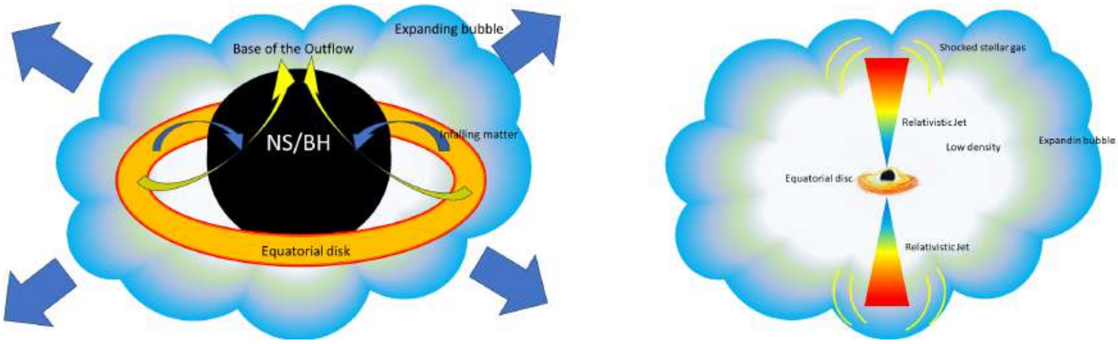

Figure 1.7: Left: Close up on the inner core of the collapsed star, with infalling matter from the equatorial plane, and the formation of the the launching jet. Right: Evolution of the outflow from the central core; the jet evolves from the polar funnels into the expanding bubble of the SN.

The jet, which is followed through a significant fraction of the star's mass, maintains a collimation of half angle of 10°. In front of the contact discontinuity between the jet and the stellar gas, there is a thin layer of shocked stellar gas, while behind the jet is slowed down. Jet material exceeds the external stellar pressure and spills out sideways and trails behind the jet, creating a sheath of low-density, relativistic material resembling the cocoons that surround the relativistic jets of radio sources. The jet now reaches the outer hydrogen envelope of the star and the drop in density gives it a large boost, reaching ultra-relativistic speeds. After emerging, the jet head advances ultra-relativistic. There could also be subrelativistic shocks at the bubble boundary, which compress the envelope gas, probably inducing further clumpiness, and a reverse shock that moves into the bubble, producing a synchrotron UV/X-ray continuum Mészáros & Rees (2001). This type of model is unable to produce bursts shorter than ~ 5 s Vedrenne et al. (2010).

1.2.2 Short GRBs

The very short time scales of short GRBs variability suggest that neutron stars and black holes are involved but, because they are not associated with star-forming regions in galaxies, they cannot be young stellar systems. An appealing possibility is that they are associated with the merger of binary neutron stars, of a neutron star and a black hole, or of two black holes Longair (2011).

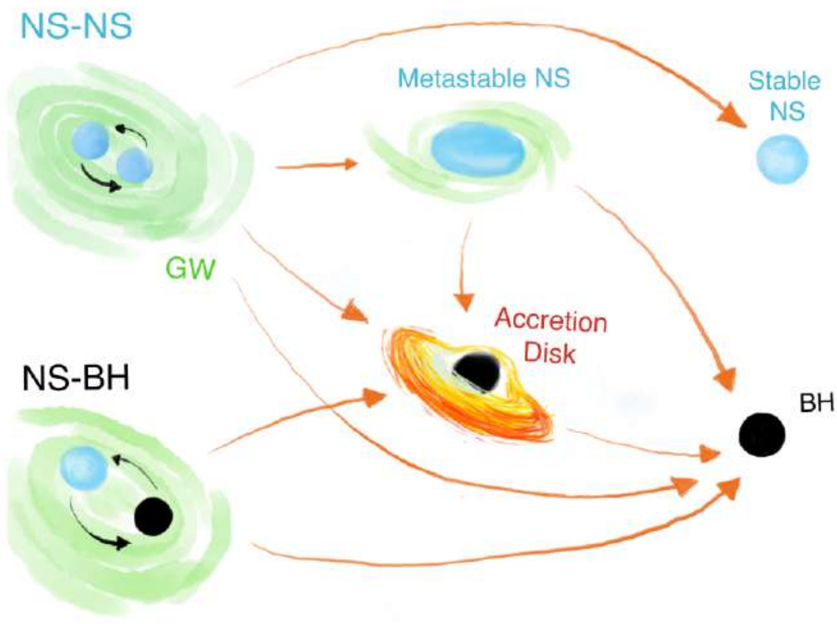

Figure 1.8: Artist's impression of the environment surrounding GRB 020819B, based on ALMA observations (Ascenzi et al. 2021).

The NS-NS are most often discussed because the radioactive ejecta from the merger provides a source for powering transient emission, in analogy with Type Ia SNe. Given the low mass and high velocity of the ejecta from a NS-NS/BH-NS merger, the ejecta will become transparent to its radiation quickly Metzger (2017).

The merger of two neutron stars represents a huge reservoir of gravitational binding energy. A sudden energy release can be quickly and continuously transformed into a radiation-dominated plasma. In NS-NS mergers, a rapidly spinning black hole is formed orbited, by a neutron-rich high-density torus. The temperature is so high ($\sim 10^{10--11}$K) that nuclei are photo-disintegrated, leading to a mixture of free neutrons α particles, protons electrons and positrons. In this system, the two main reservoirs of energy are the binding energy of the orbiting debris and the spin energy of the black hole Vedrenne et al. (2010).

Magnetic configurations that can power GRBs require fields of a few 10^{15} G, which can be quickly reached Kluźniak & Ruderman (1998). The onset of the neutron star collapse is expected to initiate differential rotation, i.e. a short-lived DROCO (differentially rotat-

ing collapsed object) as a central engine for GRBs. This is the DROCO phase preceeding the collapse into a BH. The DROCO may also be a torus rotating around a spinning BH. The DROCO winds up initial seed magnetic fields by differential rotation until the magnetic pressure $B^2/8\pi$ becomes comparable to the pressure of the matter. At this point, magnetic toroids will become buoyant, float up and break through the surface where they create an ultra-relativistic blast, and so the creation of the short GRB.
The end product of an NS-NS or BH-NS merger is a central compact remnant, either a BH or a massive NS. Sustained energy input from this remnant provides an additional potential source of heating and a dense neutron-rich environment, ideal for the formation of heavy elements such as gold and platinum (Metzger 2017; ESA/SCI 2021).
Metzger et al. (2010) determined the true luminosity scale of the radioactively-powered transients of NS mergers by calculating the first light curve models which used radioactive heating. Based on their derived peak luminosities being approximately one thousand times brighter than a nova, Metzger et al. (2010) first introduced the term 'kilonova' to describe the EM counterparts of NS mergers Metzger (2017).

If short-duration GRBs originate from NS-NS or NS-BH mergers, then one way to constrain kilonova models is via optical and NIR follow-up observations of nearby short bursts on timescales of hours to a week. All else being equal, the closest GRBs provide the most stringent constraints; however, the non-thermal afterglow emission—the strength of which can vary from burst to burst—must also be relatively weak, so that it does not outshine the thermal kilonova. Evidence for NIR emission over the expected afterglows was found following the short GRBs 050709 and 060614, indicative of possible kilonova emission. The merger of stellar mass BH-BH binaries is not expected to produce luminous EM emission due to the absence of baryonic matter in these systems. Thus, despite the large sample of BH-BH mergers, a full synthesis of the GW (Gravitational waves) and EM sky requires the discovery of GWs from merging binaries containing neutron stars (NS), of either the NS-NS or BH-NS varieties Metzger (2017).
This was the case for GW170817.

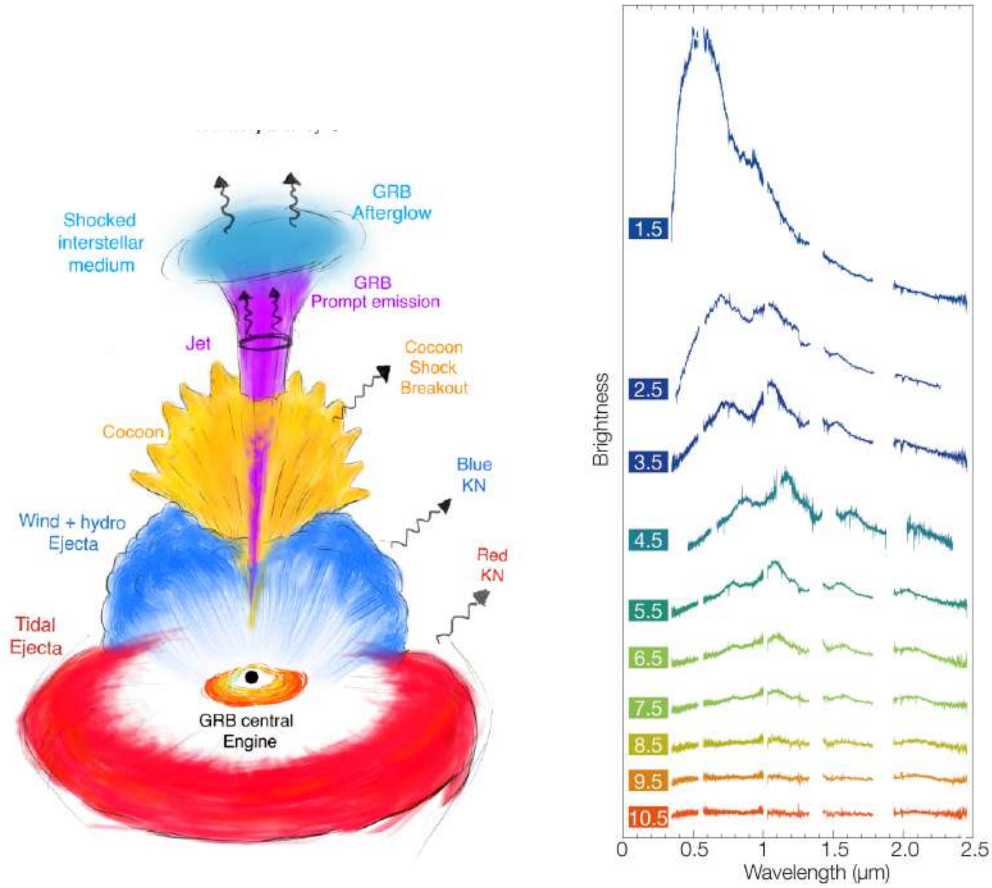

Figure 1.9: Left: Artistic representation of the scenario following an NS-NS/NS-BH merger, when an accreting BH is formed. The red component denotes the tidal ejecta, the blue component is the hydrodynamic and wind ejecta, the purple component is the jet and the yellow component is the matter of the ejecta heated by the jet (cocoon). The different components are not represented in scale Ascenzi et al. (2021). Right: The spectral evolution of AT2017gfo associated with GW170817 and GRB 170817A. The observations were taken with the X-shooter instrument on the Very Large Telescope, and cover the UV to near-IR in a single snapshot (Levan 2018).

1.2.2.1 Multimessenger Astronomy

The final proof of the kilonovae theory was found in 2017, with the detection of GW170817, by LIGO (Laser Interferometer Gravitational Wave Observatory) and the Virgo interferometer in Italy.

Gravitational waves alone provide a wealth of astrophysical information, but this is greatly enhanced by the addition of electromagnetic (or neutrino) information. In particular, while gravitational waves provide good measurements of compact object masses, as well as potentially the radii of neutron stars, they do not by themselves provide a link back to directly observed systems and signals that are emitted directly across the electromagnetic spectrum.

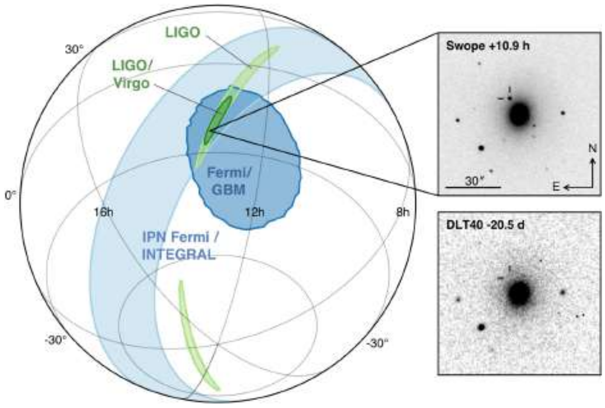

Figure 1.10: Left: Localization of the gravitational-wave, γ-ray, and optical signals of the GW170817. The left panel shows an orthographic projection of the 90% credible regions from LIGO (light green), the initial LIGO-Virgo localization (dark green), triangulation from the time delay between Fermi and INTEGRAL (light blue), and Fermi-GBM (dark blue). Right: The location of the apparent host galaxy NGC 4993 in the Swope optical discovery image at 10.9 hr after the merger (top right) and the DLT40 pre-discovery image from 20.5 days before the merger (bottom right) Abbott et al. (2017).

For the first time, gravitational and electromagnetic waves from a single source were observed. The electromagnetic observations further support the interpretation of the nature of the binary, and comprise three components at different wavelengths: (i) a prompt of a short GRB that demonstrates that BNS mergers are the progenitor of at least a fraction of such bursts; (ii) an ultraviolet, optical, and infrared transient (kilonova), which allows for the identification of the host galaxy and is associated with the binary NS merger, and (iii) delayed X-ray and radio counterparts that provide information on the environment of the binary. An image timeline follow-up of the GW170817 is shown in Figure 1.11

This colossal follow-up was possible with a big effort from all the facilities. After the first detection of LIGO and VIRGO, the GBM camera of Fermi automatically generated an announcement of detection. After 10 seconds it was detected by INTEGRAL-SPI anticoincidence shield. The combination of LIGO-Virgo-INTEGRAL and Fermi, starting from a region of $\sim$33 deg^2 with LIGO-Virgo, a region of $\sim$350 deg^2 with Fermi confirmed by INTEGRAL, together constrained the localization of the source at at $\sim$

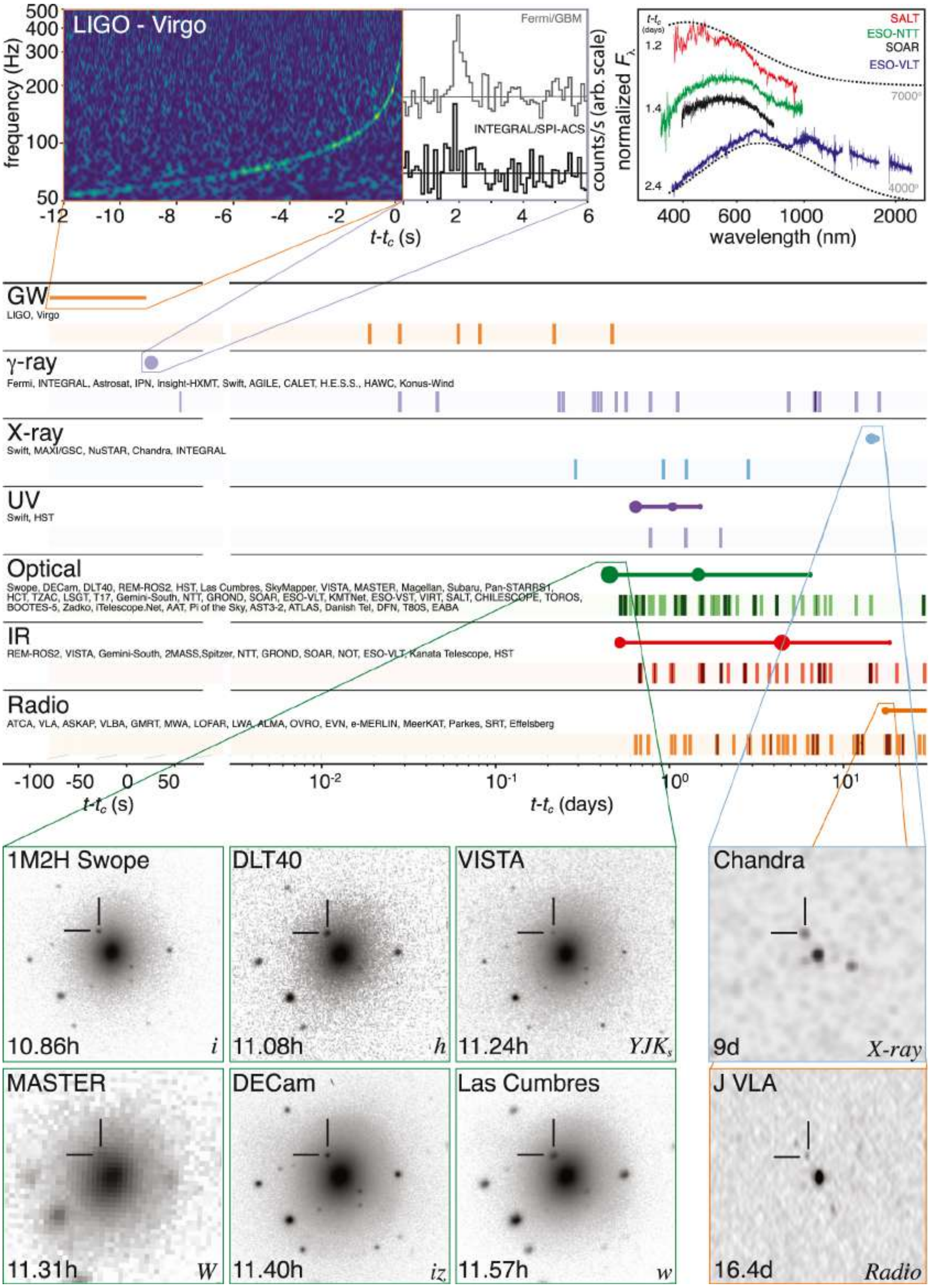

Figure 1.11: Timeline of the discovery of GW170817, GRB 170817A, SSS17a/AT 2017gfo, and the follow-up observations are shown by messenger and wavelength relative to the time tc of the gravitational-wave event (Abbott et al. 2017).

28 deg^2 (Abbott et al. 2017). This triggered a broadband observing campaign. The

One-Meter, Two-Hemisphere (1M2H) team was the first to discover and announce with the Swope telescope at Las Campanas Observatory in Chile, followed by Dark Energy Camera, Las Cumbres Observatory and Visible, Infrared Survey Telescope for Astronomy, and by the instrument UVOT/XRT on Swift, locating a bright optical transient (AT2017gfo) at 10.6” from the center of NGC 4993. Over the following two weeks, a network of ground-based telescopes, from 40 cm to 10 m, and space-based observatories spanning the ultraviolet (UV), optical (O), and near-infrared (IR) wavelengths followed up GW170817, up to the radio counterpart (Abbott et al. 2017). These observations These observations offer a sequential description of the physical processes related to the merger of a binary neutron star. As reported in Abbott et al. (2017), the results of this campaign demonstrate the importance of collaborative gravitational wave, electromagnetic, and neutrino observations and mark a new era in multi-messenger, time-domain astronomy.

The information available via these different messengers provides a unique route to understanding the behaviour of extreme systems. Indeed, the detection of GRB 170817A in coincidence with the gravitational wave detected neutron star merger GW170817 highlights this spectacularly.

Since GRBs are also relatively rare events, with detection rates of a few per week, their frequency is sufficiently low that the coincident detection of a GRB and GW trigger within a few seconds of each other has a low chance probability. This means that time information alone can enable the association of a GRB with a GW transient, even in the absence of any positional information, as was the case for GW170817 and GRB170817A. Given the challenges of searching gravitational wave error boxes, this is extremely appealing. Indeed, the error boxes derived from these γ-ray detectors can frequently be much smaller than from the GW event alone, providing a far easier search for afterglows or host galaxies (Levan 2018). Besides, their afterglow counterparts can be used as powerful background lighthouses probing in absorption both the IGM and the ISM of faint galaxies otherwise inaccessible with other observing technics (ESA/SCI 2021).

Detectors are now increasing the sensitivity where the detection of astrophysical signals in EM, GW and neutrinos is becoming more than possible. Ultimately, multimessenger astronomy offers the ability to address questions that have been inaccessible to date, and in doing so can provide answers to long-standing controversies in astronomy. However, we are right at the beginning of this era.

Joint observations of short GRBs and GW with the current mission are expected to be rare, likely no more than one per decade. In the 2030s a more sensitive third generation of ground-based GW interferometers, such as, the Einstein Telescope, will allow the observations of compact objects merge at larger distances (ESA/SCI 2021). To maximise the scientific return of the multi-messenger astronomy during the 2030s, it is essential to have a facility that can detect EM counterparts of GW/neutrinos triggers with wide spectral coverage.This is another goal of the THESEUS mission proposal (Chapter 2.3).

Chapter 2

High-energy telescopes history

In this chapter, we will present an overview of the history of high-energy astrophysics, in particular the discovery and the study of GRBs.
In Section 2.1 we will describe the past missions connected to the discovery of the GRBs and subsequent studies, while in Section 2.2 we summarize the ongoing missions that improve and allow the study of GRBs. In the final Section 2.3 we will present the mission proposal THESEUS. Throughout the chapter, we will focus on high-energy instruments, connected to the study of GRBs.

2.1 Past Missions

2.1.1 USAF Aerobee rockets

The history of GRBs is directly related to the history of high-energy astrophysics.
The USAF Aerobee rockets were among the first high-energy observatories. They were built with two Geiger counters partially surrounded by anticoincidence scintillators (see Appendix B), as is shown in Figure 2.1, to reduce the cosmic-ray background and to limit the field of view (FoV). The flight of these rockets was at around 230 km of altitude. The onboard instruments were sensitive in the 1.5–6 keV band, as reported in Table 2.1 (Giacconi R. 1962).
They provided a first glimpse of the high-energy sky, discovering sources like Sco-X1 and the X-ray background (Giacconi R. 1962). Sco-X1 showed an X-ray luminosity 10^3 times the entire luminosity of the Sun, and later was associated with a binary system con-

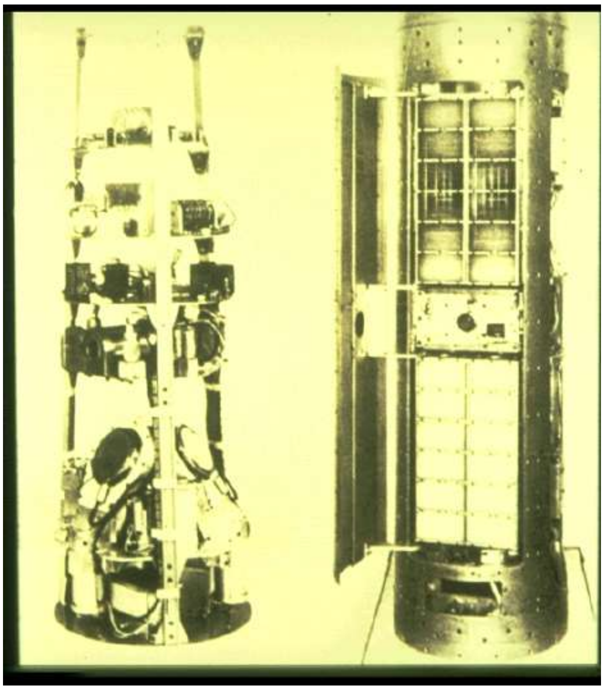

Figure 2.1: Picture of a USAF Aerobee 150 rocket with a view of the 2 Geiger counters, and the anticoincicence scintillator (Giacconi R. 1962).

taining a neutron star. The X-ray background was later associated with active galactic nuclei (Giacconi 2003; Longair 2011).

However, the discovery of GRBs that opened the way the study of these phenomena

FoV(Field of View)	open
Energy Range	1.5-6 keV
Energy Resolution	-
Spatial Resolution	-

Table 2.1: Instrumental characteristics of the experiment on the Aerobee rocket (Giacconi R. 1962).

was done by the Vela satellites.

2.1.2 Vela Satellites

The Vela satellites, run by the U.S. Department of Defense and the U.S. Atomic Energy Commission, were the first ones to be sensitive over a large energy band, from 3 to 750 keV (Terrell et al. 1982). They were intended primarily to monitor compliance with the treaty of nuclear detonation in the atmosphere, but did provide highly useful celestial data (Terrell 1989). The Vela satellites (Figure 2.2, left panel) carried two sets of instruments. The scintillation X-ray detector (XC), shown in the right panel of Figure 2.2, consisted of two 1 mm thick NaI(TI) crystal scintillators seen by photomultiplier tubes. In front of each crystal, there was a slat collimator providing an FWHM aperture of $\sim$ 6.1 $\times$ 6.1 degrees. The effective detector area was 26 cm^2. The other onboard instrument (called X-2) was a set of six γ-ray detectors. They had a total volume of $\sim$60 cm^3 of CsI(Tl) scintillators and could detect photons in the 150-750 keV energy range (Singer et al. 1969). A summary of the instrumental characteristics of Vela 5B is reported in Table 2.2.

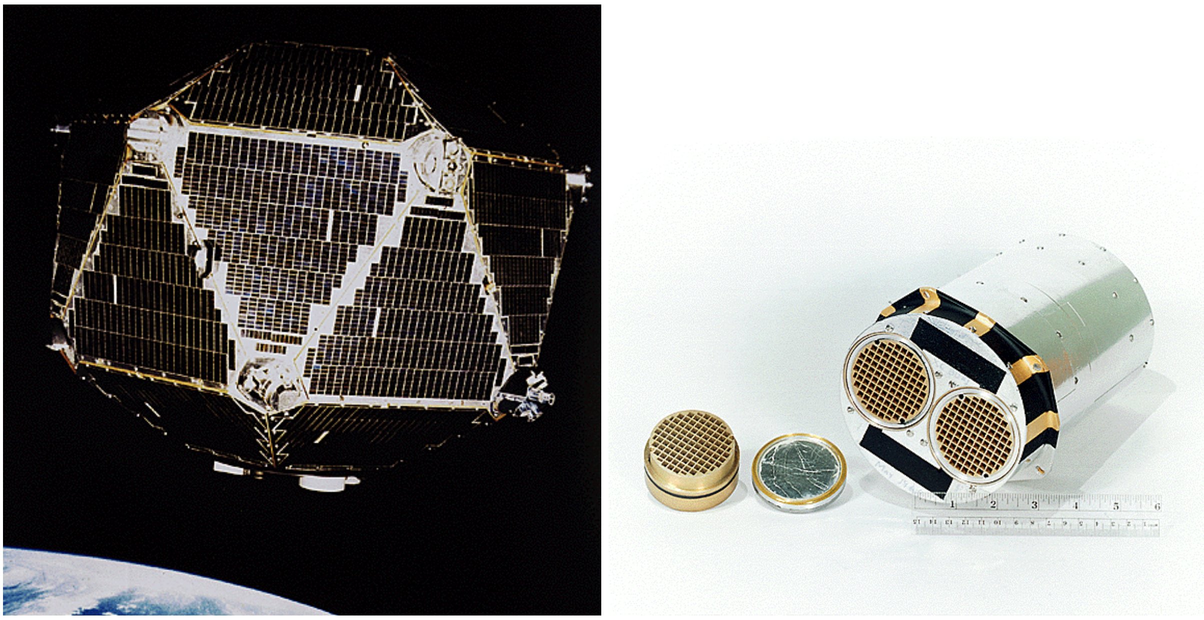

Figure 2.2: Left panel: an image of one of the Vela satellites in a Low-Earth Orbit [1]. Right panel: image of the scintillation X-ray detector (XC), with photomultiplier tubes and slat collimator [2].

These satellites were the first to record a GRB. They discovered the first X-ray burst, and throughout their lifetime (operative until 1979) they continued monitoring transient behaviour from X-ray sources (Terrell et al. 1982).

Four Vela satellites recorded 73 gamma-ray bursts in ten years of activity. However, for

[1] `https://heasarc.gsfc.nasa.gov/Images/vela5b/vela5b_5.gif`

[2] `https://heasarc.gsfc.nasa.gov/Images/vela5b/vela5b_4.gif`

security and political reasons, only in 1973 the USA declassified Vela's results and the GRBs became an argument of study (Ray W. Klebesadel 1973).

FoV	4π sr
Energy Range	3-750 keV
Energy Resolution	-
Spatial Resolution	6°

Table 2.2: Instrumental characteristics of Vela 5B (1969) (Terrell 1989).

2.1.3 Compton Gamma Ray Observatory

In 1991 the Compton Gamma Ray Observatory (CGRO) was launched by NASA. CGRO had 4 instruments that covered six orders of magnitude in energy, from 30 keV to 30 GeV (Gehrels & Shrader 2001). The 4 instruments onboard were BATSE, EGRET, OSSE and COMPTEL, as shown in Figure 2.3.

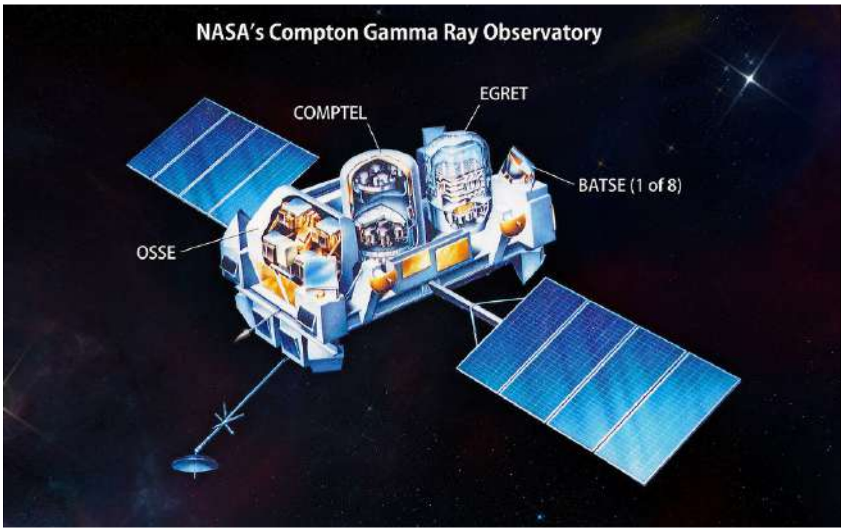

Figure 2.3: Artistic representation of CGRO. The OSSE instrument was located in the front, while EGRET and Comptel were in the middle and BATSE on the back. Image taken from NASA[3].

[3]https://astrobiology.nasa.gov/missions/cgro/

2.1.3.1 EGRET, OSSE, COMPTEL

The Energetic Gamma Ray Experiment Telescope (EGRET) detected γ rays in the 20 MeV-30 GeV range. It had a large field of view of 80 degrees (Esposito et al. 1999). A summary of the instrumental characteristic is reported in Table 2.3.

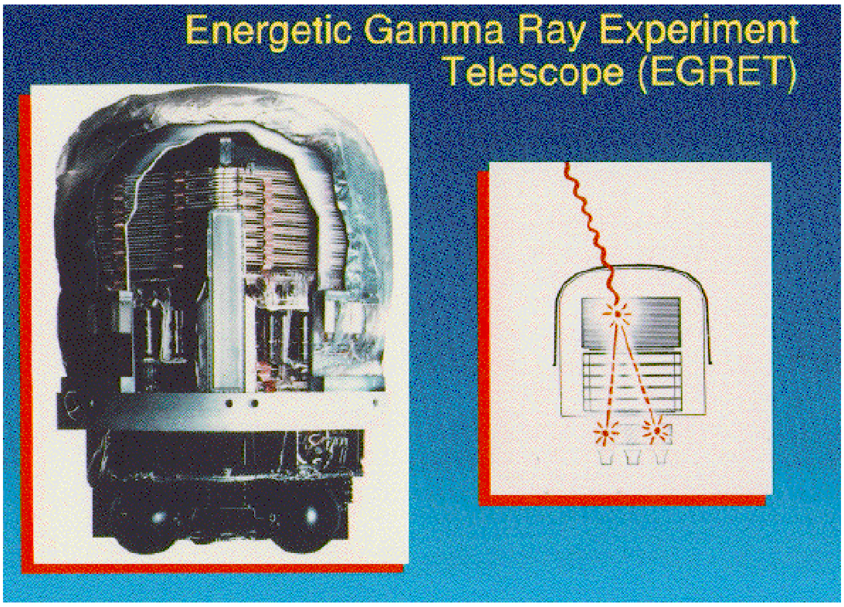

Figure 2.4: View of the instrument EGRET. Image taken from NASA[4].

EGRET detected gamma rays using a spark chamber for direct measurement and a NaI(TI) calorimeter for energy measurement. The spark chamber had on the top and on the side a plastic scintillator dome to recognize events from charged particles entering from above, which is shown in Figure 2.4.

FoV	80°
Energy Range	20 MeV-30 GeV
Energy Resolution	~25 % at 100 MeV
Angular Resolution	5 - 30 arcmin.

Table 2.3: Instrumental characteristics of EGRET (Kanbach et al. 1989).

Another instrument onboard CGRO was OSSE, Oriented Scintillation Spectrometer Experiment, designed to observe astrophysical sources in the 0.05 to 10 MeV energy range.

[4] `https://heasarc.gsfc.nasa.gov/docs/cgro/cgro/egret.html`

It was composed of four detectors, shown in Figure 2.5. The primary element of each detector is the NaI(TI)-CsI(Na) phoswich, optically coupled to each other and to a common photomultiplier tube (Johnson et al. 1993).

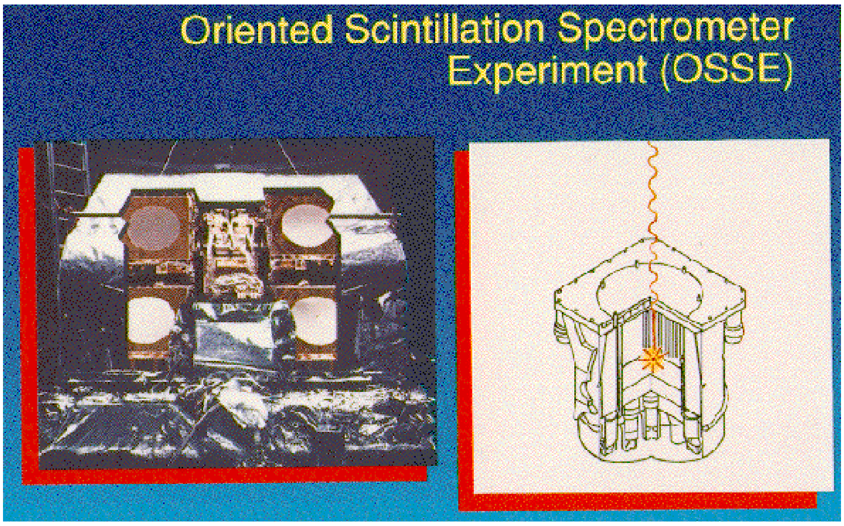

Figure 2.5: View of the instrument OSSE. Image taken from NASA[5].

A tungsten slat collimator, located directly above the NaI(Tl) portion of each phoswich, defines the gamma-ray aperture of the phoswich detector (Johnson et al. 1993). The instrumental characteristics are reported in Table 2.4.

FoV	$3.8° \times 11.4°$ FWHM
Energy Range	0.05-10 MeV
Energy Resolution	8% at 0.661 MeV
Spatial Resolution	-

Table 2.4: Instrumental characteristics of OSSE (Johnson et al. 1993).

COMPTEL, an Imaging Compton Telescope, was capable of imaging 1 steradian of the sky in the 0.8-30 MeV energy range; a summary of its instrumental characteristic is reported in Table 2.5 (Schonfelder et al. 1993). A representation of the COMPTEL instrument is reported in 2.6.

[5] https://heasarc.gsfc.nasa.gov/docs/cgro/cgro/osse.html

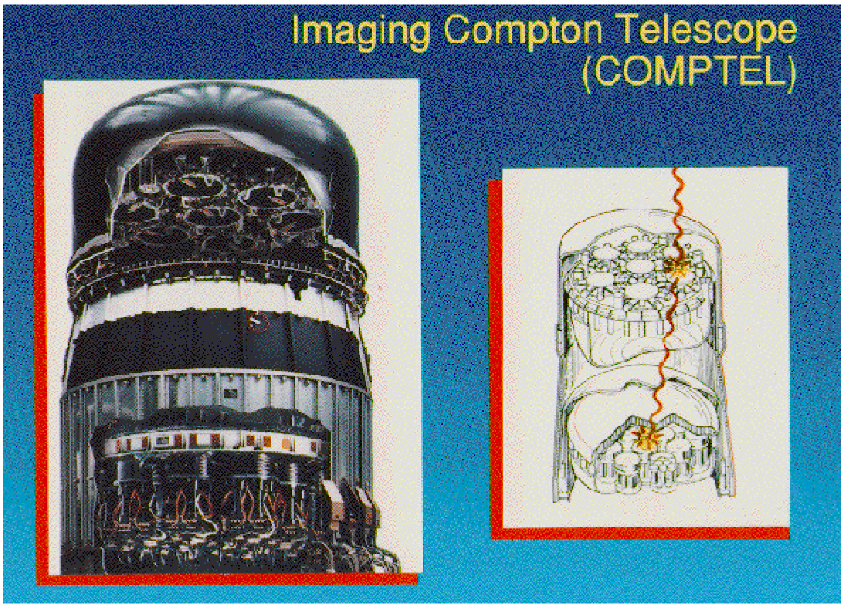

Figure 2.6: View of the instrument COMPTEL. Image taken from NASA[6].

The COMPTEL upper detector assembly consisted of seven cells, filled with a liquid scintillator (NE213A). The lower detector assembly is composed of 14 identical detector modules of cylindrical Nal(Tl) crystals. The idea was to first have a gamma ray Compton-scattered in the upper detector, which would then undergo a second interaction in the lower detector. From the direction of the two scattered events and from the energy loss COMPTEL was able to locate the celestial source. Together, the location and the energy losses determine the overall energy and angular resolution of the telescope.

As shown in Figure 2.6, the two detectors were separated by 1.5 m and each of them was surrounded by a thin anticoincidence shield made of a plastic scintillator, which is used to reject charged particles.

FoV	~ 1 sr
Energy Range	0.8-30 MeV
Energy Resolution	5-8 %
Angular Resolution	5 - 30 arcmin

Table 2.5: Instrumental characteristics of COMPTEL (Schonfelder et al. 1993).

[6]https://heasarc.gsfc.nasa.gov/docs/cgro/cgro/comptel.html

2.1.3.2 BATSE

The Burst and Transient Spectrometer Experiment (BATSE) was an all-sky monitor, sensitive from 20 to 600 keV. Its instrumental specifics are summarised in Table 2.6. BATSE was made by eight identically configured detector modules, each of which contained two NaI(TI) scintillation detectors, a Large Area Detector (LAD), and a Spectroscopy Detector (SD) (Fishman et al. 1992). A representation of the BATSE instrument is shown in Figure 2.7.

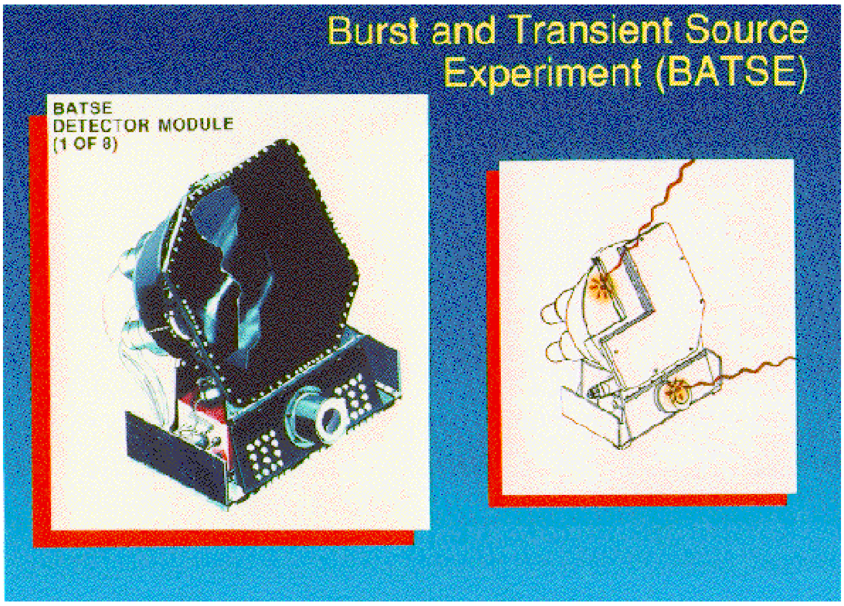

Figure 2.7: An image of BATSE detector and a diagram explaining the detection mechanism implemented by BATSE[7].

The LAD detector is a disk of NaI(Tl) scintillation crystal. A light collector housing on each detector brings the scintillation light into three photomultiplier tubes placed at the end of the light collecting cone, as shown in the lower part of Figure 2.7. A plastic scintillation detector in front of the LAD was used as an anticoincidence shield to detect and discriminate the background caused by charged particles (Fishman & Austin 1977).

The spectrograph was an uncollimated NaI(TI) scintillation detector. A single photomultiplier tube is directly coupled to the scintillation detector window.

BATSE could detect GRB onboard by examining the counts rates of each of the eight LADs for statically significant increases of the X/γ flux above background (Fishman &

[7] `https://heasarc.gsfc.nasa.gov/docs/cgro/cgro/batse.html`

Austin 1977).

The pointing accuracy of BATSE was only 4°, which made the identification of optical counterparts challenging (G.J. Fishman 2013).

FoV	4π sr
Energy Range LAD	20 keV - 1.9 MeV
Energy Range SD	10 keV - 100 MeV
Energy resolution LAD (at 0.88 keV)	30 %
Energy resolution SD (at 0.66 MeV)	8 %
Angular Resolution	4 °

Table 2.6: Instrumental characteristics of BATSE (G.J. Fishman 2013).

2.1.4 Beppo-SAX

Beppo-SAX (Satellite italiano per Astronomia X, Figure 2.8) was an Italian–Dutch satellite for X-ray astronomy. It was an X-ray mission able of observing targets in a range of over three orders of magnitudes, from 0.1 to 300 keV. It could monitor large regions of the sky in 1.5–26 keV, with 3 arcmin angular resolution, aimed at the detection and spectral study of high-energy transients (Boella et al. 1997a).

The instruments onboard SAX were Narrow Field Instruments (NFI) and Wide Field Instruments (WFI). The NFI consisted of a Low Energy Concentrator Spectrometer (LECS, 0.1-10 keV), three Medium Energy Concentrator Spectrometers (MECS, 2-10 keV), a High Gas Pressure Scintillator Proportional Counter (HPGSPC, 20-120 keV) and a Phoswich Detection System (PDS, 15-300 keV). The WFI consisted of two Wide Field Cameras (WFC, 1.5-26 keV) and the GRBM (Gamma Ray Burst Monitor) (Feroci 1999). The working principle of Beppo-SAX, with all these instruments onboard, was to do multi-wavelength observations, allowing the follow-up of the GRBs after the prompt emission. Beppo-SAX was the first to implement this idea among high-energy telescopes.

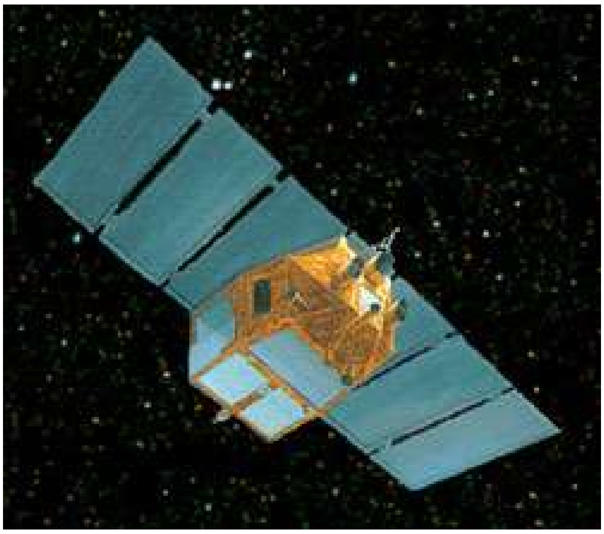

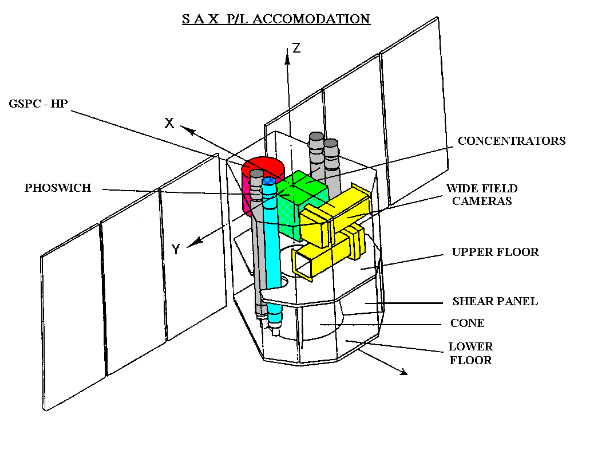

Figure 2.8: Left: An image of the Beppo-SAX spacecraft[8]. Right: A diagram showing the position of the instruments onboard the Beppo-SAX spacecraft[9].

2.1.4.1 The Beppo-SAX instrument suit

The LECS and MECS units consisted of grazing incidence X-ray concentrators, composed of 30 nested Nickel Au coated coaxial and co-focal mirrors with Wolter I geometry and a gas (Xenon) scintillation proportional counter.
The HPGSPC was a high-pressure scintillator proportional counter filled with a 5 atm gas mixture (90% Xe and 10% He).
The PDS consisted of a square array of four independent NaI(Tl)/CsI(Na) scintillation detectors capable of absorbing photons up to 300 keV. Each of the four detectors was composed of two crystals of NaI(Tl) and CsI(Na) optically coupled and forming what is known as PHOSWICH (acronym of PHOsphor sandWICH, PHW). The NaI(Tl) thickness was 3 mm and the CsI(Na) thickness was 50 mm. The scintillation light produced in each PHW is viewed through a quartz light guide (Frontera et al. 1997a; Manzo et al. 1997). The characteristics of all the described instruments are reported in Table 2.7.
The WFC consisted of two coded-aperture cameras, with detectors and masks of the same size. The mask was made of Iron and was located 0.7 m away from the detector, which was a multi-wire proportional counter filled with a gas mixture (94% Xe, 5% CO2, 1% He). The gas cell is made of Titanium coated with 1 mm of Al, and the mask and

[8]diagramshowingthepositionoftheinstruments
[9]http://people.oas.inaf.it/amati/tesi/node8.html

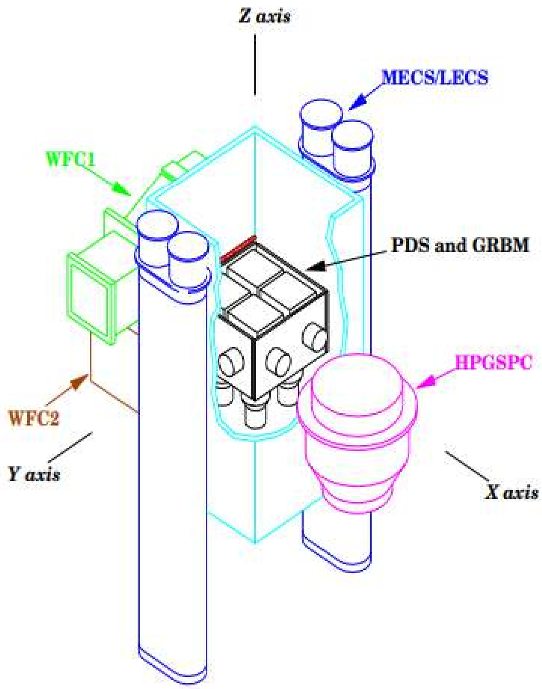

Figure 2.9: A diagram showing the position of the instruments onboard the Beppo-SAX spacecraft [10].

the detector are supported by a stainless steel structure (Feroci 1999).

A diagram with the representation of the instrument inside Beppo-SAX is reported in Figure 2.7.

2.1.4.2 GRBM

The GRBM is a secondary function of the anticoincidence shields of the PDS experiment, performed through dedicated onboard electronics. The instrument is composed of four identical CsI(Na) scintillator slabs, as shown in Figure 2.10, of about 1136 cm^2 each, surrounding the PDS detectors in a box-like configuration. The four detecting units were optically independent. Each one was composed of two optically coupled halves, whose light was seen by two independent photomultipliers (Feroci 1999).

The big step forward done by BeppoSAX was the observation of GRB 970228. The burst lasted around 80 seconds and had multiple peaks in its light curve. Within a few hours, the BeppoSAX team used the X-ray detection to determine the burst's position

[10] `http://people.oas.inaf.it/amati/tesi/node9.html`

WFC

FoV	20° × 20°
Energy Range	2–30 keV
Energy Resolution (at 6 keV)	18 %
Angular Resolution	5 arcmin

LECS

FoV	0.5°
Energy Range	0.1–10 keV
Energy Resolution (at 6 keV)	8.8%
Angular Resolution	2.1 arcmin

MECS

FoV	0.5°
Energy Range	1.3–10 keV
Energy Resolution (at 6 keV)	$\sim$ 8%
Angular Resolution (at 6 keV)	1.2 arcmin

PDS

FoV	1.3°
Energy Range	15–300 keV
Energy Resolution (at 60 keV)	$<$ 15%
Angular Resolution	-

HPGSPC

FoV	1.1°
Energy Range	4–120 keV
Energy Resolution (at 60 keV)	$\sim$ 4%
Angular Resolution (at 6 keV)	-

Table 2.7: Instrumental characteristics of LECS, MECS, HPGSPC, WFC and PDS. Data taken from Boella et al. (1997b), Manzo et al. (1997), Jager et al. (1997), Parmar et al. (1996), and Frontera et al. (1997a).

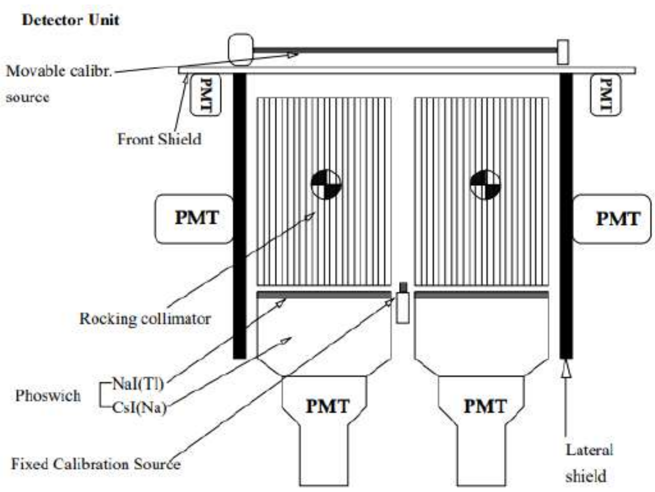

Figure 2.10: Image of a section of the PDS, where are shown the phoswich detectors. Image taken from Frontera et al. (1997b).

with an error box of 3 arcminutes, and this was the first arcminute positioning of a GRB, and the first detection of an afterglow (Costa et al. 1997b). The localization of the GRB using the wide field monitor was employed to identify the specific region of the sky from which the GRB originated, with sufficient accuracy to enable subsequent pointing of narrow-field instruments that then pinpointed the GRB. The concept of localization using wide-field instruments and subsequent re-pointing with narrow-field instruments was employed. In the case of SAX, it required multiple satellite orbits and specific GRB recognition procedures, but it nevertheless paved the way for subsequent missions like SWIFT. THESEUS proposes the same observational methodology.

FoV	4π sr
Energy Range	40-700 keV
Energy Resolution (at 511 keV)	16 %
Angular Resolution	-

Table 2.8: Instrumental characteristics of GRBM (Feroci 1999) .

2.2 Ongoing Missions

2.2.1 INTEGRAL

An important European telescope for high-energy astrophysics is INTEGRAL, INTErnational Gamma-Ray Astrophysics Laboratory. It was launched by the European Space Agency (ESA) into Earth orbit in 2002 and was designed to provide imaging and spectroscopy of cosmic sources. An image of the INTEGRAL spacecraft is shown in 2.11. The mission is dedicated to the fine spectroscopy (E/ΔE = 500) and fine imaging (angular resolution: 12 arcmin FWHM) of celestial gamma-ray sources in the energy range 15 keV to 10 MeV, with concurrent source monitoring in the X-ray (4-35 keV) and optical (V-band, 550 nm) energy ranges (Winkler et al. 2003).
INTEGRAL consists of four instruments: SPI (Spectrometer on INTEGRAL), IBIS (Imager on Board the INTEGRAL Satellite), JEM-X (Joint European X-Ray Monitor) and OMC (Optical Monitor Camera).

Figure 2.11: Image of the spacecraft INTEGRAL. Image taken from ESA[11].

2.2.1.1 JEM-X and OMC

JEM-X carries out observations simultaneously with the main gamma-ray instruments and provides images in the 3–35 keV energy band with an angular resolution of 3 arcmin. It consists of two identical instruments and uses the coded mask technique for imaging. The detector consists of two identical high-pressure gas chambers filled with a mixture of xenon and methane (Lund et al. 2003). An image of a detector of JEM-X is reported in Figure 2.12. JEM-X has a spectral resolution of 1.3 keV at 10 keV, and a FoV of $4.8°$ fully coded. The total detection area of JEM-X is 1000 cm^2 (Lund et al. 2003). A summary Table of the JEM-X instrument is reported in 2.9.

The OMC is a standard optical refractor with a 5-centimetre lens and a CCD (charge-coupled device, 2055×1056 pixels, imaging area: 1024×1024 pixels) in the focal plane sensitive to stars with a visual magnitude up to 19.7. The CCD is located in the focal plane and includes a V-filter to cover the 500-600 nm wavelength range. An image of the OMC camera is reported in figure 2.12. The FoV is $4.979° \times 4.979°$, with an angular resolution of $\sim 23''$ PSF (Mas-Hesse et al. 2003b). A summary Table of the OMC instrument is reported in 2.9.

[11] `https://sci.esa.int/web/integral/-/30907-artist-s-impression-of-integral`

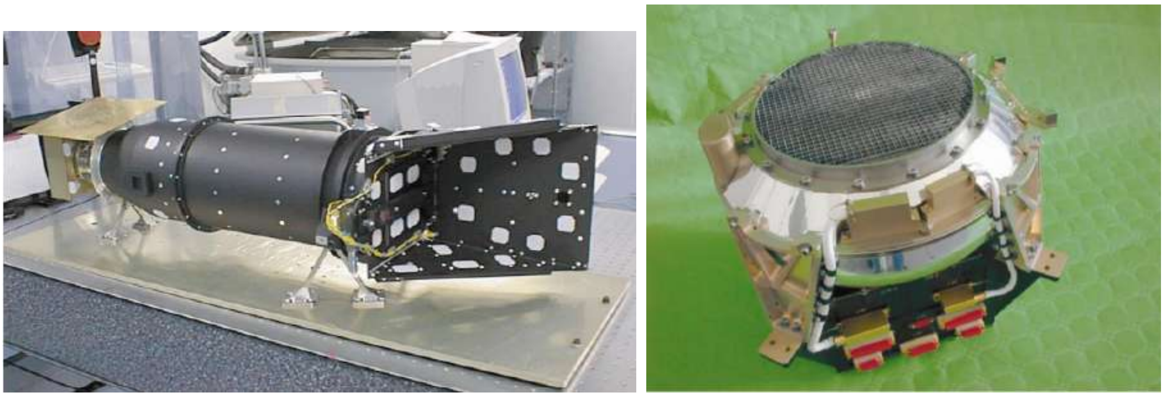

Figure 2.12: Left: An image of the OMC Camera Unit Flight Model. Image taken from (Mas-Hesse et al. 2003a). Right: Image of a JEM-X unit, where on top is placed the collimator. Image taken from (Lund et al. 2003).

JEM-X	
FoV	4.8° (fully coded)
Energy Range	3–35 keV
Energy Resolution	0.4 keV
Spatial Resolution	3 arcmin
OMC	
FoV	$4.979° \times 4.979$ °
Wavelength range	V filter (centered at 550 nm)
Angular Resolution	$\sim$ 6 arcsec

Table 2.9: Instrumental characteristics of JEM-X and OMC. Data taken from (Mas-Hesse et al. 2003a) and (Lund et al. 2003).

2.2.1.2 SPI

The spectrometer SPI performs high-resolution spectroscopy in the energy range between 20 keV and 8 MeV. It has an energy resolution of 2.3 keV at 1.3 MeV. It has a FoV of 16° (von Kienlin et al. 2003). A summary Table with the instrumental characteristics of SPI is reported in 2.10.

The camera of SPI consists of 19 cooled high-purity germanium detectors, operating at a temperature of −188°C (85 K). The imaging capability of the instrument is obtained by a passive-coded mask mounted 1.7 m above the camera with and hexagonal-coded aperture. It is made of 3-centimetre thick tungsten and consists of 127 hexagonal elements, of which 63 are opaque, and 64 are transparent. It is possible to use SPI anticoincidence shield to monitor the GRBs (von Kienlin et al. 2003). Figure 2.13 shows SPI and a closeup of the 19 cooled high-purity germanium detectors.

FoV	16 °
Energy Range	20 keV - 8 MeV
Energy Resolution (at 1.3 MeV)	2.3 keV
Angular Resolution	10 arcmin

Table 2.10: Instrumental characteristics of SPI (von Kienlin et al. 2003).

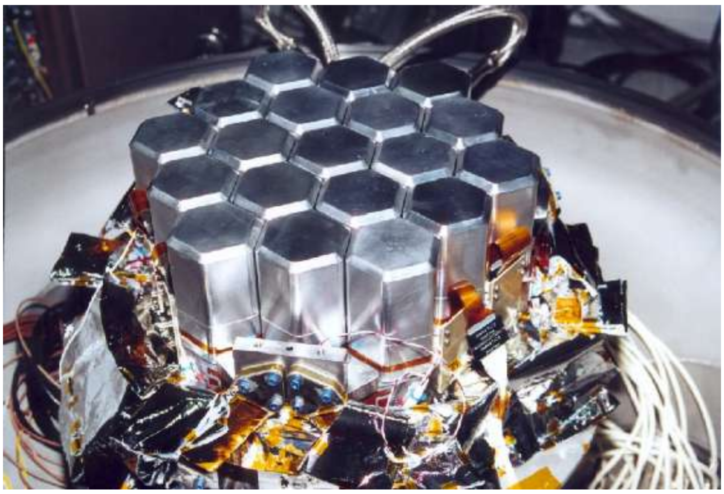
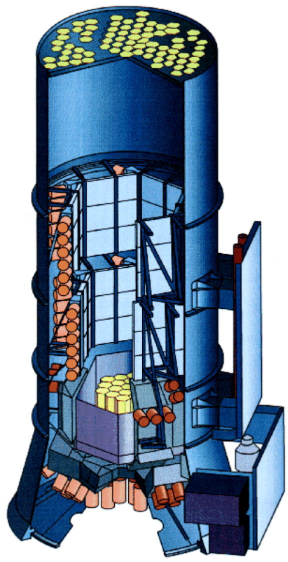

Figure 2.13: Left: An image of the detector assembly of SPI with its 19 hexagonal detectors made of Germanium. Right: Schematic view of SPI. The main elements of the gamma-ray telescope are the coded mask on the top, the Germanium detector (yellow hexagons at the bottom), and the anticoincidence system to actively shield the tube and the bottom of the telescope. Images taken from INTEGRAL-SDC[12].

[12]https://www.isdc.unige.ch/integral/gallery.cgi?INTEGRAL

2.2.1.3 IBIS

IBIS (Imager on Board the INTEGRAL Satellite) consists of two stacked detector planes: ISGRI (INTEGRAL Soft Gamma-Ray Imager) and PICsIT (Pixelated Imaging Cesium Iodide Telescope). IBIS features a coded mask and a large area ~ 3000 cm^2, a multilayer detector with CdTe (ISGRI) and CsI (PICsIT) (Ubertini et al. 2003). ISGRI's detectors with their small area (4×4 mm^2) are ideal to build up a pixellated imager with good angular resolution, but their small thickness (2 mm) restricts their use to the low-energy domain (Lebrun et al. 2003). The energy range of ISGRI is of 15 keV–1 MeV, with an energy resolution of 8% FWHM at 100 keV.
PICsIT is the IBIS high energy detector unit and is located below ISGRI. The two detectors are shielded by an active anticoincidence system made of 20 mm thick BGO crystals with PMT (photo multipliers tube) readout. The CsI(Tl) bars of PICsIT are optically bonded to custom-made silicon PIN photodiodes. This layer is divided into 8 rectangular modules of 512 detectors each, into a stand-alone sub-system. IBIS features two layers that allow the path of photons to be tracked in 3D as they scatter and interact with more than one element, as can be seen in Figure 2.14. The coded mask lays 3.4 meters above the detector bench and is composed of 11.2 mm squared pixels, 16 mm thick, interconnected by 2 mm ribs. Half of the cells are opaque to photons offering a $\sim 70\%$ opacity at 3 MeV, while the others are "open", with an on-axis transparency of 60% at 20 keV. The mask/detector set-up permits to achieve $\sim$10 arcsec point source location accuracy at 1 MeV. The higher limit, at 10 MeV, is due to the limited efficiency of IBIS and to the dynamic range of the PICsIT (Labanti et al. 2003). A summary Table of the instrumental characteristics is reported in 2.14.

FoV	$16° \times 9°$
Energy Range	15 keV- 10 MeV
Energy Resolution (100 keV)	9 keV
Angular Resolution	30 arcsec

Table 2.11: Instrumental characteristics of IBIS (Ubertini 1997).

INTEGRAL is also a successful actor in the new multi-messenger astronomy introduced by non-electromagnetic signals from gravitational waves and neutrinos: INTEGRAL found the first prompt electromagnetic radiation in coincidence with a binary neutron star merger (Abbott et al. 2017). It also discovered more than 600 new high-energy sources (Kuulkers et al. 2021). Most of the detections made by INTEGRAL were done within the Galactic plane, in three energy bands (17-60, 17-35 and 35-80 keV); it includes 402 objects exceeding a 4.7σ detection threshold on the nine years average map (Bird et al. 2016).

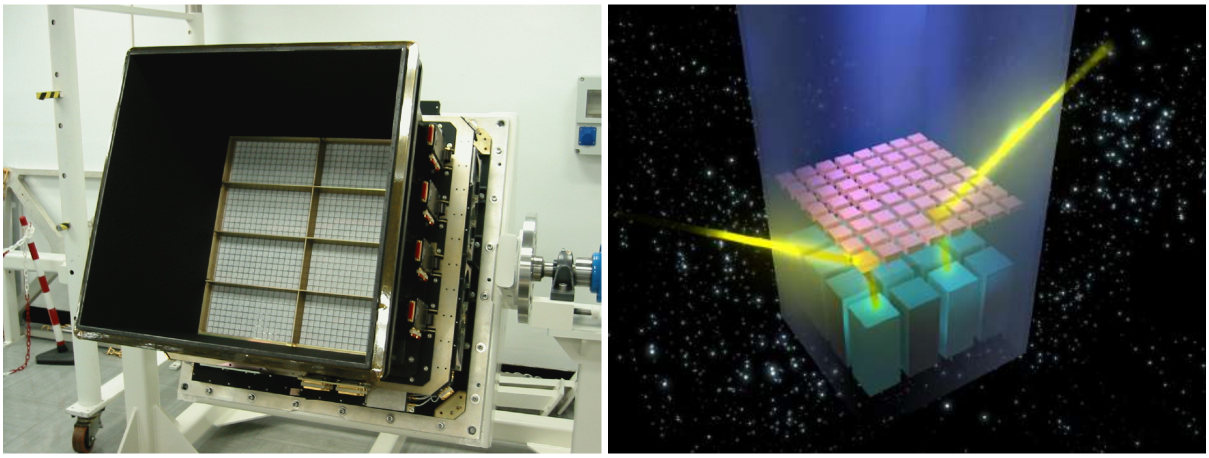

Figure 2.14: Left: A front view of the IBIS detector with the passive shield mounted. Right: An image of the working principle of IBIS CdTe pixel and CsI bars. Images taken from INTEGRAL-SDC[13].

2.2.2 Neil Gehrels Swift Observatory

The Neil Gehrels Swift Observatory (Figure 2.15), previously called the Swift Gamma-Ray Burst Explorer, was launched in 2004 and is still operative. Its burst detection rate is 100 per year, with sensitivity $\sim$3 times better than BATSE (Barthelmy et al. 2005).

Swift has three instruments to observe both GRBs and their afterglows in the gamma-ray, X-ray, ultraviolet and optical wavebands: BAT (Burst Alert Telescope), XRT (X-ray Telescope) and UVOT (Ultraviolet/Optical Telescope). With these three instruments, Swif has inherited the working principle of Bepp-SAX, i.e. the capacity of doing long follow-ups at longer wavebands and observe the GRB's afterglow. Whereas for SAX the follow-up operation required the intervention of mission control from the ground, in SWIFT the operation is managed directly on board and therefore faster (from 6/8 hours

[13] https://www.isdc.unige.ch/integral/gallery.cgi?INTEGRAL

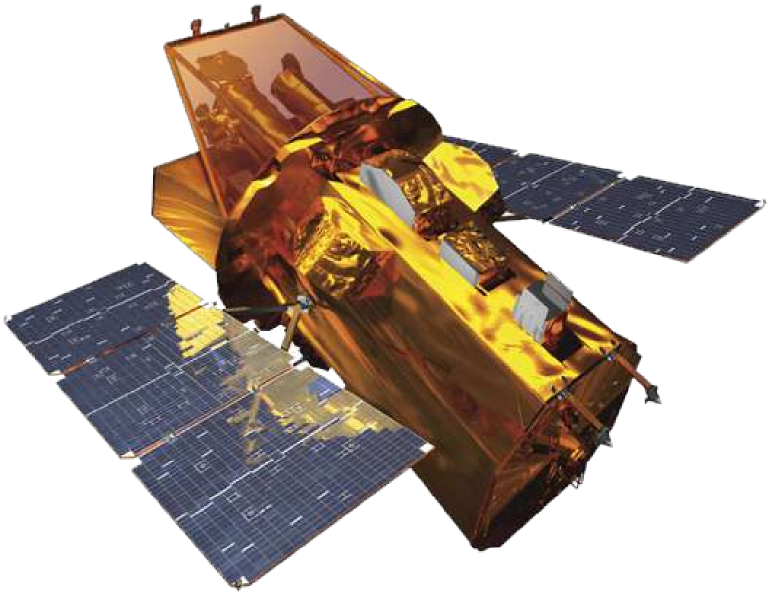

Figure 2.15: An image of the SWIFT observatory, taken from Swift [14].

of Beppo-SAX to ∼1–3 minutes).
The swift repointing capability of the XRT ensures that most bursts caught by BAT will be studied in X-ray light (Gehrels et al. 2004).
Immediately after a GRB is detected and located by BAT, the spacecraft slews to point both the UVOT and the XRT at the GRB location. The spacecraft's ∼90-second time-to-target means that about 100 GRBs per year are observed by the narrow-field instruments during the gamma-ray emission (Roming et al. 2005a).
The Swift mission has taken our knowledge of GRB to a higher level. BAT discovered over 1700 GRBs, and the number continues to increase (Oh et al. 2018).

2.2.2.1 BAT

The BAT, Burst Alert Telescope, has a large FoV (2.0 sr) designed to provide gamma-ray triggers with 4 arcminute positions. It has an energy range from 15 to 150 keV (with the capability of imaging from the coded mask, see Appendix A), and up to 500 keV for non-imaging. Since the BAT coded-aperture FoV includes the XRT and UVOT FoVs, long-duration gamma-ray emission from a burst can be studied simultaneously in the

[14]`https://imagine.gsfc.nasa.gov/observatories/learning/swift/multimedia/image_gallery.html`

X-ray and UV/optical regimes. BAT's detector plane pixels are CdZnTe (CZT) $4 \times 4 \times 2$ mm individual solid state detector assembled in an array of 8×16 elements with a 128 channel readout Application Specific Integrated Circuit (ASIC) for a total 1.2×0.6 m sensitive area (Barthelmy et al. 2005). A summary Table of the instrumental characteristics of BAT is reported in 2.12. This hierarchical structure, along with the nature of the coded-aperture technique, means that the BAT can tolerate the loss of individual pixels, and even whole blocks without losing the ability to detect bursts and determine locations (Barthelmy et al. 2001).

FoV	2.0 sr
Energy Range	15 - 150 keV
Energy Resolution X	3.3 keV at 60 keV
Spatial Resolution	1 - 4 arcminutes

Table 2.12: BAT instrumental characteristics (Barthelmy et al. 2005).

The typical resolution of the 60 keV gamma-ray line from an Am-241 radioactive source for an individual pixel is of 3.3 keV. The typical BAT background event rate in the full array above the threshold is about 10 000 counts per second. The trigger of the burst, defined within a time interval, is initiated only when a 5σ signal surpasses the background event rate, which is determined from a preceding time interval of the same duration. The trigger is subsequently followed by an onboard software check, ensuring that the trigger corresponds to a point source, effectively eliminating numerous background sources, including magnetospheric particle events. For example, if the particle background is high, or if there are nearby bright sources such as Sco X-1 or Crab, the sensitivity will be degraded (Barthelmy et al. 2005).
The coded mask has a D-shape mounted on a 5 cm thick composite honeycomb panel. The BAT coded-aperture mask uses a completely random, 50% open 50% closed pattern (Barthelmy et al. 2001). An image of the BAT instrument is shown in Figure 2.7.

The BAT instrument has two operative modes, burst detection and hard X-ray survey. While searching for bursts, the BAT performs an all-sky hard X-ray monitor. The detectors of BAT accumulate every five minutes detector-plane maps, which are included in

[15] https://swift.gsfc.nasa.gov/about_swift/bat_desc.html

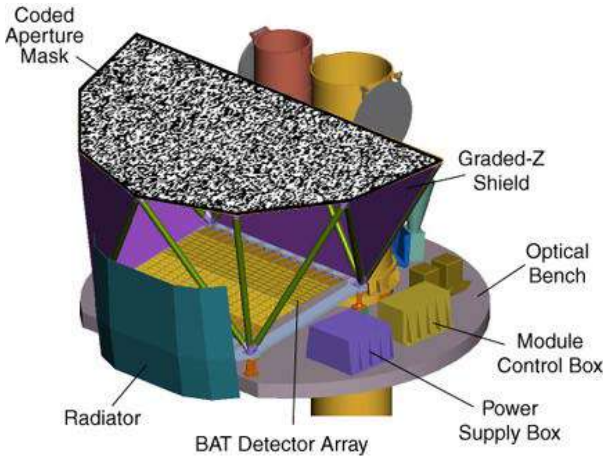

Figure 2.16: A diagram showing the main components of the BAT instrument. Image taken from Swift[15].

the normal spacecraft telemetry streams while Sky images are searched to detect sources. BAT compare the sources found in these images against an on-board catalogue of sources. The sources either not listed in the catalogue or showing large variability in the counts are deemed to be transients. Sources that were not found in the on-board catalogue and show a detection are considered to be GRBs.

2.2.2.2 XRT

Another instrument onboard Swift is XRT, the X-Ray Telescope. It was built to measure fluxes and obtain spectra and light curves of GRBs and their afterglows in a wide dynamic range, covering more than 7 orders of magnitude in flux. The XRT pinpoints GRBs to 5-arcsecond accuracy, within ten seconds of target acquisition for a typical GRB. The energy range is from 0.2 to 10 keV, with a 120 cm^2 effective area, 23.6 arcminute FoV and 15-arcsecond resolution at 1.5 keV (Burrows et al. 2000). A summary Table is reported in 2.13.

The XRT uses a Wolter 1 telescope (see Appendix C) to focus X-rays onto a CCD, which is shown in Figure 2.17. The XRT energy resolution at launch was approximately of 140 eV at 6 keV. The XRT supports different operative modes: *imaging mode*, which produces an integrated image measuring the total energy on the CCD and does not allow spectroscopy; *photodiode mode*, which is used to obtain high-timing accuracy for the

FoV	23.6 x 23.6 arcminutes
Energy Range	0.2 - 10 keV
Energy Resolution	$\sim$ 140 eV at 6 keV
Spatial Resolution	3 - 5 arcseconds

Table 2.13: XRT instrumental characteristics (Burrows et al. 2000).

rapidly varying flux from a bright source and allows spectroscopy; and *photon-counting mode* that allows the collection of spatial information and full spectra only if the source overcomes a defined threshold (Burrows et al. 2005).

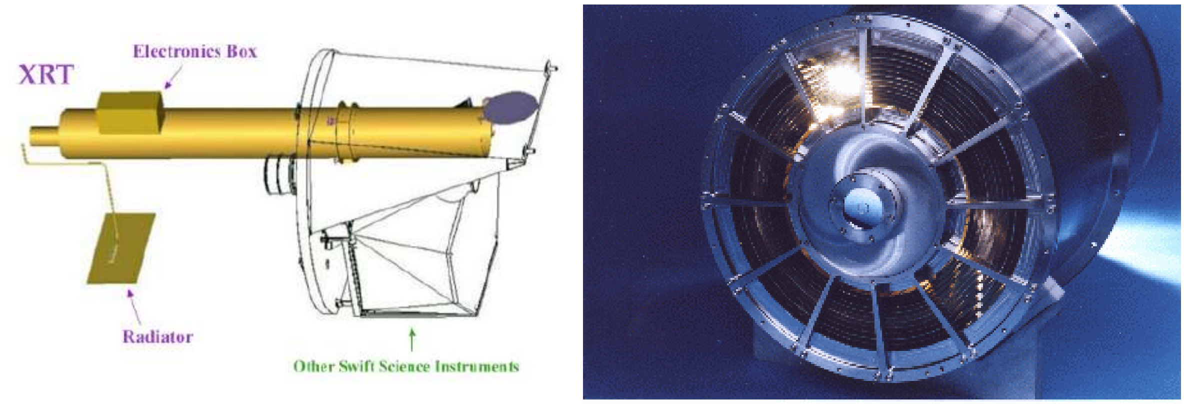

Figure 2.17: Left: schematic representation of XRT telescope inside Swift payload. Image taken from (Burrows et al. 2000). Right: XRT mirror module. It consists of 12 nested Wolter-I grazing incidence mirrors held in position by front and rear support spiders. Image taken from Swift[16].

2.2.2.3 UVOT

The Ultraviolet/Optical Telescope (UVOT), was built with the intention to follow the gamma-ray burst afterglow. It provides the most accurate onboard determination of the burst position ($\leq$ 1 arcsecond accuracy). The UVOT is a 30 cm telescope with intensified CCD detectors. It operates in the wavelength range of 1600-6000 Å(Roming et al. 2005b). The UVOT properties are reported in Table 2.14.
UVOT observations enable optimal ground-based observations by providing rapid optical images of the GRB field so that any optical or UV counterpart can be quickly identified

[16]`https://www.swift.psu.edu/xrt/optics.php`

and studied. UVOT is as sensitive as a 4-meter optical ground-based telescope. Along with XRT, it can determine the distance and collect information about the host galaxies of the burst (Gehrels et al. 2004).

FoV	17 x 17 arcminutes
Wavelength Range	170 - 650 nm
Spectral Resolution	~200-400 nm
Spatial Resolution	2.5 arcseconds

Table 2.14: UVOT instrumental characteristics (Roming et al. 2005a).

The telescope tube contains a 30-cm primary and a 7.2 cm secondary mirror which are both made from Zerodur (Peter W. A. 2005).
UVOT has a filter wheel before the detector with 6 filters, 3 for optical (*v= 550 nm, b= 440 nm, u= 350 nm*) and 3 for UV light (*uvw1= 260 nm, uvw2 =225 nm and uvw3= 193 nm*). Each pixel has a size of 4×4 arcseconds on the sky, thus providing a 17×17 arcminute FoV (Roming et al. 2005a). The UVOT can achieve an approximate PSF FWHM of 2.5 arcsec. A schematic representation of UVOT is shown in Figure 2.18.

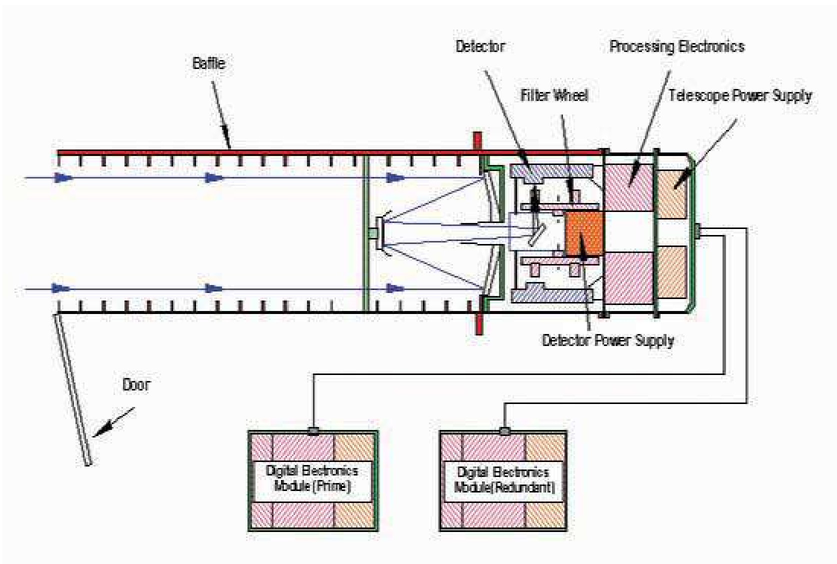

Figure 2.18: A diagram showing the main components of the UVOT telescope. Image taken from (Roming et al. 2005a).

2.2.3 AGILE

AGILE, Figure 2.19, Astro-Rivelatore Gamma a Immagini Leggero, is an Italian mission developed for γ-ray observation (Tavani et al. 2009), launched in 2007. AGILE is light ($\sim$ 350 kg, $\sim$ 130 kg of scientific instrumentation) and effective in detecting and monitoring gamma-ray sources within a large field of view ($\sim$ 1/5 of the whole sky) (Tavani 2002). The instruments onboard AGILE are GRID, Gamma-Ray Imaging Detector, MCAL, Mini-Calorimeter, and the Super-AGILE detector, all surrounded by a plastic scintillator Anticoincidence system for background particle identification.

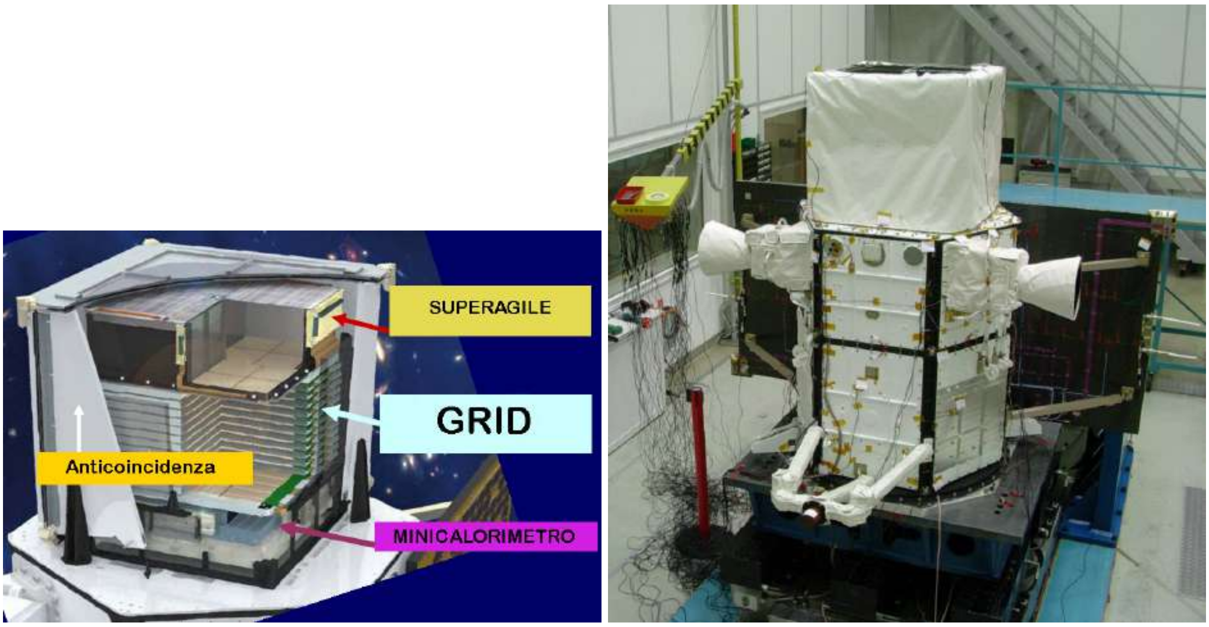

Figure 2.19: Left: A schematic view of the AGILE instruments displaying the hard X-ray imager Super-AGILE, the gamma-ray silicon tracker that is the core of the GRID detector, the mini-calorimeter, and the anticoincidence system. Image taken from IASF-Milano[17]. Right: An image of the model of the AGILE spacecraft in its final configuration before the launch. Image is taken from (Tavani 2019).

[17] https://www.iasf-milano.inaf.it/Divulgazione/divulgazione.php?pg=agile2&mn=agile&lin=gamma_agile

2.2.3.1 GRID

The GRID detector is sensitive in the range of 30 MeV–50 GeV. GRID consists of a Silicon-Tungsten Tracker, a CsI(Tl) based Mini-Calorimeter, a plastic scintillator Anti-coincidence system, and fast readout electronics and processing units. GRID is designed to achieve an angular resolution of $\sim$ 5'–20' for intense sources, an FoV of nearly 3 sr and a sensitivity comparable to EGRET for on-axis. A summary Table of the instrumental characteristic of GRID is reported in Table 2.15.

FoV	$\sim$ 3 sr
Energy Range	30 MeV - 50 GeV
Energy Resolution(at 300 MeV)	ΔE/E $\sim$ 1
Angular Resolution	$\sim$5-10 arcmin

Table 2.15: Instrumental characteristics of GRID (Tavani 2002).

The silicon-tungsten-tracker is made of 12 planes, each plane includes one tungsten layer converting the impinging γ in a e^-, e^+ pair, and two Si layer providing the X and Y coordinates of interacting charged particles (Prest et al. 2003). A section of the Agile payload, including the instrument GRID, is presented in Figure 2.20. The GRID is designed to achieve a nominal spectral resolution Δ E/E $\sim$ near 300 MeV, and energy resolution $\sim$1 MeV below 100 MeV. This result is obtained by combining the information on the particle energy deposited in the Si-Tracker and MCAL (Prest et al. 2003).

2.2.3.2 MCAL

The MCAL (Figure 2.26) can detect photons independently from the GRID, in the energy range of 0.3 to 200 MeV. It is used to provide spectral and accurate timing information of transient events. It is made by 30 Cesium Iodide (CsI(Tl)) bars arranged in two orthogonal planes (Labanti et al. 2006).

The signal from each CsI(Tl) bar is collected by two photodiodes placed at both ends. MCAL can obtain information on the energy deposited in the CsI bars by particles produced in the Silicon Tracker therefore contributing to the determination of the total

Figure 2.20: Left: A schematic view of the AGILE instrument displaying (from the top): the hard X-ray imager Super-AGILE, the gamma-ray silicon tracker that is the core of the GRID detector, and the mini-calorimeter. Image taken from (Tavani 2019). Right: An image of the model of the AGILE instrument (AC system not displayed). Image taken from (Tavani 2002).

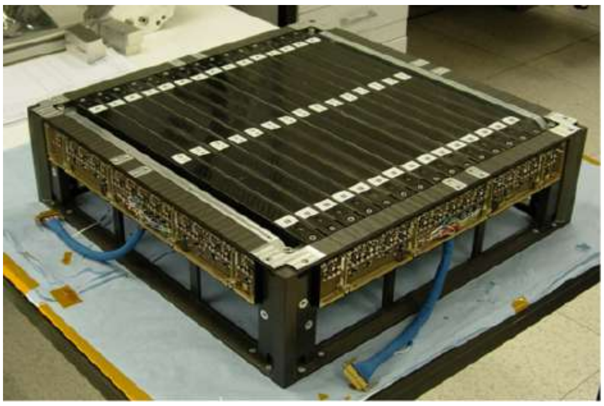

Figure 2.21: Image of the detector MCAL. Image by the courtesy of Labanti.

photon energy, and detect GRBs and other impulsive events with spectral and intensity information (Fuschino et al. 2008). Mini-Calorimeter events detected by CsI bars are of two spectral types: low-energy events, for a single low-energy channel from 250 keV to 1 MeV (for 1-diode detections), and standard events, for an energy range from 1 to $\sim$ 100 MeV band with $\sim$ 1 MeV energy resolution (for 2-diode detections) (Labanti et al. 2006). A summary table of the MCAL instrument is reported in Table 2.16.

FoV	-
Energy Range	0.3-200 MeV
Energy Resolution	1 MeV
Angular Resolution	-

Table 2.16: Instrumental characteristic of MCAL (Labanti et al. 2006).

2.2.3.3 Super-AGILE

Another instrument is the Super-AGILE detector. It consists of a plane of four Silicon square (19×19 cm^2 each, similar to those of the Tracker) units positioned on top of the GRID Tracker plus an ultra-light Tungsten coded mask at a distance of 14 cm from the Silicon detectors (Costa et al. 2001). An image of the stand-alone detector Super-AGILE is reported in image 2.22. Super-AGILE operates in the 10-40 keV band with an angular resolution of 6 arcminutes (pixel size), and an energy resolution of nearly 3 keV (Feroci et al. 2007). A summary Table with the characteristics of Super-AGILE is reported in 2.17.

FoV	$107° \times 68°$
Energy Range	10-40 keV
Energy Resolution	ΔE $<$ 4 keV
Spatial Resolution	-

Table 2.17: Super- AGILE instrumental characteristics (Feroci et al. 2007).

During its operations, AGILE surveyed the gamma-ray sky and detected many galactic and extra-galactic sources: AGILE discovered the gamma-ray emission from the microquasar Cygnus X-3 (Tavani et al. 2009), detected many bright blazars, discovered several new gamma-ray pulsars, and discovered emission up to 100 MeV from Terrestrial Gamma-Ray Flashes (Marisaldi et al. 2010).

2.2.4 Fermi Gamma Ray Observatory

The Fermi Gamma Ray Observatory, Figure 2.23, was launched in 2008 by NASA and is dedicated to γ-ray observation and depicted in GRBs. Fermi has two main instruments,

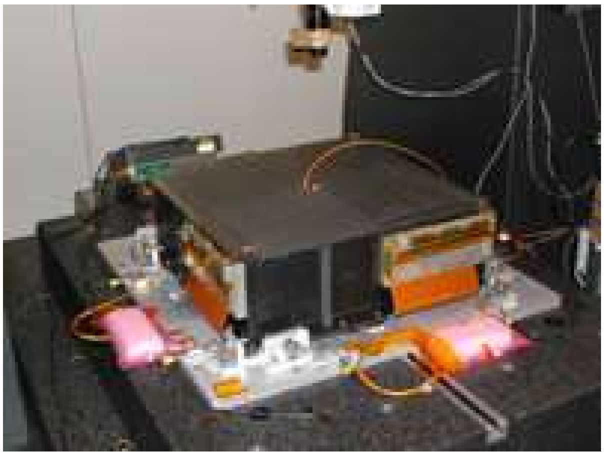

Figure 2.22: Image of the detector Super-Agile. Image taken from IASF-Milano[18]

the LAT, Large Area Telescope, and GBM, Gamma-ray Burst Monitor.

Figure 2.23: Left: an image of the Fermi spacecraft (taken from NASA[19]). Right: a diagram showing the position of the payloads onboard the Fermi spacecraft. Image taken from NASA[20].

[18] https://www.iasf-milano.inaf.it/Divulgazione/divulgazione.php?pg=agile2&mn=agile&lin=gamma_agile

[19] https://science.nasa.gov/get-involved/toolkits/spacecraft-icons

[20] https://imagine.gsfc.nasa.gov/observatories/learning/fermi/multimedia/spacecraft_gallery.html

2.2.4.1 LAT

The LAT instrument is Fermi's primary instrument. The LAT has 3 subsystems that work at the same time to detect gamma rays and reject cosmic rays, a tracker, a calorimeter and an anticoincidence detector.
The LAT instrument has a very large FoV of over 2 steradians to observe about one-fifth of the sky at any given moment. In sky-survey mode, which is the primary observing mode, the LAT covers the entire sky every three hours. The observatory can also be pointed at targets of opportunity and can slew autonomously when either instrument detects sufficiently bright GRBs. The LAT energy range is from 20 MeV to 300 GeV (Atwood et al. 2009).
The LAT has a precision gamma-ray converter tracker and calorimeter, each consisting of a 4×4 array of 16 modules. The technology used enables straightforward determination of the direction of the incident photon (Atwood et al. 2009), based on the same principle described in AGILE. A gamma photon entering the tracker is converted in a particle pair (electron and positron) by a foil of high-z converter material (Tungsten) placed above a tracking plane. The tracking plane consists of two layers (x and y) of single-sided silicon strip detectors. The converter planes are interleaved with position-sensitive Si detectors that record the passage of charged particles, thus measuring the tracks of the particles resulting from pair conversion. The pair conversion signature is also used to the rejection of the much larger background of charged cosmic rays. An image of LAT and its working principle is reported in 2.24.

The calorimeter below the tracker has the purpose of measuring the energy of the tracked particles and making a 3-dimensional representation of the electromagnetic shower that these particles produce in the heavy material of the calorimeter, providing an important background discriminator and an estimator of the shower energy leakage fluctuations. Each calorimeter module has 8 layers of 12 CsI(Tl) crystals. Each crystal element is read out by PIN photodiodes, mounted on both ends of the crystal, which measures the scintillation light. The difference in light levels provides a determination of the position of the energy deposition along the CsI crystal (Atwood et al. 2009). A summary Table with the instrumental characteristics is reported in 2.18

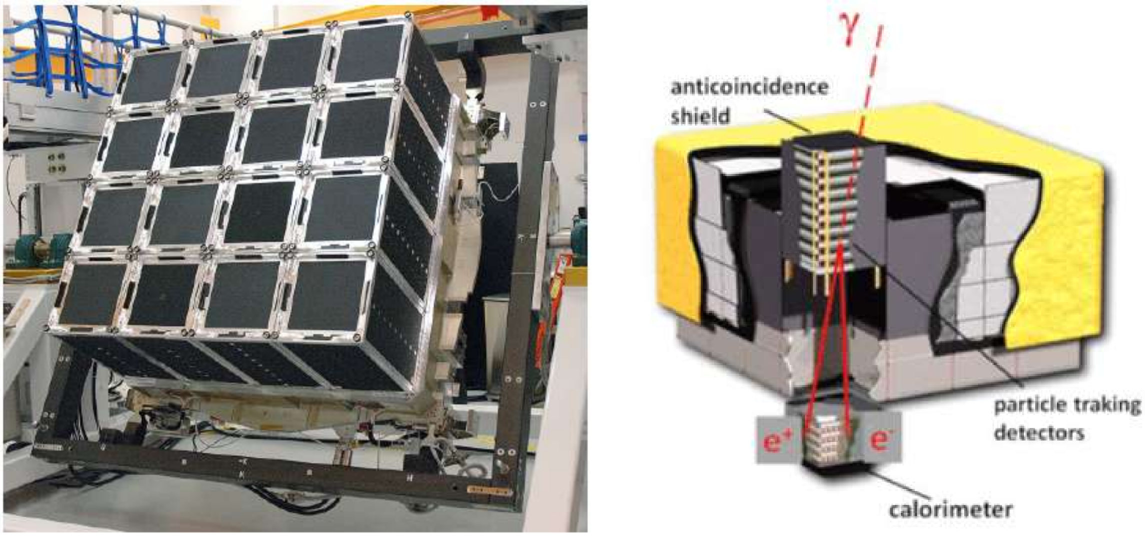

Figure 2.24: Left: image of LAT (Atwood et al. 2009). Right: diagram showing the detection mechanism implemented by LAT. Image taken from (Atwood et al. 2009).

FoV	2.4 sr
Energy Range	20 MeV–300 GeV
Energy Resolution(100 MeV–1 GeV)	9%-15%
Energy Resolution(1 GeV–10 GeV)	8%-9%
Energy Resolution(10 GeV–300 GeV)	8.5%-18%
Spatial Resolution	$\sim$ 10 arcminute

Table 2.18: Fermi-LAT instrumental characteristics.(Atwood et al. 2009).

2.2.4.2 GBM

Another instrument onboard Fermi is GBM (Gamma Burst Monitor), which operates in the range of 8 keV to 30 MeV. This wide energy band is achieved thanks to an arrangement of 12 thin NaI(Tl) detectors which are inclined to each other to derive the position of GRBs from the measured relative counting rates and to get the low-energy spectrum in the range $\sim$8 keV to $\sim$ 1 MeV. The cylindrical NaI crystals have a diameter of 12.7 cm and a thickness of 1.27 cm. To fill the gap between the GRBM and LAT energy ranges, two Bismuth Germanate Oxide (BGO) detectors are mounted on two opposite sides of the GLAST spacecraft consisting of BGO crystals which are sensitive to γ-rays from $\sim$150 keV to $\sim$30 MeV (Meegan et al. 2009). A summary table of the characteristics of

GBM is reported in 2.19. Images of the BGO and NaI detectors are reported in Figure 2.25.

FoV	9.5 sr
Energy Range	~8 keV - 30 MeV
Energy Resolution(at 511 keV)	12% FWHM
Angular Resolution	-

Table 2.19: Fermi- GBM instrumental characteristics (Meegan et al. 2009).

The Fermi telescope has brought a significant amount of new discoveries, such as the creation of a catalogue of more than 5800 sources, the Milky Way Gamma and X-ray Fermi bubbles and the observations of numerous TGF, Terrestrial Gamma-ray Flashes (Abdollahi et al. 2020). Fermi is also known for the observation of numerous GRBs, in particular the GRB 170817A. (Abbott et al. 2017).

Figure 2.25: Left: An image of the system integration of the Fermi-GBM both BGO and NaI detectors. Right: an image of isolated NaI detectors. Images taken from NASA[21].

2.3 The future: THESEUS

Nowadays, both ESA and ASI are preparing mission concepts dedicated to high-energies and detections of GRBs. In particular, they aim at detecting GRBs with unprecedented

[21] `https://gammaray.nsstc.nasa.gov/gbm/instrument/`

timing and positional accuracy, in order to properly assess the prompt emission. The study of the prompt emission of GRB is crucial to determine the emission mechanisms (through temporal and spectral characterization), which in turn can give clues to the nature of the progenitors. These studies require a broad energy band, from ∼1 keV to ∼1 MeV, and a good energy resolution (ESA/SCI 2021). The THESEUS mission concept is a candidate on the current ESA M7 call mission opportunity.

2.3.1 The THESEUS Mission

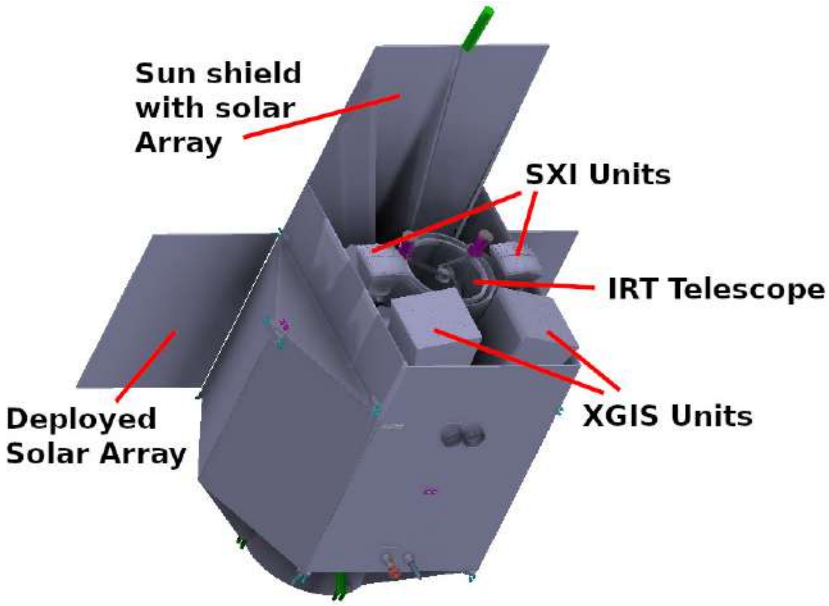

Figure 2.26: Schematic view of the spacecraft design of THESEUS. Image taken from ESA/SCI (2021)

THESEUS, Transient High-Energy Sky and Early Universe Surveyor, is a proposed space mission developed by a large European collaboration and submitted in 2017 to ESA, for the M5 call within the Cosmic Vision Program. In 2018, THESEUS, along with other two mission concepts was selected by ESA for a 3-year Phase A assessment study. Unfortunately, it was not selected in 2021 for launch . THESEUS was re-proposed for the ESA M7 call. Currently, it has just concluded the preliminary phase 0, undergoing the CDF (Concurrent Design Facility) study, and is pending the ESA decision for admission to the next phase A of the selection.

THESEUS aims at entering the Cosmic Vision program [22] by fully exploiting GRB observations to solve key questions about the early Universe, as well as becoming a cornerstone of multi-messenger and time-domain astrophysics. THESEUS will provide a substantial advancement in the study of Gravitational Waves (GW) and neutrinos by enabling the identification, accurate localization, and study of electromagnetic counterpart of those sources. THESEUS will work with the second and third generation of GW interferometers and future neutrino detectors. Under all these respects, THESEUS will provide great synergies with future large observing facilities in the multi-messenger domain.
These goals will be achieved by a payload and mission profile providing a combination of: wide and deep sky monitoring in a very broad energy band (0.3 keV - 10 MeV), providing large grasp and high angular resolution, onboard near-IR capabilities for immediate transient identification, arcsecond localization, and redshift determination; a high-degree of spacecraft autonomy and agility, together with the capability of promptly transmitting to ground transient trigger information.
The scientific goals for the exploration of the early Universe require the detection, identification, and characterization of several tens of GRBs that occurred in the first billion years of the Universe (z>6) within the 4 years of nominal mission lifetime of THESEUS, combined with intensive follow-up programs from the ground (ESA/SCI 2021). The main improvements with respect to previous missions are shown in Table 2.20.

One of the most significant limitations in the precedent missions is the waveband coverage. To cover both the prompt and afterglow emissions from GRBs, past missions had to point more than one single instrument to the source (see Sections 2.1, 2.2). Following the heritage of Beppo-SAX, and Swift, and considering the importance of rapidly detecting GRBs, THESEUS aims at covering from soft X-rays (2 keV) to soft γ-rays (10 MeV), increasing the sensitivity by at least one order of magnitude concerning previously wide-field X-ray monitors. Another goal consists in the improvement of the efficiency of counterpart detection, spectroscopy (in the wide spectral window), and redshift measurement through prompt onboard NIR follow-up observations, using the IRT instrument (Section 2.31). Moreover, THESEUS will be able to detect and quickly localize short GRBs over a large FoV (ESA/SCI 2021).
The THESEUS payload will include the following scientific instruments:

[22] `https://www.esa.int/Science_Exploration/Space_Science/ESA_s_Cosmic_Vision`

Mission	Autonomous rapid repointing	Arcsec localisation	Optical imaging	Near-IR imaging	Near-IR spectroscopy	On-board redshift broadcasting	<10 keV X-ray coverage	>10 keV X-ray coverage	MeV γ-ray coverage	Energy Resolution
CGRO BATSE	×	×	×	×	×	×	×	✓	✓	at 660 keV 8 %
SWIFT BAT	✓	✓	✓	×	×	×	✓	✓	×	at 60 keV 3.3 keV
Fermi GBM	×	×	×	×	×	×	×	✓	✓	at 511 keV 12 %
INTEGRAL IBIS	×	×	✓	×	×	×	×	✓	✓	at 100 keV 9 keV
Beppo-SAX GRBM	×	×	×	×	×	×	✓	✓	×	at 511 keV 16 %
THESEUS XGIS	✓	✓	✓	✓	✓	✓	✓	✓	✓	at 500 keV ≤ 6 %

Table 2.20: GRB detection performance of THESEUS (ESA/SCI 2021) compared with past and current high-energy space missions (se Chapter 2).

- **Soft X-ray Imager (SXI)** (0.3-5 keV): a set of two “Lobster-eye” monitor units, covering a total FoV of $\sim$ 0.5sr with source location accuracy of 0.2 arcminutes;
- **X-Gamma rays Imaging Spectrometer (XGIS)** (2 keV- 10 MeV): a set of two coded-mask monitor cameras using a combination of solid state and scintillator detectors detectors, granting a $\sim 2\pi$ sr imaging FoV and a source location accuracy <15 arcmin in 2-150 keV, an energy band from 2 keV up to 10 MeV, and a few μs timing resolution;
- **InfraRed Telescope (IRT)** (0.7-1.8 μm): a 0.7 m class IR telescope with 15’×15’ FoV, and position accuracy of 5 arcsecond, with imaging and spectroscopy capabilities.

The main requirements for the instruments onboard THESEUS are shown in Table 2.21.

SXI sensitivity (3σ)	1.8x10^{-11} erg/cm^2/s (0.3-5 keV, 1500 s)
SXI FoV	0.5 sr
SXI positional accuracy (0.3-5 keV)	$\leq$ 2 arcminutes
XGIS sensitivity (1s, 3σ)	10^{-8} erg/cm^2/s (2-30 keV) 3x10^{-8} erg/cm^2/s (30-150 keV) 2.7x 10^{-7} erg/cm^2/s (150 keV-1 MeV)
XGIS FoV	77×77 deg^2 (2-150 keV) 2π sr ($\geq$ 150 keV)
XGIS positional accuracy (2-150 keV)	$\leq$7 arcminutes(50% of the triggered sGRB) $\leq$15 arcminutes(90% of the triggered sGRB)
IRT sensitivity (imaging, SNR=5, 150 s)	20.9 (I), 20.7 (Z), 20.4 (Y), 20.7 (J), 20.8 (H)
IRT field-of-view	15’x15’
IRT positional accuracy (5σ detections)	$\leq$5 arcsecond (real-time) $\leq$1 arcsecond (post-processing)

Table 2.21: Scientific requirements for the instruments onboard THESEUS (ESA/SCI 2021).

The mission operation concept includes a *Survey mode*, during which the monitors are chasing GRBs and other transients of interest. Following a GRB trigger validated by the Data Handling Units (DHU) system the spacecraft enters in *Burst mode* (slewing the spacecraft so to bring the GRB into IRT FoV), followed by IRT observing sequence (*Follow-up and Characterization or Deep Imaging modes*). The pointing strategy during the Survey mode will be to maximize the combined efficiency of SXI and XGIS and that of the follow-up with the IRT. In the next subsections, we will present the instruments onboard THESEUS.

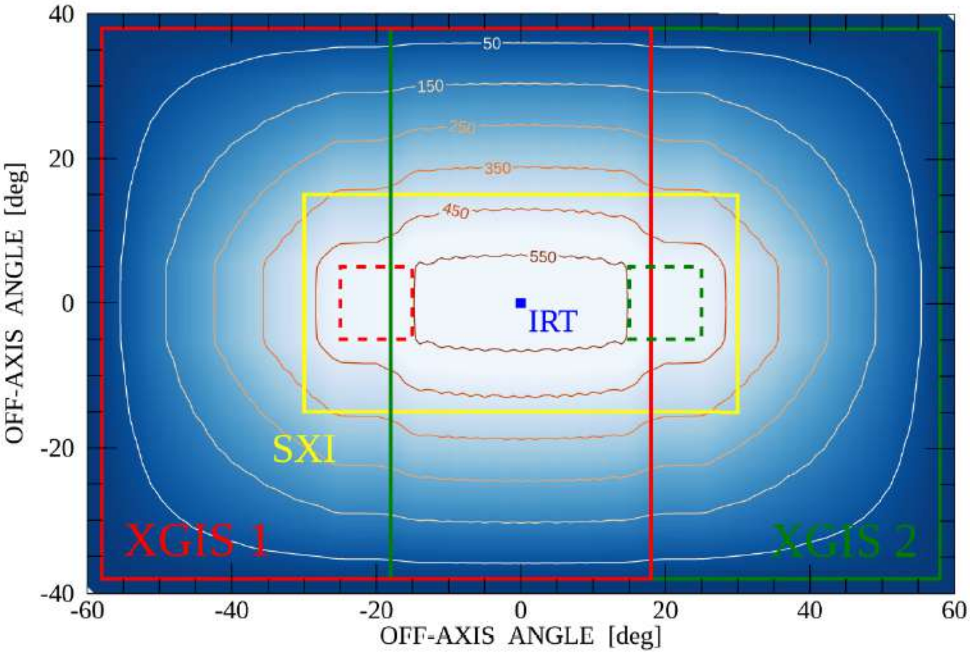

Figure 2.27: Fields of view of the THESEUS instruments. The red (left) and green (right) squares indicate the partially coded FoV (77×77 deg^2, solid lines) and fully coded FoV (11×11 deg^2, dashed lines) of the two XGIS units. The yellow rectangle is the SXI FoV (61×31 deg^2). The blue square indicates the pointing direction of the IRT. The contour lines indicate the effective area at 10 keV provided by the sum of the two XGIS units, assuming a 50% open fraction for the coded masks (Mereghetti et al. 2021).

2.3.1.1 SXI

SXI, Soft X-ray Imager, will be composed of two identical modules as shown in Figure 2.28. The SXI is made by a consortium of scientists from ESA member states, led by the UK, including Belgium, Spain, Switzerland and the Czech Republic. Each module is a wide-field, “Lobster eye” X-ray telescope, an X-ray imaging principle that allows a

FoV as large as desired and it is practical to achieve good efficiency for photon energies up to 6 keV.

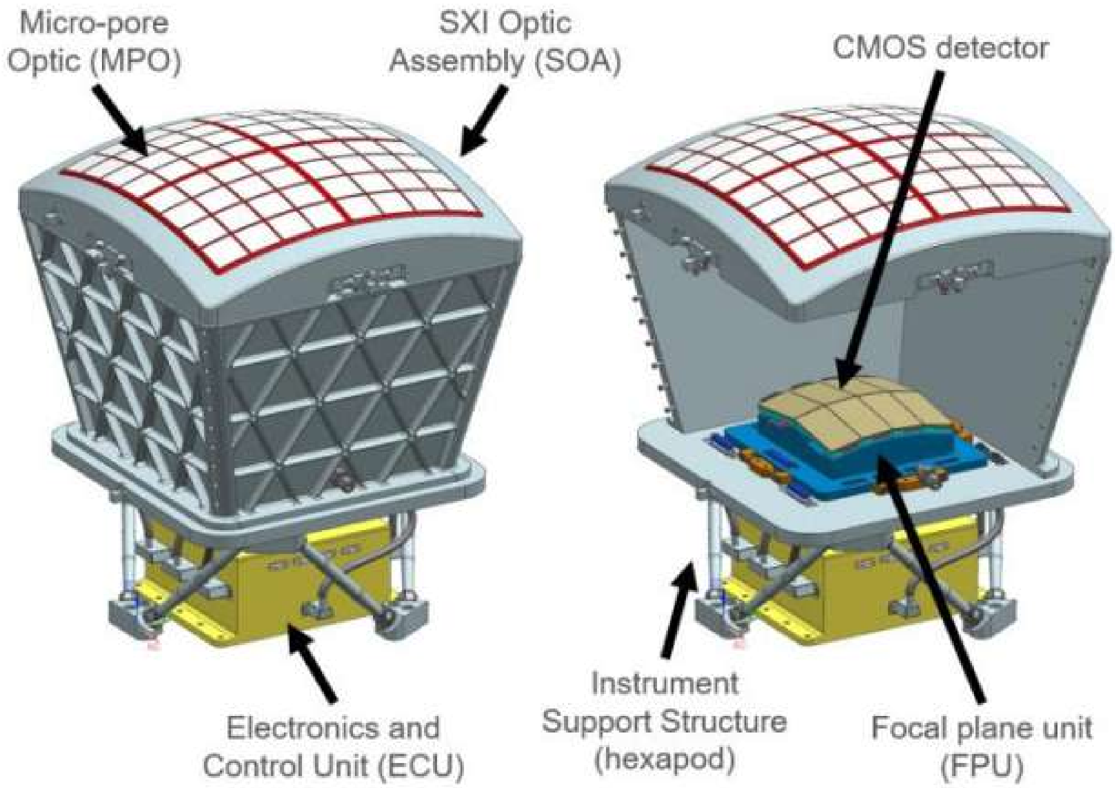

Figure 2.28: Left: SXI module exterior view. Right: focal plane assembly located below the optics assembly. The electronics box is shown here below the focal plane within the structure of the spacecraft. Images taken from (ESA/SCI 2021)

The optics consist of many small tubes, of square cross-section and with reflective internal surfaces, arranged over a spherical surface with their axes radially aligned (Angel 1979).
This configuration provides for a wide FoV, focusing X-ray imaging system with an effective area maintained across the entire FoV. The optics aperture for the SXI modules is formed by an array of 8×8 square micro-pore optics mounted on a spherical frame with a radius of curvature of 600 mm.

The lobster eyes configuration yields a PSF cross-arm (Figure 2.30), because the X photons reflected by the micro-pore walls are focused in lines or columns on the focal plane forming a cross. In this configuration some 75% of the incident X-rays are focused.

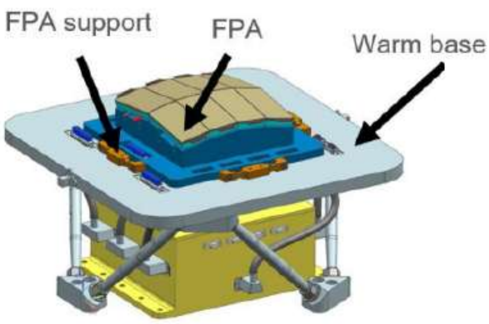

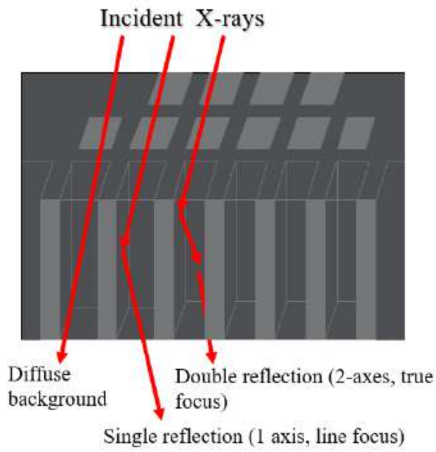

Figure 2.29: Left: Focal Plane Assembly of SXI. Image taken from (ESA/SCI 2021) Right: Schematic view of a photon interacting with the square pore MCP of SXI. Image curtesy of O'Brien P.

The FoV of SXI will be of 0.25 steradians (31° ×31°) per module. The 2 modules will be aligned on the sky, with a 1° wide overlap on one side (O'Brien et al. 2021).

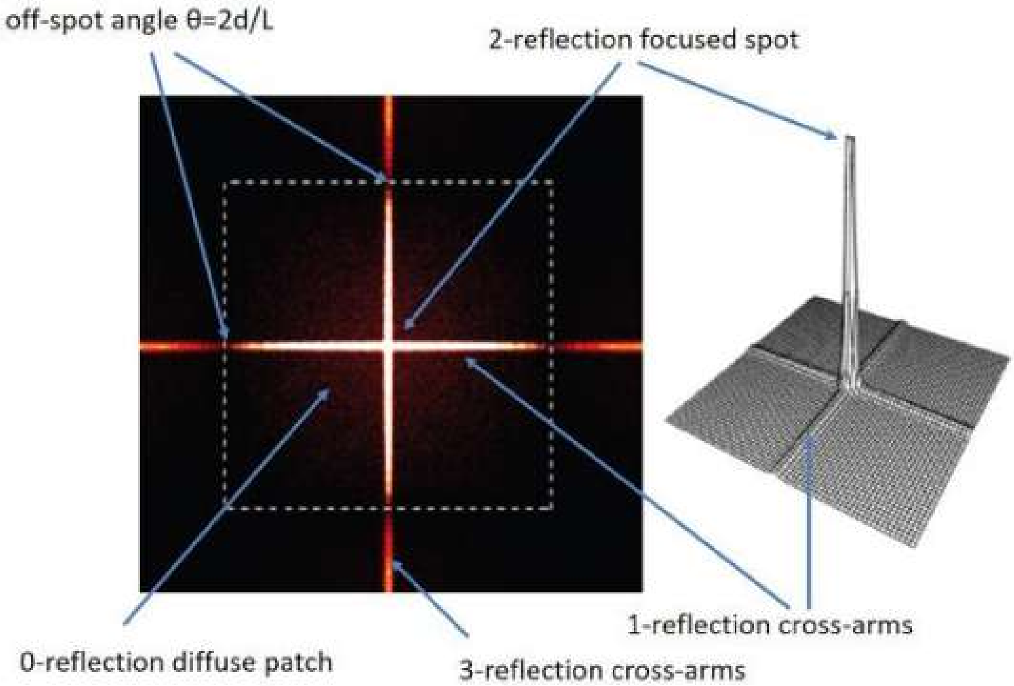

Figure 2.30: Left: The MPO point spread function showing the cross-arm shape. Right: The inner dotted square where the PSF cross-arms. Images taken from (O'Brien et al. 2021).

Ray-tracing simulations across the 0.3–6 keV energy range show that the SXI effective area peaks at 1 keV and that the optics exhibit an FWHM of 6 arcmins at the peak energy (O'Brien et al. 2021). As is shown in figure 2.27 SXI has a better angular resolution than the IRT's FoV, so with the slewing THESEUS can get the burst into the FoV of IRT. In the case of XGIS, this does not happen because the angular precision of XGIS is worse than the FoV of IRT. SXI will also search for X-ray transients associated with multi-messenger sources and monitor the X-ray sky (Amati et al. 2018).

2.3.1.2 XGIS

XGIS, X/γ-ray Imaging Spectrometer, is a high-energy detector capable of covering an exceptionally wide energy band (2 keV – 10 MeV), with imaging capabilities and location accuracy < 3 arcmin up to 150 keV over a Field of View of 2sr (see Figure 2.27), a few hundred eV energy resolution in the X-ray band at 6 keV, less than 6% at 600 keV and a few micro-seconds time resolution over the whole energy band (Amati et al. 2022).

Energy Range	2-150 keV	150-10 MeV
Partially coded FOV	117×77 deg^2	
FOV		2π sr
Peak effective area	~ 500 cm^2	~ 1000 cm^2
XGIS sensitivity (two combined cameras)	At EoL at least $10^{-}8$ cgs over the 2–30 keV range in 1 s for 99.73% of the observations and at least 3x$10^{-}8$ cgs over the 30–150 keV range in 1 s for 99.73% of the observations	at least 3x $10^{-}7$ cgs over the 150 keV- 1 MeV energy range in 1 s for 99.73% of the observations
Source location accuracy	$\leq$ 15 arcmin 90% confidence level in the 2-150 keV energy band for a source with SNR >7	
Energy resolution	Better than 1200 eV FWHM at 6 keV at End of Life	6 % FWHM at 500 keV
Relative timing accuracy	7 μs	

Table 2.22: Main characteristics of each XGIS camera (Labanti et al. 2021a).

The most relevant XGIS requirements (Labanti et al. 2021b) are:

- The total peak effective area of the two XGIS units shall be equal or larger than > 500 cm^2 in the 2–150 keV energy range.
- The total peak effective area of the two XGIS units shall be equal to or larger than > 1000 cm^2 above 150 keV.

- The effective area shall be known to an accuracy of 10 % over the interval 2–150 keV. The effective area will be known to an accuracy of 15 % above 150 keV.
- The energy range shall be 2 keV–10 MeV.
- The XGIS shall have imaging capabilities up to 150 keV.
- The instrument will provide an energy resolution $\leq$1200 eV (goal of 300 eV) FWHM at 6 keV End of Life (EoL) and less than 6% at 600 keV.
- The XGIS will have a total FoV 117x 77 deg^2 FWHM in the 2–150 keV energy band.
- The XGIS will have a total FoV of 2π sr above 150 keV.
- The detector operating temperature, referred to as the SDD top plane, shall be from –30 °C to +10 °C

The large waveband, the high energy resolution for spectroscopy, the coded mask imaging system joined to the detection plane, and the modularity of the design grant great flexibility in adapting the XGIS configuration for specific scientific objectives and available resources (e.g., inclusion in the payload of a medium/large mission or a dedicated "stand-alone" small satellite, Amati et al. 2022).
The XGIS realisation design and construction is in charge of international consortium lead by OAS-INAF Bologna, the XGIS architecture and operating principle will be described in detail in Chapter 3.

2.3.1.3 IRT

The InfraRed Telescope (IRT) on board THESEUS is designed to identify, localize and study transients and especially their afterglows detected by the Soft X-ray Imager (SXI) and the X and γ Imaging Spectrometer (XGIS). The SXI is made by a consortium lead by France, in collaboration with Switzerland and Germany.
It will also be able to measure, onboard, the redshift of each source. The IRT instrument consists of the IRT-CAM and the IRT Data Handling Unit (IRT-DHU). The telescope (optics and tube assembly) can be made of SiC, a material that has been used in other space missions such as Gaia, SPICA, and Herschel (Amati et al. 2018). IRT is a 70

cm Korsch telescope as shown in Figure 2.31. The optical design will implement two separate fields of view, one for photometry with a minimal size of 15×15 arcmin and one for spectroscopy of 2×2 arcmin. On the photometric field of view, the IRT will be able to acquire images using five different filters (I, Z, Y, J, and H) and on the spectroscopic field of view, the IRT will provide spectroscopy in the 0.8-1.6 μm range.

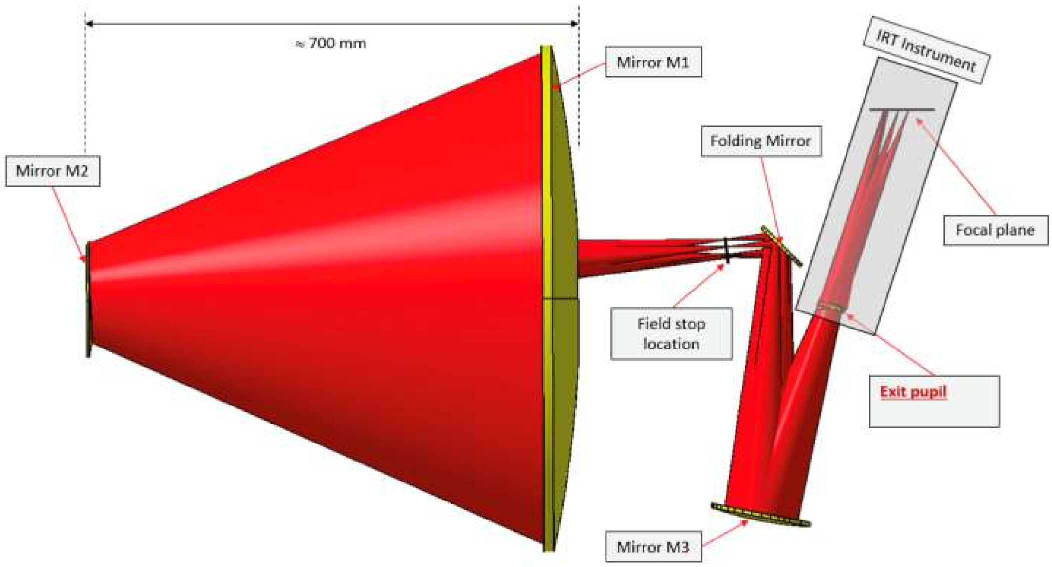

Figure 2.31: IRT Optical scheme. The exit pupil represents the optical interface with the IRT-CAM. Image taken from (ESA/SCI 2021).

Once a GRB is detected by the SXI and/or the XGIS, a slew is requested to the platform to place the GRB error box within the IRT photometric FoV. Then the IRT enters the *follow-up* mode, an exposure of 150-s duration is made in each of the available filters and acquired. Thanks to these images and an onboard catalogue (based on Gaia surveys), the IRT will be able to autonomously identify the GRB afterglow candidate and compute its coordinates and its photometric redshift. Then, as a function of the source flux, the IRT enters the characterization mode, which includes an observation in the spectroscopy mode for 1800 s followed by 1800 s of deep imaging. To activate the spectroscopic mode, the satellite needs to perform a small slew to put the afterglow positions within the 2×2 arcmin spectroscopic FoV (Amati et al. 2018). A schematic model of the science operation of IRT after a GRB trigger is shown in figure 2.32

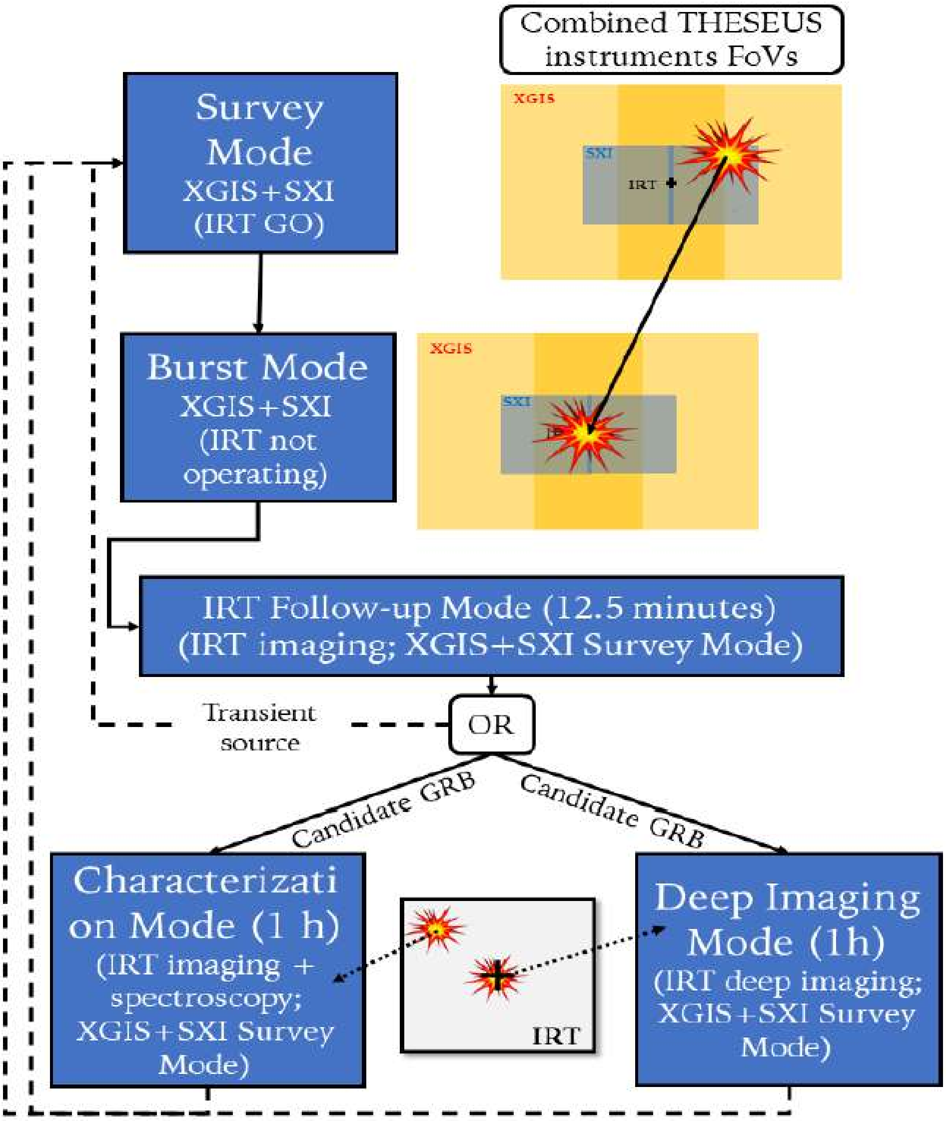

Figure 2.32: Diagram with the THESEUS science operations after a GRB trigger and the pinpoint (ESA/SCI 2021).

Chapter 3

THESEUS/XGIS

In this chapter, we will describe the XGIS instrument onboard THESEUS. We will present the architecture and working principle of XGIS in Section 3.1. We will describe the building blocks of XGIS such as silicon detectors in Section 3.2 with a focus on PN junctions and SDD in sections 3.2.1 and 3.2.2, respectively. The scintillators will be described in Section 3.3.
We will present the siswich working principle and its application in THESEUS/XGIS, and its readout through the ORION chipset in Sections 3.4 and 3.5.

3.1 Architecture and Working Principle

XGIS, X/Gamma-ray Imaging Spectrometer onboard THESEUS, has implemented two X/gamma-ray cameras (Figure 3.1), two power supply box (XSU), and a Data Handling Unit (DHU). Each XGIS camera is powered by its dedicated XSU and is directly connected to the DHU. XGIS has imaging capabilities up to 150 keV, with a FoV larger than and fully overlapping with the SXI one, and has spectrometric capabilities covering a wide energy range from 2 keV to 10 MeV, partially overlapping with the SXI in the soft X-rays.
The detector modules are the key elements of the XGIS units. Their architecture is based on elements already used in previous experiments like INTEGRAL and AGILE, but updated with new technologies, such as SDDs and low noise front-end electronics.

Each camera (see Figure 3.1), is composed of a Coded Mask, and a Collimator assembly,

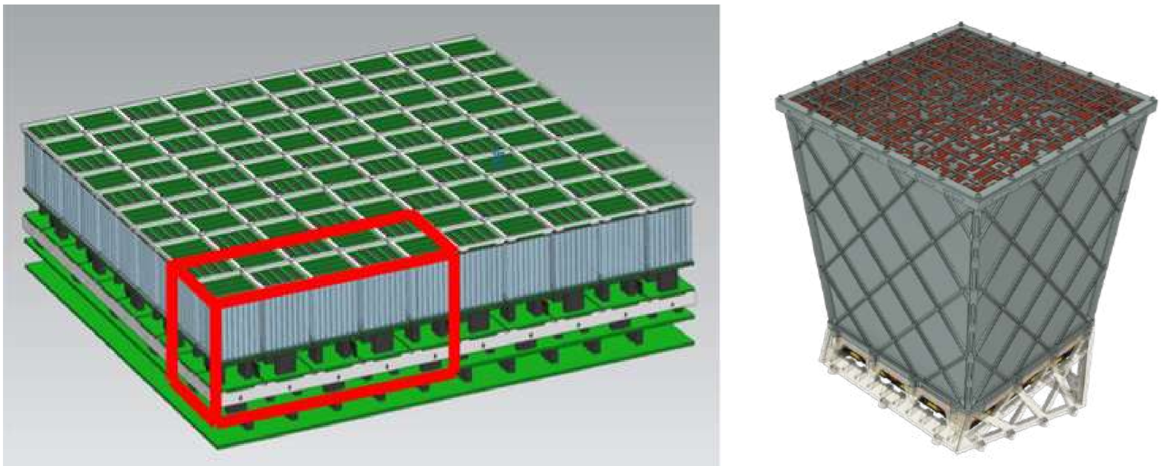

Figure 3.1: Left: Image of the detector plane of XGIS, where are highlighted 10 modules of XGIS. Image taken from (Fuschino et al. 2021). Right: Sketch of an XGIS camera, with the coded mask. Image taken from (ESA/SCI 2021).

and a Detector. The overall Camera size is 60×60×91 cm^3 for a total weight of about 80 kg with a consumption power of $\sim$ 120 W, including the margin. The camera Modules and Super-Modules are organized in a way to achieve a high level of redundancy.
As an imager, XGIS is based on the coded mask principle, with the mask shadowgram being recorded by a position-sensitive detector, that can then be deconvolved into a sky image. The 1 mm thick Tungsten coded mask has an envelope of 600×600 mm^2 with a self-supporting pattern while guaranteeing maximum transparency. The collimator assembly defining the FoV up to 150 keV, is made of Coded Mask Assembly of 0.25 mm thick tungsten slabs that act as a lateral passive shield for the XGIS Imaging System and a support structure.
The imaging sensitivity of a single XGIS camera depends on the position of the source within the FoV, as it is influenced by the 'working area' of the detector. This working area corresponds to the region of the detector that measures the flux modulated by the coded mask and is determined by the source's off-axis angle (Labanti et al. 2021a).

The two cameras of XGIS are misaligned by $\pm 20°$ to IRT, thus providing a total FoV below 150 keV of 117×77 deg^2.
Above 150 keV, the mask and the collimator of an XGIS camera become transparent, thus the imaging capabilities are lost. In the fully coded field of view (FCFOV), the working area coincides with the whole detection plane, and therefore it has the same

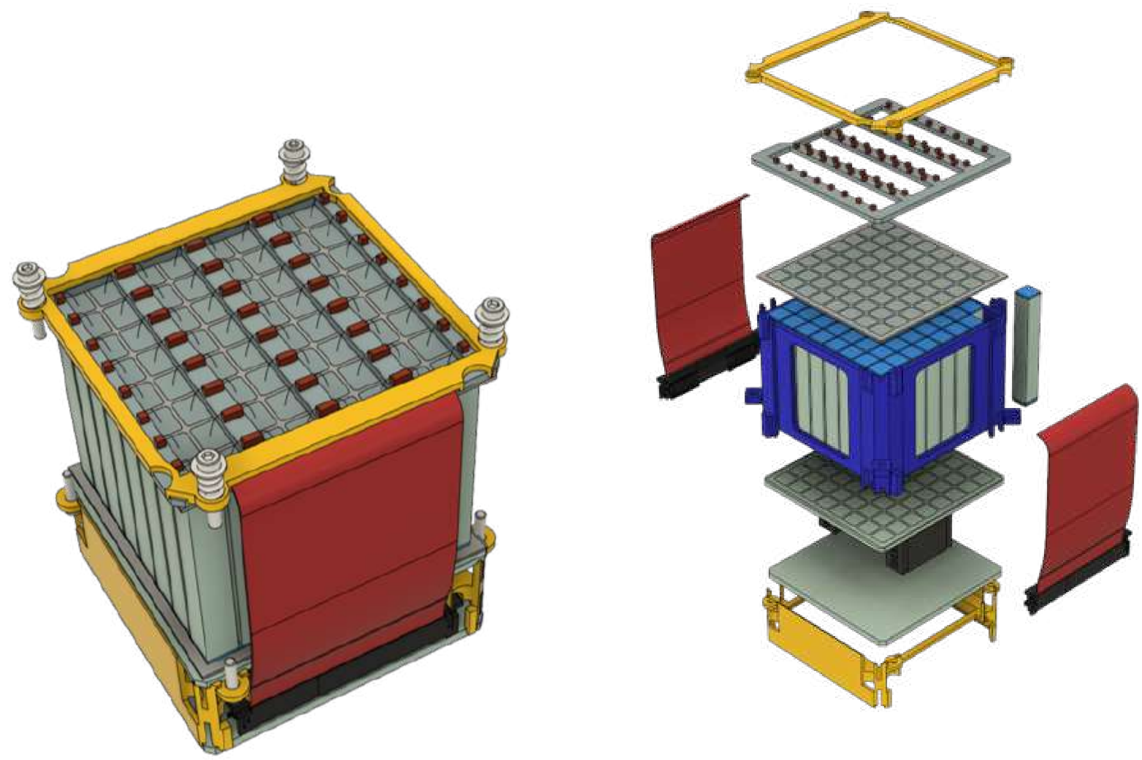

Figure 3.2: Left: Image of a single XGIS detector module design assembled. Right: Image of a single detector module design disassembled. Image given by the courtesy of F. Mele (PoliMi).

dimensions. Therefore, the sensitivity in the FCFOV is approximately constant. For sources outside the FCFOV, the working area is only a fraction of the detector, going linearly to zero for off-axis sources.

The Module (Figures 3.2 and 3.7) is the basic element of the detector plane, it contains all the active detection elements, the autonomous pixels, the electronics circuits for full signal analysis and the mechanical frames for the detector and electronics components. Each module consists of an array of 8×8 individual pixels: two Silicon Drift Detectors (SDDs, Section 3.2.2) that are optically coupled through transparent silicone layers to the scintillator crystals CsI(Tl) (3 cm thick). A crystal wrapping optically insulates one crystal to the others so that the scintillation light of one crystal can reach only its two coupled SDDs. An unique complex Printed Circuit Board made with both stiff and flexible elements routes the electrical signals; a mechanical frame guarantee the assembly of these components. The XGIS SDD has a square cross-section 5×5 mm^2 while the scintillator crystal is $4.5 \times 4.5 \times 30$ mm^3 in size.

3.2 Silicon detectors

Semiconductor detectors are Solid-State Detectors based on the crystalline structure of the material. The most commonly used for designing radiation detectors are Silicon, Germanium or CdTe. They offer several advantages, such as energy resolution, compact size, relatively fast timing characteristics, and an effective thickness that can vary depending on the needs of the application (Knoll 2010). The main property of these detectors is the structure of the energy bands since the electrical behaviour of a material is determined by the occupation of its electronic bands. As shown in Figure 3.3, semiconductors are characterized by the presence of two bands: the valence band which is completely occupied by electrons, and the conduction band, which is at higher energies and empty and it is separated from the first one by a region in which there are no allowed electronic states. The forbidden region is called gap and its energy extension is called gap energy, E_{gap}. The E_{gap} is characteristic of semiconductor material. The semiconductor is neutrally charged, this means that, as the negatively charged electron breaks away from its covalent bonding position, a positively charged "empty state" is created in the original covalent bonding position in the valence band (Neamen 2012). An electron in the valence band to *jump* in the conduction band must have a kinetic energy greater than E_{gap}.

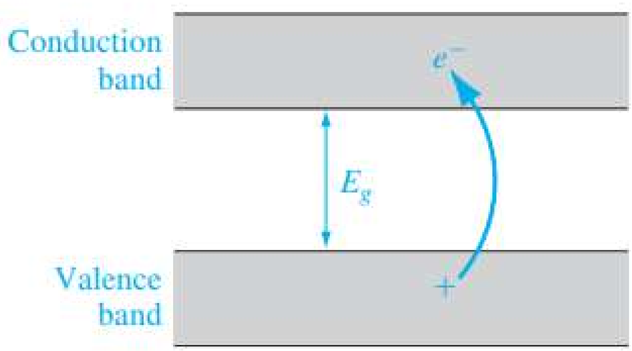

Figure 3.3: Diagram of the band gap energy between the Valence band (low) and Conduction band (high). Image taken from Neamen (2012).

At any temperature, a valence electron can gain sufficient thermal energy to be promoted to a state in the conduction band, by crossing the E_{gap}, as shown in Figure 3.3. This excitation process creates an electron in the conduction band and also leaves a hole in the valence band, the combination of the two is called an electron-hole pair. Electrons in the conduction band and valence-band holes can move under the action of an applied electric field in opposite directions.

In an intrinsic semiconductor, the number of electrons and holes are equal. It is convenient to introduce some impurities to the semiconductor to change the balance of the carriers, varying the conductivity. This means introducing a small percentage of atoms of different and appropriate chemical species. The impurity atom donates an electron to the conduction band and so is called a donor impurity atom (Neamen 2012).

3.2.1 PN junction

The simplest possible junction is a step-like region where the doping concentration is uniform in each region and there is an abrupt change in doping at the junction. The concentration gradient that is created determines a diffusion current of the two types of carriers. The majority of carrier electrons in the n region will begin diffusing into the p region, and the majority of carrier holes in the p region will begin diffusing into the n region, as shown in Figure 3.4. The net positive and negative charges in the n and p regions induce an electric field in the region near the p-n junction, in the direction from the positive to the negative charge, or from the n to the p region . This creates a gradient of an electric field across the junction that eventually stops the diffusion process, leaving a region of net charge due to non-mobile carriers (Neamen 2012). This region is referred to as the *depletion region*.

The p-n junction is the basis of devices called semiconductor diodes. Electron-hole pairs created by the passage of radiation within the depletion zone can be collected if an external potential is applied to the junction, and their motion will give rise to a proportional electronic signal. The inherent property of an unbiased junction in thermal equilibrium is that it can function as a detector, but with limited performance. This is primarily because the electric field across the junction is typically insufficient to effectively collect the induced charge carriers (electrons and holes) that result from external excitation or radiation (Knoll 2010). Applying an external potential enhances the detector's performance. In the forward bias mode, where the p-region has a higher potential than the n-region, a high current flows through the device. Conversely, in the reverse bias mode, where

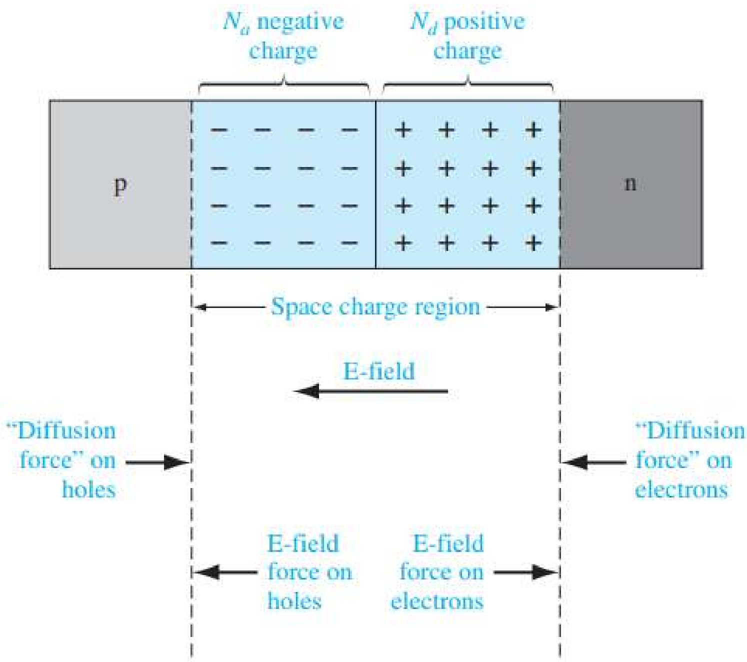

Figure 3.4: Image of a PN junction, showing the space charge region, the electric field, and the forces acting on the charged carriers. Images taken from (Neamen 2012).

the potential in the n-region is larger than the p-region, the current becomes extremely small. Reverse biasing expands the depletion region, allowing for a larger volume to collect charge carriers produced by radiation, thus improving detection performance. In forward bias, current flows relatively freely in one direction, while in reverse bias, there is a large resistance to current flow in the opposite direction.

3.2.2 SDD

Silicon Drift Detectors (SDD) are radiation detectors, introduced in 1984 by Gatti & Rehak (1984) whose working principle is based on the sideward depletion of a semiconductor (Castoldi & Guazzoni 2012).

An SDD consists of a large n-type silicon wafer of high resistivity on which a striped pattern of p^+ junctions are present (i.e. p-doped semiconductor with a higher dopant content than the p-type), covering at least one or both surfaces of the structure. The n^+ ohmic contact, one or more, at the periphery of the chip, is positively biased with respect to the p+ contacts; Figure 3.5 reports a linear and multi-anode SDD. The electron

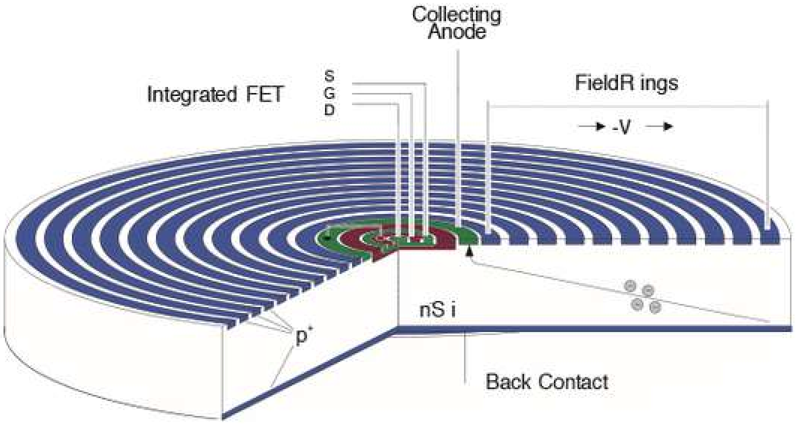

Figure 3.5: Image of the working principle of a SDD, integrated with the first transistor of the electronic circuit, a J-FET. The produced electrons are driven to the anodes for read-out. The unstructured p^+ rear contact of the device acts as the radiation entrance window (Hartmann et al. 1997).

potential energy has a funnel shape with a minimum located in the middle of the wafer. In Figure 3.6 the effect of the depletion and the final potential where the electrons will drift are reported.

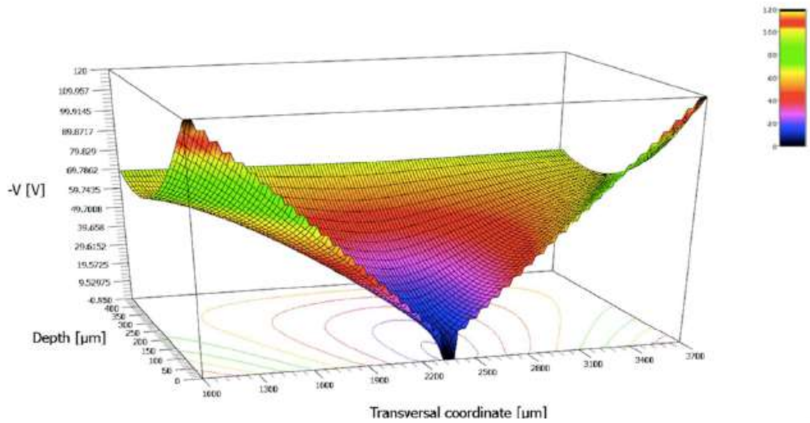

Figure 3.6: Potential distribution in the collection zone of a silicon drift detector (numerical simulation). Image courtesy of A. Vacchi[1].

Compared with a standard PIN diode of the same size, the main advantage of a SDD is the small value of the anode size (so of capacitance it present) which is practically independent of the total area of the device, limited only by the type of interconnection with the readout electronics. This feature has a prominent effect on the overall noise of the readout electronics, which is dependent on detector capacitance (Christian W. Fabjan

[1]`https://gsr.to.infn.it/wp-content/uploads/sites/8/2019/02/Vacchi_SDD-Cogne_09.pdf`

2020).

Drift detectors have therefore gained considerable attention as X-ray spectrometers, since due to their low readout noise, they show an optimal energy resolution that can be also enhanced by cooling them below room temperature. The small capacitance of drift detectors also leads to an advantage in high counting rate applications. Because the optimal shaping time for minimization of electronic noise shifts to lower values as the detector capacitance is decreased, shorter shaping times are possible that leads to a higher count rate capability for a given degree of pile-up. For example, shaping times for drift detectors can be as short as hundreds of nanoseconds (Knoll 2010).

3.3 CsI(Tl) Scintillator

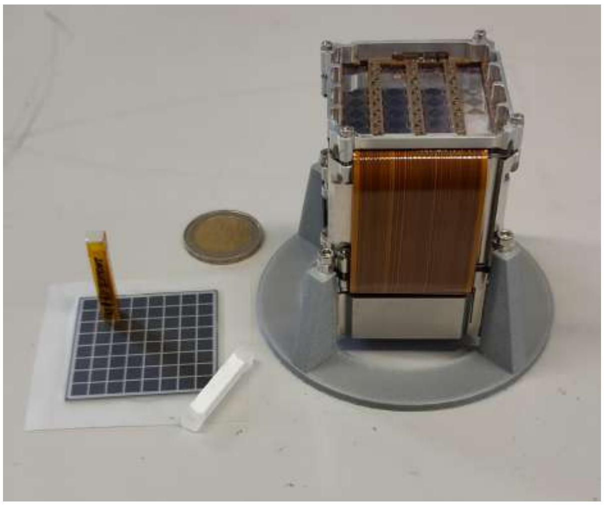

Figure 3.7: Image of a prototype module of XGIS for the Phase A of the M5 ESA call, with a SDD plane and 2 CsI(Tl) crystals, the white one partially wrapped with white coverage and the other one is completely wrapped with reflective material to drive the scintillation light at the ends of the crystal. This image was taken by us at the OAS-INAF facilities in Bologna.

The scintillation process remains one of the most useful methods available for the detection and spectroscopy of nuclear radiation, charged particles, neutrons and photons. The ideal scintillation material should: convert the kinetic energy of nuclear radiation into detectable light, the conversion should be linear (the light yield should be proportional to deposited energy over as wide a range as possible). Moreover, it should be transparent to the wavelength of its emission for good light collection, and the decay time of the induced luminescence should be short so that fast signal pulses can be generated. The material should be of good optical quality and subject to manufacturing in sizes large enough to be of interest as a practical detector. For a good scintillator, the dominant process should be the fluorescence (the rapid emission of visible radiation from a substance following its excitation). The general contributions of phosphorescence, corresponding to the emission of light of usually a longer wavelength than fluorescence, with a slower characteristic time, must be minimized.

Scintillator materials can be divided into two macro classes: organic and inorganic, with a different scintillation mechanism, that depends on the structure of the crystal lattice. Inorganic scintillators, like CsI(Tl) and NaI(Tl), are characterized by high light output, linearity, and energy resolution, but they have longer response times. In these scintillators, energy levels can be treated with band theory in the same way as semiconductors. To enhance the probability of visible photon emission during the de-excitation process, small amounts of impurities are added to inorganic scintillators. Such deliberately added impurities, called activators, create special sites in the lattice at which the normal energy band structure is modified from that of the pure crystal. New energy states are thus allowed within what would be the forbidden band in pure crystals. This reduces the energy required to excite the electron, from the valence band to conduction, because the energy is less than that of the full forbidden gap, and thus the de-excitation energy will also be lower, because the electron can de-excite through these levels to return to the valence band, making the scintillation photon visible. These de-excitation sites are called luminescence centres or recombination centres. Their energy structure in the host crystalline lattice determines the emission spectrum of the scintillator (Knoll 2010).

One important consequence of luminescence through an activator is the fact that the crystal can be transparent to the scintillation light. In the pure crystal, roughly the same energy would be required to excite an electron-hole pair as that liberated when that pair recombines. As a result, the emission and absorption spectrum therefore will overlap and there will be substantial self-absorption. However, the emission from an activated crystal occurs at an activator site where the energy transition is less than that represented by the creation of the electron-hole pair. The emission spectrum is shifted to longer wavelengths and will not be influenced by the optical absorption band of the bulk of the crystal (Knoll 2010).

An example of the different shape and purity of scintillator crystals is shown in Figure 3.8.

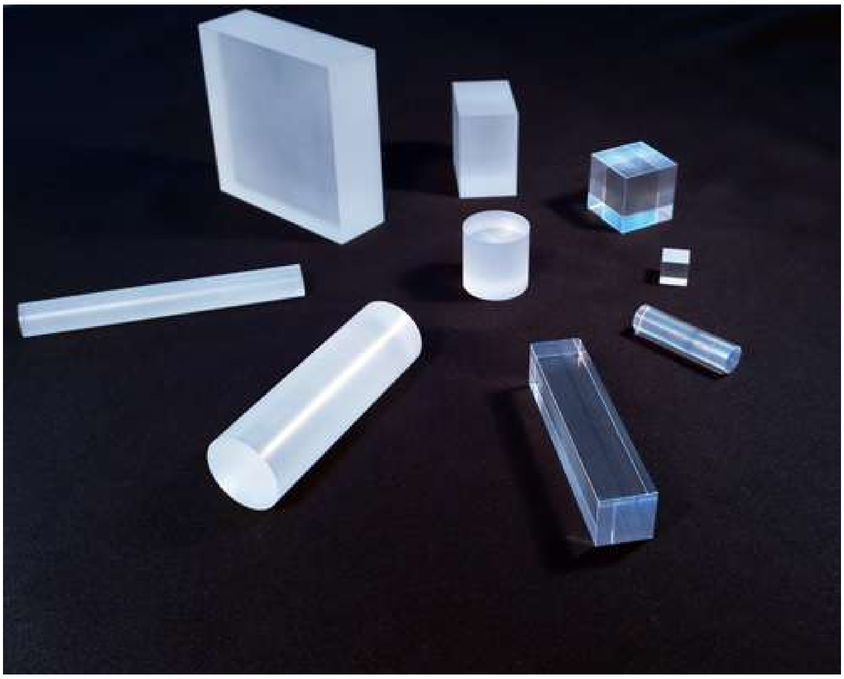

Figure 3.8: CsI(Tl) scintillator crystals with different shapes and dimensions. Image taken from Hangzhou Shalom Electro-optics Technology Co., Ltd [2].

In organic scintillators, the process that leads to the emission of visible light is different. The particle passing through the material interacts with the electronic and vibrational levels of a single scintillator molecule, and not with the energy bands relative to the entire crystal: the fluorescence mechanism arises from transitions in the energy levels, from a fundamental state to an excited, one of a single molecule and therefore the fluorescence can be observed independently of the physical state. This is why they can be present in different states of matter without changing their properties: they can take crystalline, liquid, and plastic forms. They have faster response times, but lower light yields (i.e., the ratio of the number of scintillation photons to the energy deposited). Inorganic crystals have a high Z-value of constituents and high density that favour their selection for γ-ray spectroscopy, while organic ones are often preferred for charge particle detection. In a scintillator assembly, the goal is to collect the maximum amount of emitted light from the crystal, which is why two effects must be taken into account: optical self-absorption

[2]`https://www.shalomeo.com/Scintillators/Scintillation-Crystal-Materials/CsI-Tl%20/product-393.html`

within the scintillator and losses at the scintillator surfaces. The probability of light being reabsorbed by the crystal is proportional to its size, so usually, it is not significant except for very large crystals, whereas, to minimize photon leakage from the surface, they are wrapped in a typically white layer of material that diffuses the light or that reflects it and still pushes it towards the photodetector. Another important parameter is the light output or effective light yield, which is the effective charge signal produced by the photosensor reading the scintillator light, expressed in electrons/keV of the incident radiation. This is usually a fraction of the intrinsic light output since not all scintillation photons produced within a crystal are converted into a charge unit at the output of the photodetector. Several factors come into play for this parameter: the number of scintillation photons, the efficiency in collecting these photons at the scintillator output window, the efficiency in the optical coupling between the scintillator and photodetector, the quantum efficiency of the detector, the signal integration time, and so on.

For the detection of γ-rays, XGIS uses a CsI(Tl) crystal. Caesium iodide is an alkali halide scintillation material. Particularly clean separations can be achieved between charged particles such as protons or alpha particles on the one hand and electron events on the other hand.

The luminescent states in Csl(Tl) are populated through an exponential process that results in an unusually long rise time of 20 ns for the initial appearance of the light. The subsequent decay of these states is among the slowest for the commonly used scintillation materials (Knoll 2010). The light emission for gamma-ray excitation shows two primary components with decay times and relative intensities at room temperature of 0.68 µs (64%) and 3.34 µs (36%). The best energy resolution is promoted by choosing long shaping times[1] (e.g., 12 µs) to fully integrate all the prompt scintillation lights (Böck et al. 1975) (Mahant et al. 1998).

In the XGIS configuration, each CsI(Tl) bar has dimensions $4.5 \times 4.5 \times 30$ mm^3, the longer dimension along the XGIS Camera axis (Labanti et al. 2021b).

[1]The time value that corresponds to 61 % of the peak amplitude is called shaping time (Ermis & Celiktas 2013)

3.4 Siswich Working Principle

The working principle of the XGIS detector is shown in Figure 3.9. This concept consists of a scintillator crystal bar, made of CsI(Tl), coupled at both ends with a single-cell SDD.
The silicon photo-detector used to collect the scintillation light is also a direct X-ray detector, for radiation interacting in the Si depletion zone; in the XGIS case the thickness of the SDD depletion zone is 0.45 mm so that this device has a significant efficiency for X ray up to about 30 KeV. Additionally, when X-rays interact with silicon, the creation of electron-hole pairs results in a fast signal with a rise time of about 10 ns. On the other hand, the collection of scintillation light is primarily governed by the de-excitation time of fluorescence states, which can take a few microseconds. Therefore, in this scenario, a shaping time is necessary to mitigate any significant ballistic deficit (Marisaldi et al. 2004).

3.4.1 The XGIS siswich architecture

The SDDs, Application Specific Integrated Circuit (ASIC) and detector assembly are the key technologies for XGIS. The SDD has been used in many experiments on the ground, and proposed for space missions; such as the Large Observatory for X-ray Timing (LOFT) ESA M3 candidate mission, or the NICER (Neutron Star Interior Composition Explorer Mission) mission, or the eXTP (X-ray Timing and Polarimetry) mission; as well for the nano-satellite constellation HERMES.
The SDD design employed in XGIS results from the developments carried out in the framework of the ReDSoX collaboration, led by INFN (Istituto Nazionale di Fisica Nucleare) with the participation of several institutions (FBK "Fondazione Bruno Kessler", INAF "Istituto nazionale di Astrofisica", University of Pavia, Polytechnic of Milan, ENEA, Elettra Syncrotron, etc.).
The single XGIS base module is arranged to have two (8×8) silicon drift detector (SDD) matrices optically coupled at the opposite sides of a block of 64 CsI(Tl) scintillator crystals, and is housed in a metal frame (see Figure 3.2). The detectors are made using a full double-side process: the p-side is the side in which the optical entrance window is made, while the n-side is the side in which the collecting anode electrode is made by an

ohmic bulk contact, surrounded by the drift rings. The n-side of the detector will be directly exposed to radiation. The sensitive area for X-rays detection, which in principle is the geometrical area 5×5 mm^2 of each array element, is instead reduced due to a partial obstruction made by the assembly Printed Circuit Board (PCB). The p-side of the detector will be optically coupled to the scintillators. To guarantee an adequate optical separation among adjacent elements, a 0.5 mm wide Al track is deposited between the SDD elements, thus reducing the sensitive area for the scintillation light to 4.5×4.5 mm^2. The scintillation light of the crystal will be collected also by a second SDD array placed on the bottom side of the module. Figure 3.9 shows the pixel operation concept. Two SDDs are placed at the two opposite sides of a scintillator CsI(Tl) crystal. The depletion voltage of each SDD is strongly linked to the doping concentration of the substrates and then, for a large area detector, the doping uniformity at the wafer level is crucial. For devices manufactured in the same production run with the same substrate batch depletion voltage uniformity level have to fit the requirements for the production of the XGIS sensor for THESEUS, reported in Table 3.1.

Array size	42.4 × 42.4 mm^2
Si thickness	450 μm
Number of SDDs	64
SDD pitch (n side)	5 x 5 mm^2
Single SDD active area for scintillator (p side)	4.5 × 4.5 mm^2
Metal grid between single SDD (p side)	0.5 mm wide
Typical polarization voltage (one connection/SDD)	–150 to –200 V
Single SDD capacitance	50 fF (typical)
Single SDD dark current (at T= 20 °C)	350 – 1000 nm (typical)
Quantum efficiency (at 560 nm)	> 80 %
Optical spectral response	350 – 1000 nm (typical)

Table 3.1: Table of the main parameters of the SDD array (Labanti et al. 2021a).

Applying the siswich concept illustrated above, low-energy X-rays (from 1-2 keV to 25-30 keV) are directly absorbed by the SDD, leading to a very sharp (∼100–200 ns) rise-time analog signal on the detector preamplifier. Higher energy X-rays and γ-rays are instead absorbed in the CsI(Tl), thus producing a large number of optical scintillation photons.

These photons are collected and detected by the SDDs, giving rise to a much slower ($\sim$ few μs, dominated by the scintillator crystal fluorescent states de-excitation times) output signal. As a consequence, the signals from the SDD and the scintillator should be integrated at different times to maintain the lowest noise and avoid significant ballistic deficit (see Section 3.3).
An X photon produces signal only in the top SDD, γ-ray with the scintillation produces coincident signals in time in the top and bottom SDD. This allows to discriminate between the two types of events, rendering the detector sensitive to a very large energy band. An opportune readout electronics integrated into an ASIC, called ORION, is able to discriminate the two signals.

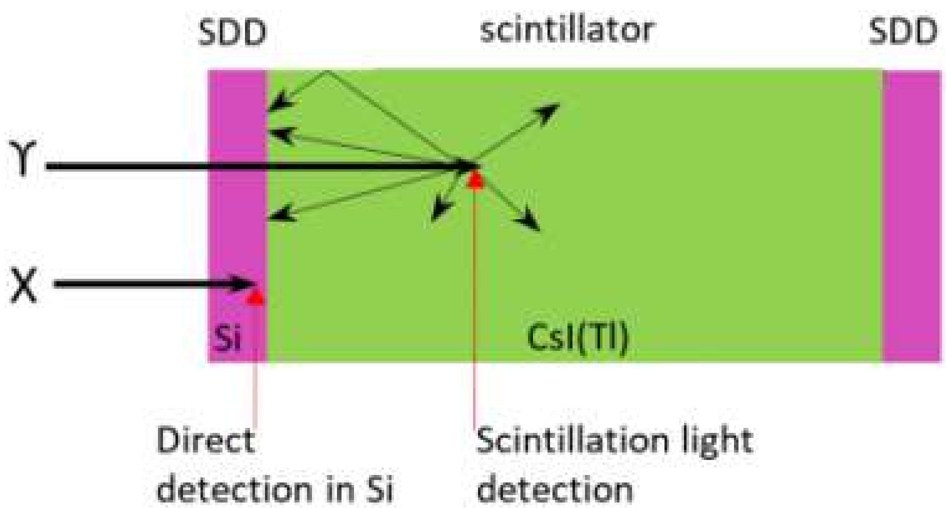

Figure 3.9: Image of a single XGIS pixel operation principle. Image taken from Labanti et al. (2021a).

Each SDD at the top and bottom of the crystals will be read out by custom ASICs, the ORION-FE (with FE meaning Front-END), placed near the SDD anode, with the functions of pre-amplifying and buffering the signal. All the other functions needed to properly process the signal will be accomplished in a second ASIC, the Orion-BE (with BE meaning Back-End), placed in the bottom part of the module below the scintillator crystals. The separation of electronic functions and the need to stay close to the anode are necessary to keep the dimension of the pre-amp ASIC as small as possible, maximizing the low-energy radiation entering the SDD, and not to increase stray capacitance.

The pixel size of the SDD determines the position resolution in the detector plane for both direct SDD and scintillation detection, see Section 3.5. By weighting the two SDD signals (top and bottom), the scintillation depth in the bar can be evaluated producing a 3-D position detector, this feature will be used in data analysis to reduce the background. Also, an image can be obtained through the coded-mask imaging method.

3.5 ORION Chipset

The 2 XGIS cameras will contain 200 modules, each one with 64 pixels, for a total of 12.800 individual detectors. Each one will require 2 SDDs with related electronic readouts. Furthermore, the readout should treat signals introducing the lowest possible noise level, maintain and elaborate the information from two different kinds of interactions in Si and in the scintillator (siswich principle), and operate with low power and in a harsh space environment. Therefore a full custom, multichip, readout electronics is crucial for the XGIS experiment. In this scenario the two ASICs of the ORION chipset (ORION-FE and ORION-BE) were developed, thanks to a strong heritage from the ReDSoX research program.

The ASIC requirements specification, provided by the OAS THESEUS team, were first deeply discussed and then realised by engineering team from Polytechnic of Milan and University of Pavia, which has a deep expertise in this field, having acquired know-how over the last 20 years, successfully developing several mixed-signal ASICs, specific for X- and γ-ray detectors. In the frame of THESEUS M5 proposal, the ASIC was considered a "critical technology" by ESA reviewers; a development program, aimed to arrive to the final ORION chipset design was then discussed, approved and realised. ORION ASICs of increasing complexity were realised in four steps, using the MOS (Metal Oxide Silicon) technology 0.35um C35B4C3 technology of the AMS foundry (i.e. Si chips with minimum 0.35 microns wide tracks) available to Universities and Research institution through the Europractice consortium [2] that since 30 years allows micro-electronic development in Europe.

The ORION chipset is responsible for both the analog readout of the SDD charge, applying the operations of a spectroscopic nuclear electronic chain, and for the digitization

[2] https://europractice-ic.com/

and data communication of the event information to the module back-end electronics.
The ORION readout electronics integrates two dedicated analog processors for low-energy photons up to 80 keV (X-branch) and high-energy photons up to 10 MeV (γ-branch), allowing a spectroscopy-grade resolution in the 4 decades energy band (2 keV–10 MeV) of the XGIS.
As shown in the Figure 3.9, direct X-ray detection occurs in the Si of the top SDD of a pixel, which implies the following points:

- *Readout Strategy*: an X-ray under 30 keV ist detected with good effiency within a single SDD cell, thus the readout electronics must read and process the charge of a single cell;
- *Noise Performance*: for the purpose of making the most of the high-energy resolution of SDDs, the minimized stray capacitance at of ASIC-SDD connection must be minimised, so the first element of the ORION chipset (a pre-amplifier) must be as close as possible to the SDD anode; a minimum noise design strategy of the electronics compatible with a low power consumption is required;
- *Processing Time*: to optimise the Signal/Noise ratio of the "transfer function" applied to the signal, and considering the fast signal rise time of the Si detector (hundreds of nanoseconds) a signal integration time of about one microsecond is chosen.

As γ-ray detection occurs in the scintillator, the requirements for the ORION chipset regarding the gamma-ray branch are:

- *Readout Strategy*: the scintillation light will produce a time-coincident signal on two distant SDD pixels at the extremities of the CsI(Tl) bar. The readout electronics must be able to combine the two charge signals, apply the time-coincident signal to proper discrimination and filtering strategy;
- *Noise Performance*: the light generation statistics of the CsI(Tl) bars will most likely limit the spectroscopic performance of the γ-ray events. As in the previous case the noise should be minimised, for the top SDD the same preamplifier will be used for X and γ signal readout, for the bottom SDD an ORION preamplifier chip with the same configuration of the top will be mounted near the bottom SDD anode;

- *Processing Time*: due to the characteristic constant time of the scintillation light (up to several microseconds), the signal integration time determined by the shaping electronics must ensure a peaking time long enough to avoid a ballistic deficit in the charge collection (Mele et al. 2021).

For the application of these two (X and γ) operating principles, ORION has been conceived as constituted by two ASICs, where every XGIS pixel is read and pre-amplified by two front-end ASICs (ORION-FE) and one back-end ASIC (ORION-BE), that integrates a triple-core processing chain. The FE will be of a small size so that can be mounted near the SDD's anode, while the BE can be mounted a few cm away from the detector core.

3.5.1 ORION-FE

The ORION-FE ASIC is a 490 μm $\times$ 990 μm fully-analog ASIC conceived to provide the first amplification of the charge signal coming from the SDD, keeping a low area occupation ($\sim$0.3 mm^2). Conceptually the pre-amplifier integrates, as a capacitor of very small value C (nominally 14,4 fF), the transient SDD current pulse to produce a signal voltage V proportional the charge Q produce in the Silicon. The pre-amplified output signal into a form suitable for measurements, meaning to maximize the S/N ratio. The rise time of the output pulse is kept as short as possible, consistent with the charge collection time in the detector itself. The signals are transmitted from the ORION-FE to the ORION-BE in current mode.
The full-scale range of the CSA (Charge Sensitive Amplifier) is set to 90 000 e$^-$, which allows the ORION-FE to correctly process both X and γ events (the event type can only be discriminated on the ORION-BE, where information on both top and bottom SDDs is collected) (Mele et al. 2021).
An image of the bonding of the SDD to the FE is shown in Figure 3.10, and in Figure 3.11 a schematic representation of the components of the FE and the disposition of the FE with a XGIS pixel. The topology of Orion-FE with 2 pre-amplifiers per chip is designed to fit the PCB design at the top of the module with each pre-amplifier facing the corresponding SDD.

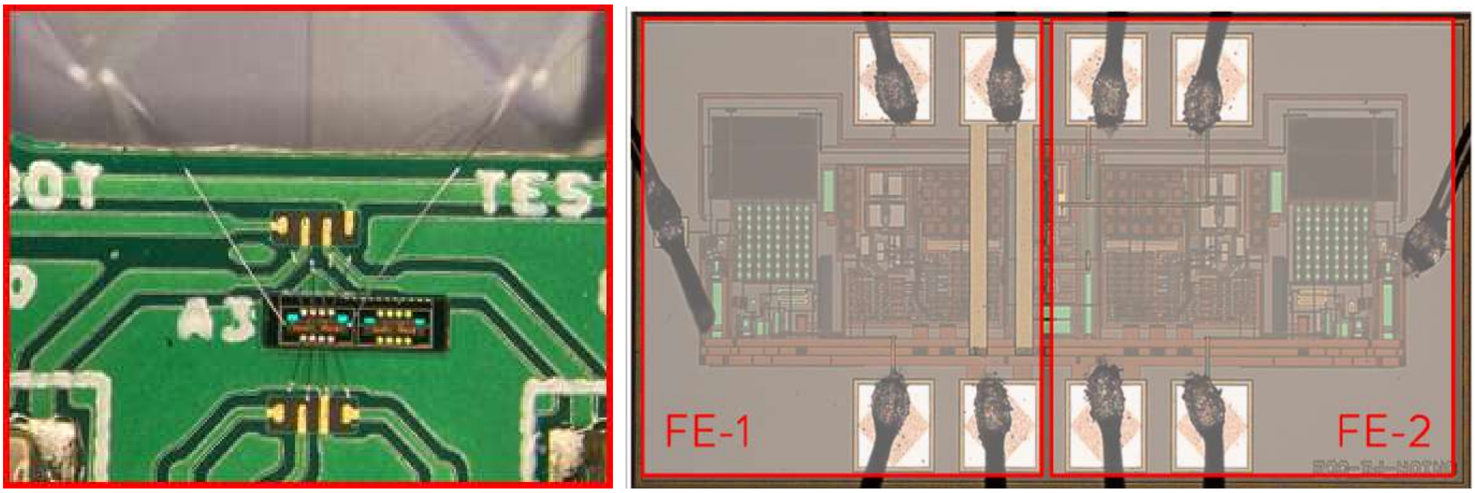

Figure 3.10: Left: image of the ORION-FE bondings. Image taken from Mele et al. (2021). Right: image of the ORION-FE (dual channel) micrograph with the connections of the bondings. The small dimension of the input pads (right and left on the picture) is optimised to minimise the input capacitance, compared to the other service pads dimension. This design of ORION-FE is the one that satisfies the requirements specifications. Image courtesy of F. Mele (PoliMi).

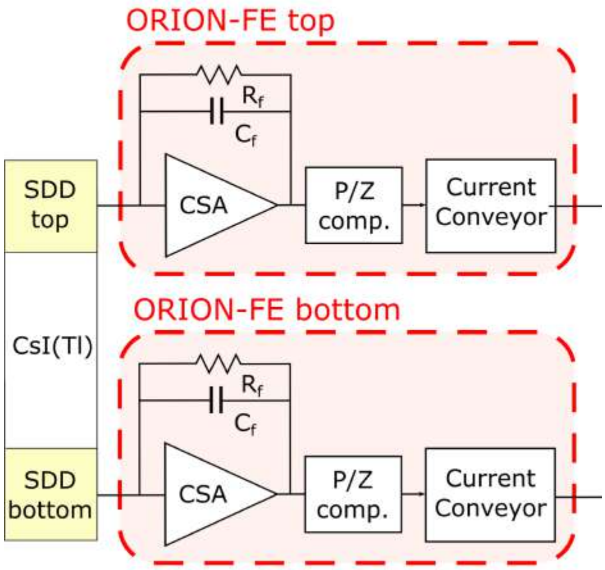

Figure 3.11: Block-diagram of two ORION-FEs readout electronics for a single XGIS pixel. CSA is a charge sensitive pre-amplifier P/Z comp. is a Pole zero compensation circuit defining the shape of the transmitted signal. Diagram taken from Mele et al. (2021).

3.5.2 ORION-BE

The ORION-BE chipset is located on a Printed Circuit Board (PCB) on the bottom of the module, Figure 3.12, a few centimetres away from the ORION FE.

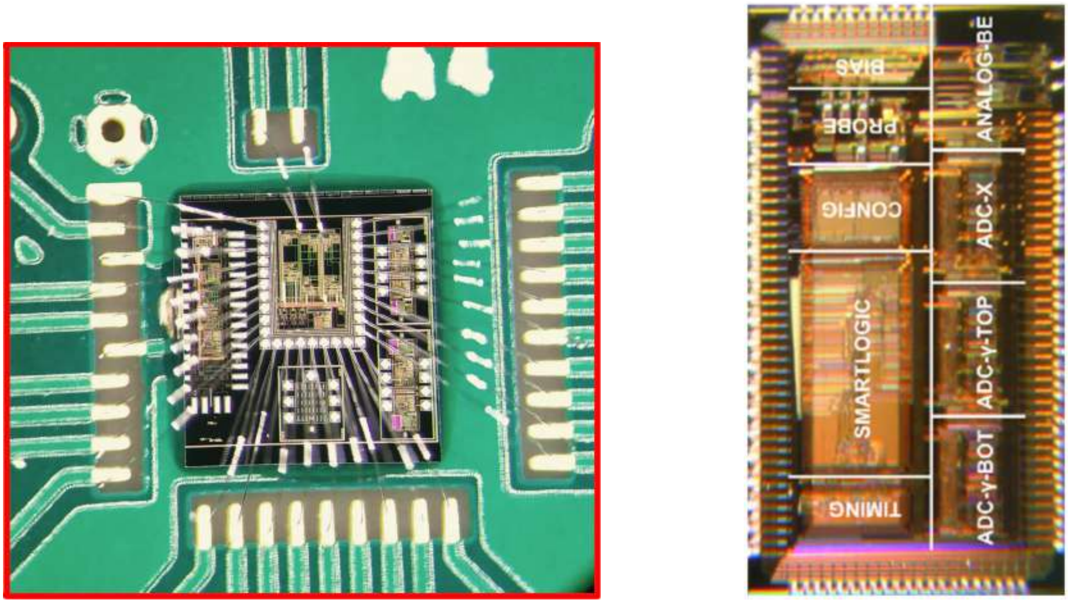

Figure 3.12: Left: Picture of the ORION-BE micrograph with the connections of the bondings. Image given by the courtesy of F. Mele (PoliMi). Right: Picture of the ORION-BE channel chip micrograph. This is the first prototype of the ORION-BE collecting the signal of just 2 ORION-FE (one pixel) and with many test points connected to the many pads so to allow to reach and test individual parts of the circuit. Image taken from Grassi et al. (2022).

The ORION-BE is a mixed signal ASIC. Signals coming from the top and bottom SDDs of the same XGIS pixel, after being processed by two ORION-FE chips, are collected by two dedicated current receivers in each ORION-BE processor. The BE processor contains the RC stage of the semi-Gaussian-shaper, matched to have the same time constant of the first CR shaping realized in the FE, which elaborates the shaped pulse. Internally, the ORION-BE implements two processors (X and γ) with three signal processing channels two for the top SDD signal one for the bottom SDD, allowing an optimized noise performance, selecting the most favourable peaking time and conversion gain for each type of event.

As can be seen in Figure 3.13 ORION-BE includes the following different circuit blocks:

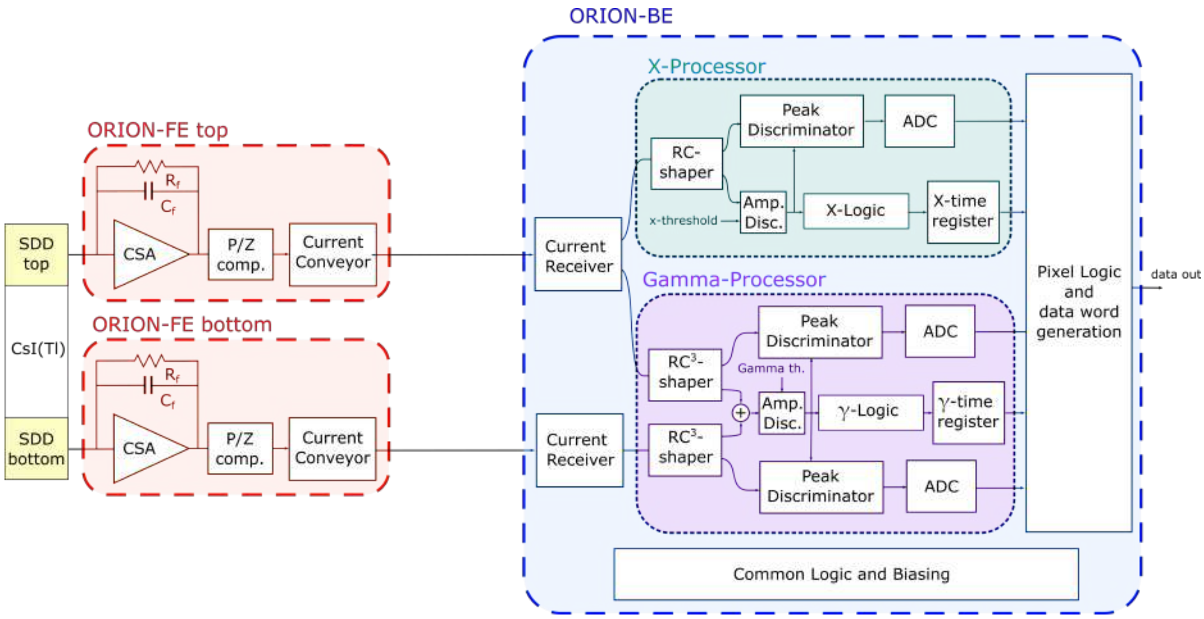

Figure 3.13: Block-diagram of a single ORION readout electronics, for the readout of a single XGIS pixel. It is composed by two ORION-FE (top and bottom) and one ORION-BE with separate X and γ processing channels. Diagram taken from Mele et al. (2021).

shaping of the signal, discrimination above the noise and stretching of the signal, digital conversion of signal amplitude, time marking of the signal occurrence, the logic for digital data composition and transmission, handshaking with external circuitry. ORION-BE deals with the signals as described in detail below.

3.5.2.1 Signal Shaping

The very small value of charge detected produced in the SDD and collected into a current pulse by the ORION-FE, is preamplified, converted in voltage, buffered and sent to ORION-BE where it needs to be converted back, and amplified to be further elaborated. The shaper amplifiers in ORION-BE, X and γ branches, have the task to realise the optimum filter, in the signal/noise balance, and minimize the pile-up for the signal they elaborate. The amplifier is characterized by a constant shaping time that is related to the duration of the pulse produced at its output. An X-ray will deliver a short signal and a scintillator a longer. Short shaping time are desirable to reduce the noise due to integration of the SDD leakage current.

The shaping of the signal is achieved by combining circuits that while amplifying also

analogically derivate (CR) and integrate (RC) with proper time constants. As it is not known if a signal will result in an X (Si interaction) or a γ event (scintillation interaction), the Top-SDD signal of a pixel is processed both in the X and the γ branches of the ASIC while the bottom SDD signal of a pixel is processed only in the γ branch. Furthermore, the amplification level of the X or γ branches is done to fulfil the energy range of the two detection modes (80 keV i.e. about max 21.000 e^- for X, and 10 MeV i.e. about max 90.000 e^- for γ). The fast rise time of an X (1 μs) signal needs only a CR-RC shaping. For the γ shaping, instead a CR-RC^3 is used, and results in a peaking time that is a factor of 4 longer than that for a simple CR-RC network, more suited for a γ-ray that has to collect the scintillation light (3 μs).
In Figure 3.14 we show a a pulse simulated input step signal is shaped in the X-top and gamma top and bottom chains.

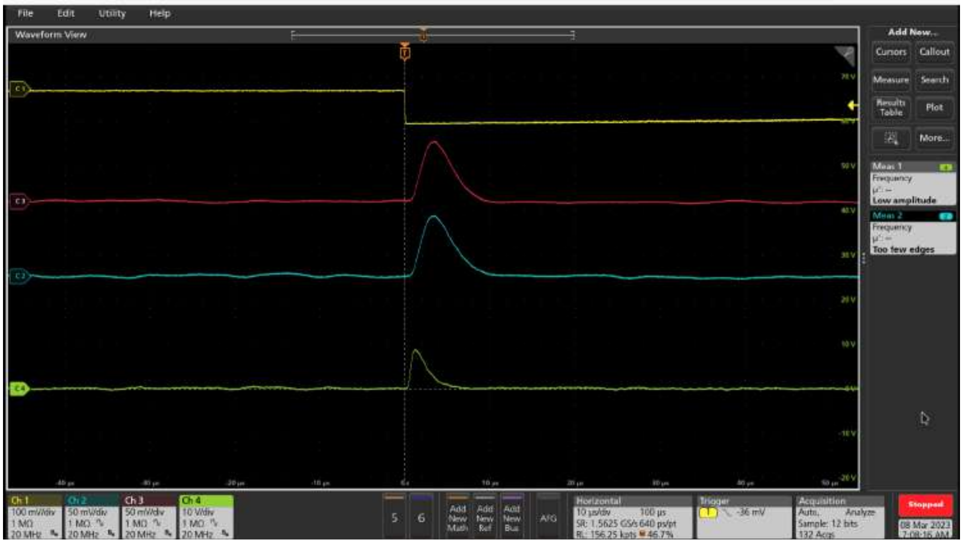

Figure 3.14: Image of three shaped signals from an impulse. The first signal from the top is the impulse, the red and blue ones are the signals from the γ-shaped chains and the green one is the signal from the X-shaped chain. The plot shows the difference in shaping time between X and γ.

The ORION-FE pre-amplifier is linearly proportional to the input charge in a determinate energy range, if the amplitude exceeds the maximum design output amplitude, the amplifier will saturate or limit and produce a distorted output pulse with a flat top at the amplitude at which saturation occurs, as shown in Figure 3.15 (Knoll 2010). However, the operative range the ASIC can shape normally the signal incoming from the SDD, as shown in Figure 3.16.

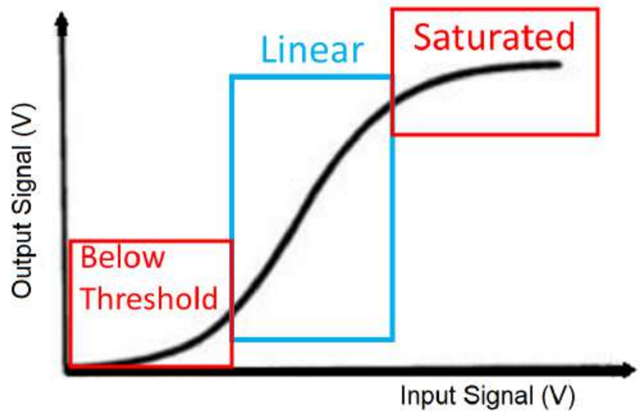

Figure 3.15: The light blue rectangle indicates the range in which the voltage output from the amplifier is a linear function of the input voltage. The red squares indicate the regions where output and input are not linear. On the left, the signal is below the detection threshold and is not elaborated by the amplifier, on the right the signal is saturated instead.

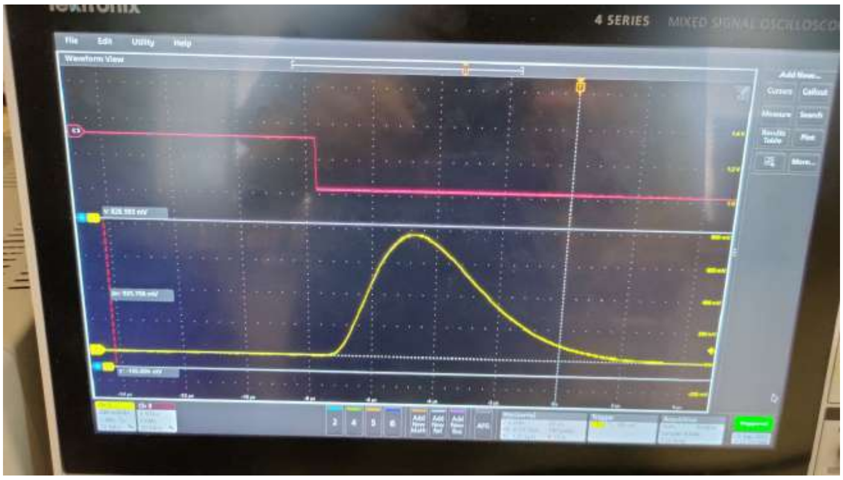

Figure 3.16: Image taken from the oscilloscope. The red signal is the input impulse from the pulser, while the yellow signal is the correct shaped signal from the γ branch.

On the other hand, below the lower limit of the operative range, the ASIC can not shape the impulse. Conversely, at higher amplitudes, the peak of the shaped signal flattens, meaning the ASIC is working in a saturated regime, where the output is no longer proportional to the input (Gilmore 2008).

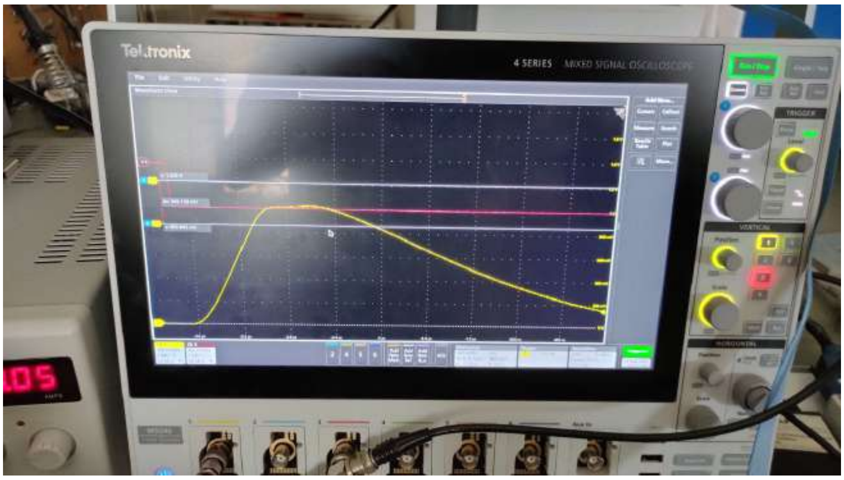

Figure 3.17: Image taken from the oscilloscope. The red signal is the input impulse from the pulser. The yellow signal is the output from the γ branch in shaping mode, which is saturated. The signal thus diverges from a Gaussian profile and is instead flattened at the peak.

3.5.2.2 Signal Discrimination and Peak Stretching

After the shaping of the signal, it is important to record the maximum value of the shaped peak. The information about the energy of a detected event, X or gamma, is related to the peak amptlitude of the shaped signal. This is done by the peak discriminator, which has the task to hold the signal peak received from the current receiver, and differentiate between an X or a γ ray. To properly acquire and convert into digital units a given signal, the ASIC needs to hold the peak for a time period sufficiently long for the acquisition to take place and converting these amplitudes to a digital number (Analog to Digital Conversion, ADC). In both X and γ branches a discriminator circuit has the task to detect if the signal is above the noise level and trigger the acquisition chain. In the X branch the discriminator senses if the signal amplitude of the SDD top is above a threshold level defined when configuring an opportune ASIC register and activates a circuit that stretches the top SDD X-shaped signal when it reaches his peak value stretch (or 'held'), so that the pulse maximum is available for comparison over the time needed for the conversion into digital units (Knoll 2010). As shown in Figure 3.13, in the γ-branch the discrimination, due to the nature of SDD top and bottom coincident signals, is made comparing the sum of the two slow shaped signals with a refrence voltage value. The X and gamma discrimination can be verified with the ASIC output by monitoring the Trigger X and Trigger γ logical output signals, the Trigger (X or γ) signal occurs always at peak of the signal. Figure 3.18 shows how the stretched and the trigger signals are related. The last LAM (look at me) signal indicates the end of ADC conversion (Grassi et al. 2022). The digital signal, Trigger or LAM are used by the external electronics to command the operations for extracting the information from the ASIC and reset it for further operation.

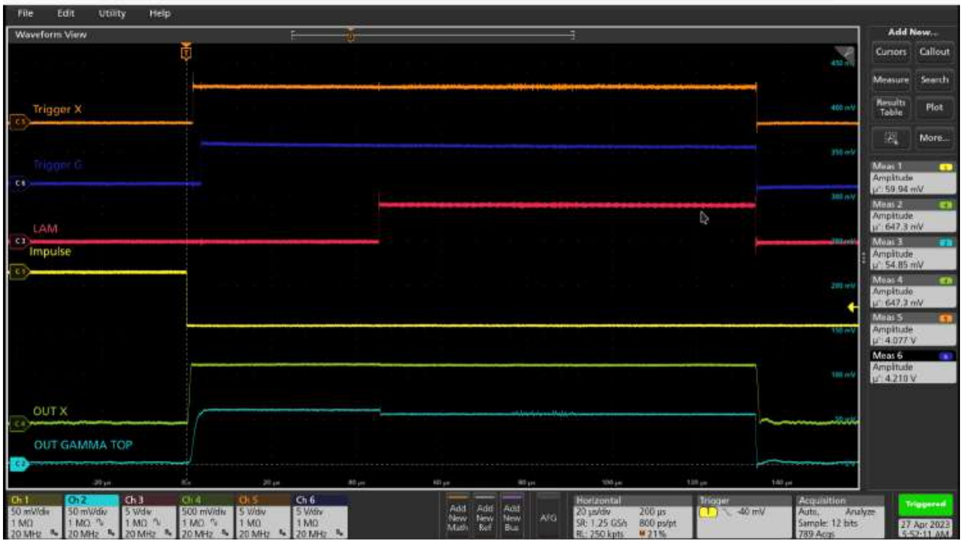

Figure 3.18: Image of the oscilloscope with two stretched signal from an impulse, triggers and Look at Me signal. The green signal is the stretched X signal chain. We also show the blue signal is the stretched γ signal chain the trigger X (red), trigger γ (blue), and the LaM (red) signals. The figure shows how the Trigger X and Trigger γ are emitted at the peak of the shaped signal, and are then delayed due to the different shaping time.

For testing purposes, the actual ORION-BE can work either in shaping mode or in stretch mode. In shaping mode, the pulse discriminator (the peak detector and the trigger logic are disabled), and the output signals of the X and γ shapers are directly routed to the output probe circuits. In stretch mode, the pulse discriminator, the peak detector and trigger logic are enabled, and the internal stretched output signals (the ADC input signal) are also routed to the probes (Mele et al. 2021).

3.5.2.3 Analog to Digital Conversion (ADC)

The stretched signals described in the previous paragraph are converted to a digital value with ADC circuits. Three independent ADCs are used as shown in Figure 3.13.

To operate the ADC we need an external clock signal that can be work at frequency up to 7 MHz. The Trigger (X or γ) commands the ADC to start the conversion, after the Rise Time Protection (RTP), a few programmable microsends, to settle the circutery. At the end of the data conversion the ASIC sends a LAM signal to the external logic (Grassi et al. 2022).

3.5.2.4 Time Marking of the event

Another piece of information characterising the event is its occurrence time, that it is required with 1 microsecond precision. This data is evaluated starting from an external supplied Pulse Per Second (Marchesini et al. 2021). The PPS resets an ASIC internal counter that is incremented with the same Clock used for the ADCs. At Trigger (X and γ) occurrence the counter is read and his content correlated with the PPS gives the time mark of the event. The analog-to-digital conversion ends and the triggered signal is reset, allowing the processing of a new signal; the test equipment sends a RESTART signal to the ASIC, which also resets the analog section. The acquisition chain is shown in Figure 3.19.

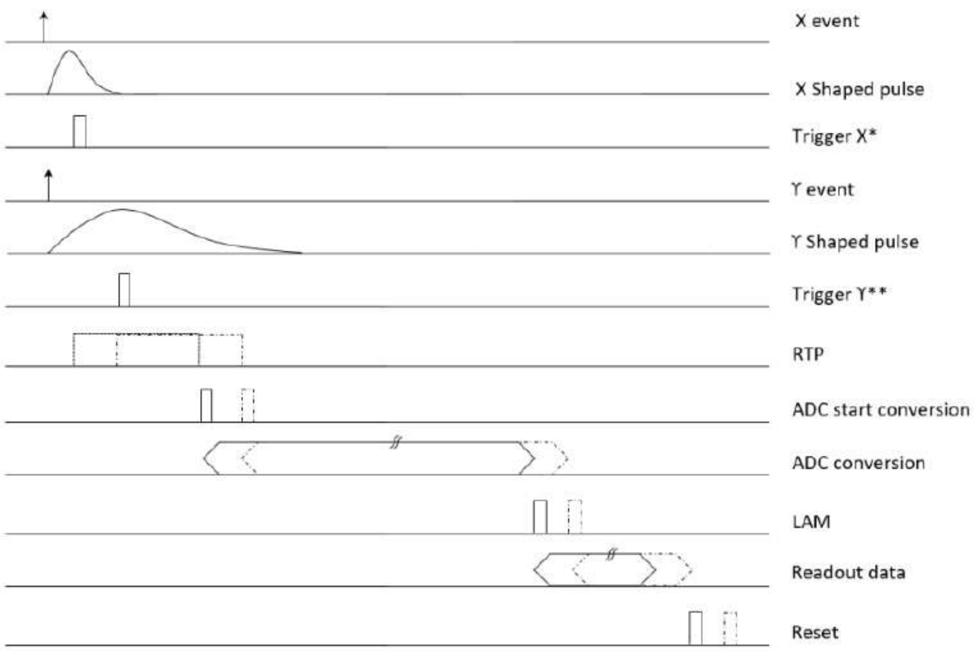

Figure 3.19: Diagram of the acquisition chain from the ORION-BE. Image curtesy of Labanti.

3.5.2.5 ORION Event Discrimination Logic

ORION-BE has a discrimination logic to distinguish between an X event and a γ event. We will discuss the two cases separately:

- *X-ray*: an X-ray photon arrives on the SDD. The X-processor of the BE has been designed to elaborate signals from the top SDD detecting photons up to 30 keV, corresponding to an input charge range of about 10000 electrons. Since the X-photons will be absorbed by direct conversion on the top SDD, a fast signal rises, of the order of a few tens of nanoseconds. For this reason, the shaping time of the X-processor is set to 1 μs (Mele et al. 2021). The BE then follows the acquisition chain described in Section 3.5.2.4. Now the last part of the logic refines the digital discrimination process; in this case, only an X trigger is stored, and then the event will be considered X. A diagram of the physics process and the acquisition chain is shown in Figure 3.20.

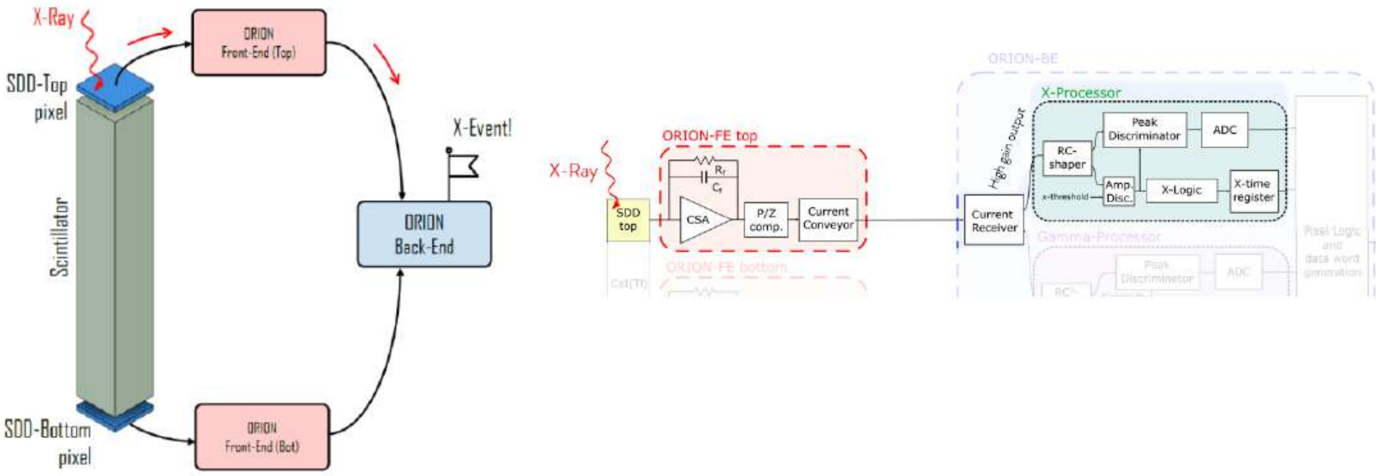

Figure 3.20: Left: Diagram of a single XGIS pixel hit by a X-ray photon and the classification as X event. Right: Block-diagram of the X branch of a single ORION readout electronics, for the readout of the XGIS pixel. Image courtesy of F. Mele (PoliMi).

- γ*-ray*: A γ-ray photon goes through the SDD. The crystal stops the high-energy photon and produces scintillation light. This optical light is reflected by the crystal wrapping, until is absorbed by both the SDD Top and the SDD Bottom. The XGIS instrument is expected to detect γ photons up to 10 MeV, but the probability of having the complete 10 MeV photon stopped in a single CsI(Tl) crystal is extremely low, allowing to set the expected maximum energy range of a single XGIS pixel to approximately 7.2 MeV (Mele et al. 2021). Two current signals arrive simultaneously at the BE from the FEs. The output of the top current receiver is elaborated by the γ-top channel of the γ-processor, and the output of the bottom current receiver in the γ-bottom processor.

In this case, the γ shaper has a peaking time of 3 μs. The outputs on the top and bottom shapers are summed in current mode to eventually trigger the amplitude discriminator and start the digital processing by the γ logic. Two independent peak detectors and analog-to-digital converters (ADCs) are then used to digitize the outputs of the γ shapers, which are eventually summed in the digital domain. The BE then follows the acquisition chain described in Section 3.5.2.4. Now the logic starts the refining of the digital discrimination process (Fuschino et al. 2021). The output data will include: γ register time, ADC-γ-bot and ADC-γ-top data. A diagram of the physics process and the acquisition chain is shown in Figure 3.21.

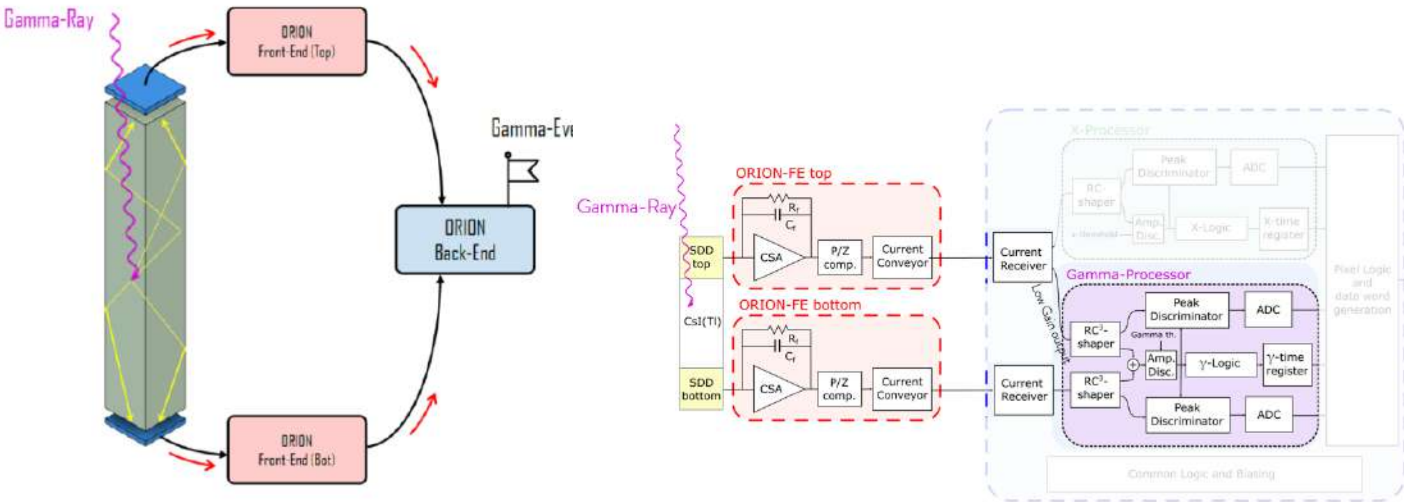

Figure 3.21: Left: Diagram of a single XGIS pixel hit by a γ-ray photon and the classification as γ event. Right: Block-diagram of the γ branch of a single ORION readout electronics, for the readout of the XGIS pixel. Image courtesy of F. Mele (PoliMi).

For the full XGIS, a total of 12800 analog ORION-FE are foreseen, which will send a pre-shaped signal to 1600 mixed-signal back-end multi-channel chips (8-channels ORION-BE) for dedicated signal processing and digitization.

3.5.2.6 Format of the output data

An event detected by a pixel and elaborated by the ORION chipset is contained in a 64 bit word as illustrated in Table 3.2.

Time	Address	X/γ	SDD Bot	SDD Top	TRG X	TRG
24 bit	3 bit	1 bit	16 bit	16 bit	1 bit	1 bit

Table 3.2: 64-bit output frame of ORION-BE-channel ASIC (Grassi et al. 2022).

Further details are reported in Table 3.3.

Event	Time	X/γ	SDD Bot	SDD Top	TRG X	TRG
X	X-Time	0	0	Data X	1	0
γ	γ-Time	1	Data γ-Bottom	Data γ-Top	1	1

Table 3.3: 64-bit output frame of ORION-BE-channel ASIC, depending on the event type (Grassi et al. 2022).

Chapter 4

Characterization of the single-channel ORION I ASIC

This Chapter discusses the tests performed on the ORION ASICs described in Section 3.5, which are one of the most critical elements for THESEUS/XGIS. In particular, in this chapter, we will explain the different tests performed to characterize the ASIC ORION I Single Channel, connected to a SDD but with no scintillator crystal.
We will present the ASIC circuit in Section 4.1, and the test setup in Section 4.2. We describe the procedure and the result of the functionality tests in Section 4.3, both in the X-branch and γ branch. We describe the procedure and the results of the performance tests in Section 4.4, both in the X-branch and γ branch. We will describe the environmental tests and results in Section 4.5.
The board BE-6, which was tested at first, did not endure the environmental test. We repeated the functionality tests with another board, BE-5. Both are prototypes of the same design.

4.1 ORION ASIC single channel circuit

A first set of ORION-FE V1.1 and ORION-BE V1.1 ASIC prototypes, were monted on test boards BE-5 and BE-6 designed at INAF/IASF Milano. Two ORION-FE were connected to two SDD available at the moment and belonging to the Hermes nanosatellite experiment. Each SDD is about 42 mm^2. The HERMES SDDs (see Appendix F) are arranged in matrix 5×2 with cells 6.05×7.44 mm, and 450μm thick. Instead, the ORION's

SDDs are organized in a matrix 8×8 with cells 5×5 mm, 450 μm thick. The ORION-BE V1.1 (from now on, called ORION I) includes the processing chain of one channel with both X and γ branch, many test point to monitor different ASIC parts. The ASIC does not include the logic for X/γ selection, and the data interface with the external so that the three ADC and the time output data are available as parallel signal (16 bit/24 bit). Figure 4.1 shows details of the board esigned by INAF/IASF (Milan) and its components.

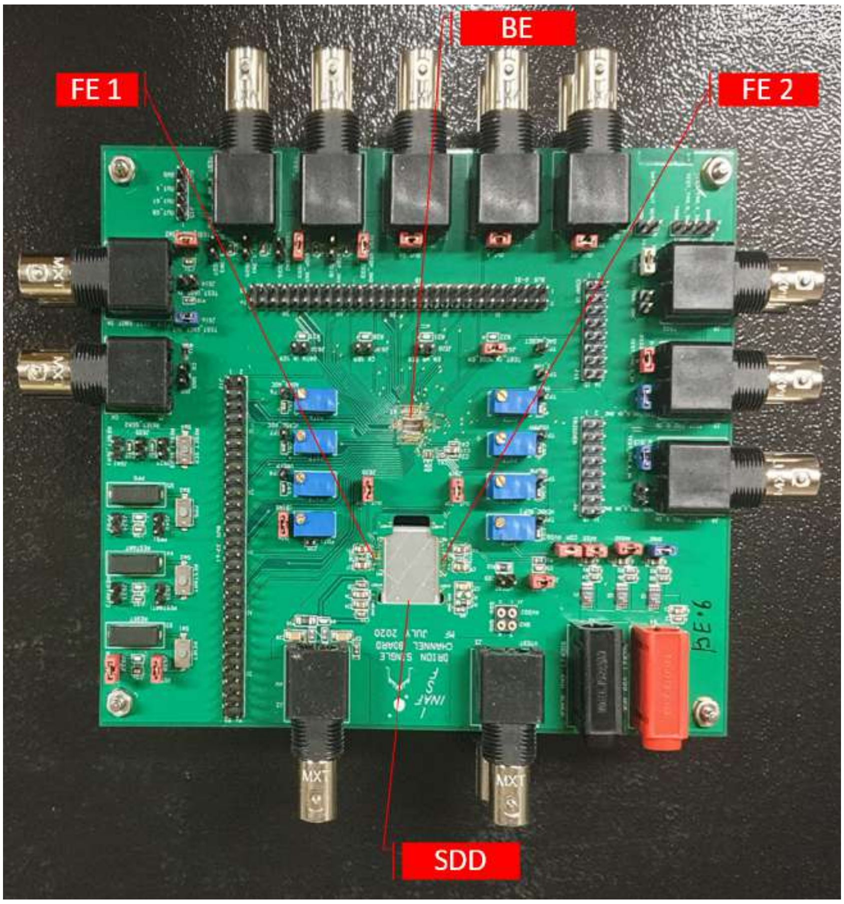

Figure 4.1: Image of the test board BE-6 with the elements of the ORION I circuit, where the position of both the FE, the BE and the SDD are marked in red.

The X and γ branches can be tested with both electrical impulses or low energy radioactive sources interacting in the SDD.

4.2 Test setup

The test setup consists of a National Instruments (NI) [1] board commanded by a program that we developed specifically for this purpose, in LabVIEW (see Appendix D), together with a NI Interface board connected to the ASIC board. A pulser is connected to the ASIC board to stimulate the ORION I FE with electrical pulses. Low and high power supplies are used to supply voltage to the FE and the BE together, and to polarise the SDDs present on the test board. An MCA8000D (Multi-Channel Analyser [2]) can also be connected to test the BE in order to compare internal ADCs data with data from an independent device when connected the analogic signal.
The main power supply, data configuration and data acquisition components of the test setup are shown in Figure 4.2.

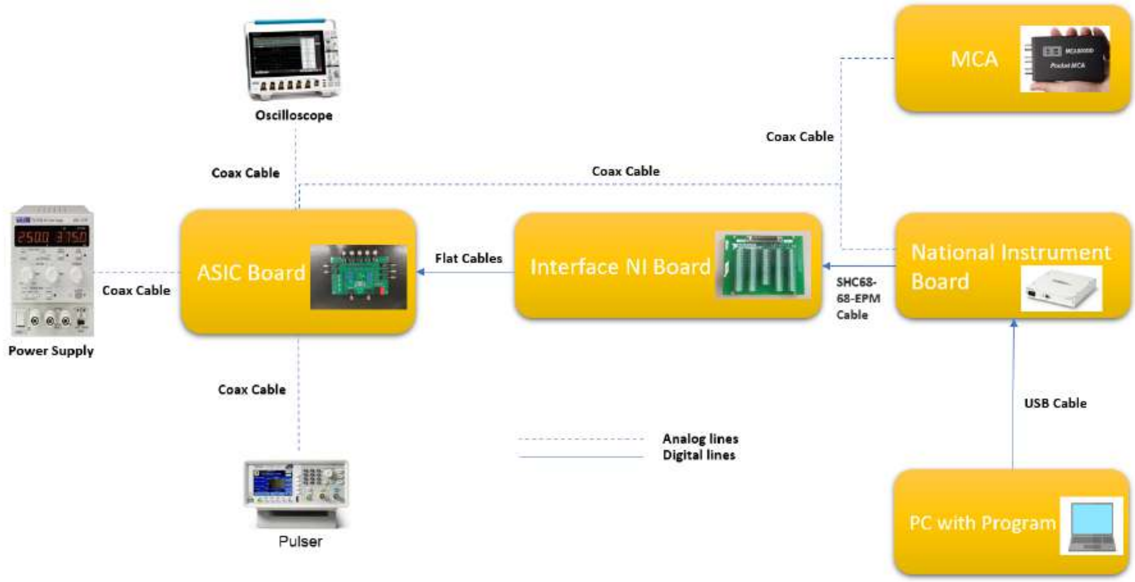

Figure 4.2: Diagram of the test seup connections. Analog connections (coaxial cables) are expressed with dotted lines. Digital connections are expressed with continue lines.

The test setup consists of:

- MCA Amptek-8000D: A high-speed digital MCA compatible with an analog pulse shaping systems and a high speed 16 bit ADC, that digitizes the analog signal from the ASIC providing us with pulse height and pulse height spectrum;

[1] https://www.ni.com/it-it.html
[2] https://www.amptek.com/products/multichannel-analyzers/mca-8000d-digital-multichannel-analyzer

- NI USB 6259 Mass Termination: NI USB 6259 Mass termination device includes a total of 48 digital channels with 32 Digital Input/Output pins (PO) and 16 digital trigger pins, with each terminal capable of being programmed as an input or output. The board includes 16 ADC that were used with the same function of the MCA to digitize X and γ branch analogue signals ;

- Software Interface: We developed the software to configure the ASIC and command the data acquisition in LabVIEW. A complete description of the software is in Appendix D;

- Low Power Supply EX752M Multi-Mode PSU, that provides power to ORION I FE and ORION I BE;

- High Power Supply (HPS): to provide power supply to the SDD onboard the BE-6.

4.3 Functionality tests

The standard testing procedure of any prototype is divided into three steps: functionality, performance and environmental testing.

Functionality tests are necessary to ensure that all components of the full detector are working. Thus, their aim is to verify that it meets the requirements and that no functional discrepancy or misconfiguration is present.

In the following, we discuss the procedure for the functionality tests. In Figure 4.3, we show a diagram explaining the order by which the different tests were performed. Firstly, we aim at testing whether ORION I is able to read the charge collected by the SDD and generate an appropriate semi-Gaussian. Then it was verified if the output signal amplitude, in shaper mode, was indeed proportional to the input signal amplitude; this was done with external ADCs on the NI board ADCs digitalising the analog X and γ signal stimulated both with pulser and with a radioactive calibration source. Finally, we want to verify if the internal ADC works properly, by repeating the same test.

4.3.1 Shaper Test

In this section, we report the test on ORION I in shaping mode.

When working in shaper mode, the ASIC *shapes* the input signal, which is then sent as

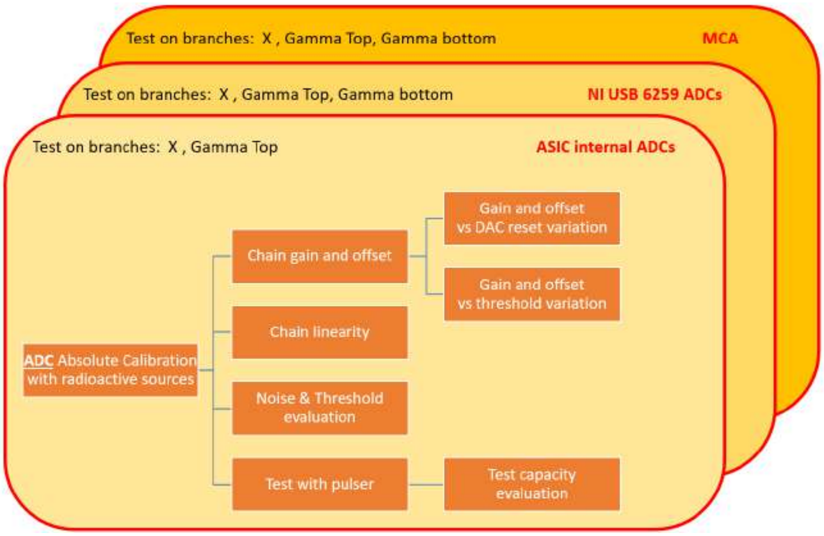

Figure 4.3: Diagram of the tests functionality procedure. The layers show the steps to follow, from the dark orange (MCA) as initial test, to light orange (ASIC internal ADCs) as final functionality test.

an analog output, giving a semi-Gaussian fit proportional to the energy of the incoming photon (see Section 3.5.2.1).
The test was done irradiating the SDD with a radioactive source (Am-241) and connecting the tested channel output, for example the shaped X branch signal (see Figure 3.13) to the MCA. Internal discrimination, stretching and ADC operations were disabled. The result confirms the correct operation of this block (see Figure 4.4). If the externally digitized analog signal corresponds to the input impulses, the shaper is working properly. Indeed, the obtained spectrum coincides with what is expected from Am-241.

4.3.2 Peak Discriminator and Peak Stretching Test

The test was done irradiating the SDD with a radioactive source (Am-241), with internal discrimination and stretching functions enabled and ADC operation disabled. The signal under test, for example the stretched X branch signal (see Figure 3.13 and Figure 3.18) was connected to the ADC of the NI 6259 board whose operation was commanded for example by the Trigger X Internal discrimination. The resulting spectra, in Figure 4.5, shows that also with a different scale the same features of the spectra of Figure 4.4 is obtained, confirming the correct operation of this block.

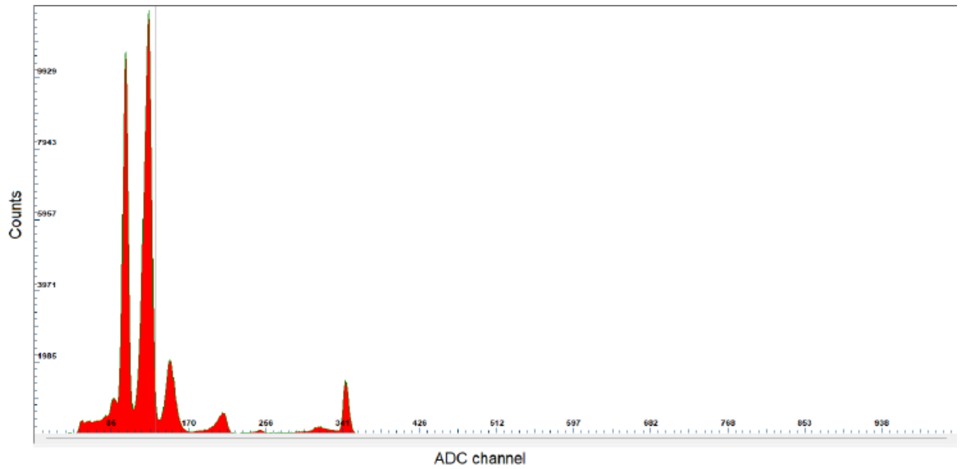

Figure 4.4: Histogram of events taken in shaping mode (X branch).

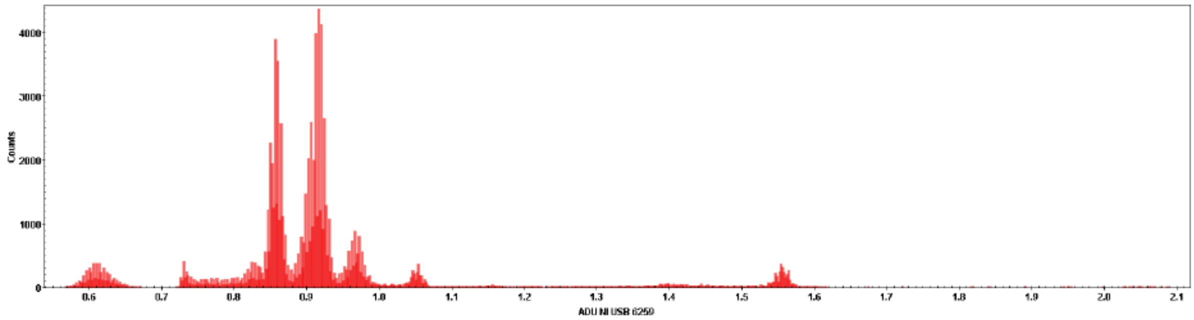

Figure 4.5: Histogram of the event in the X branch, taken in stretcher mode, acquired with the external ADC.

4.3.3 Internal ADC tests

The test was done irradiating the SDD with a radioactive source (Am-241), with internal discrimination, stretching and ADC functions enabled. The ASIC digital data were collected, and organized as a spectrum. The result is shown in is in Figure 4.6 that does not differ for the structure of the spectra of Figure 4.4 and 4.5, confirming the correct operation of this block.

4.3.4 Dynamic range Test

One of the main requirements for THESEUS/XGIS regards its dynamic range, i.e. the range at which it is able to operate. This value, which we report in units of electrons, represents the energy band in which the instrument is able to detect photons. Since XGIS is required to operate in the range of 2 keV to 10 MeV (Section 2.3.1.2), this test will verify if the electronics are able to operate in the equivalent range of 540 e^- to 90000

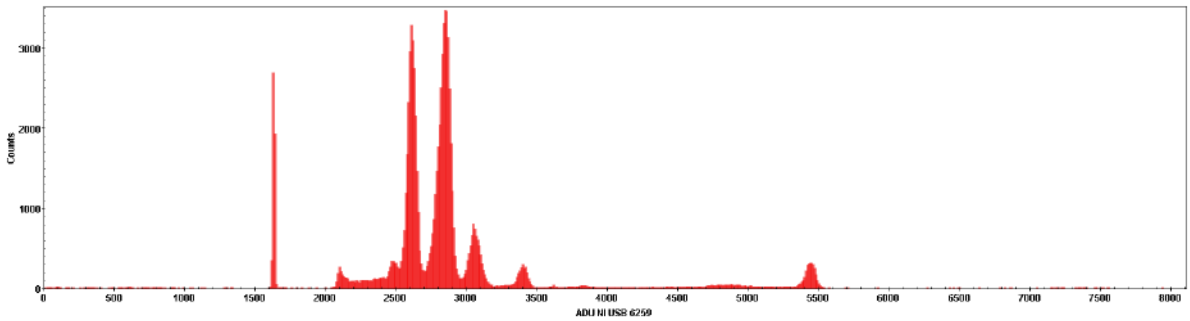

Figure 4.6: Histogram of Am-241 spectrum (X branch), taken in stretcher mode, with the internal ADC of the ORION I ASIC.

e$^-$, as listed in Table 4.1 (Mele et al. 2021).

Parameter (°C)	X-Processor	γ-Processor
Detector	SDD	CsI(Tl) + 2 × SDDs
Temperature range	[-20 °C ; +20 °C]	
Linear range in charge	0–10 000 e$^-$ ($\sim$ 30 keV)	0–90 000 e$^-$ ($\sim$ 10 MeV)
Peaking time	1 μs	3 μ s
Linearity Error	± 1	
ENC(equivalent noise charge) at -20°	$\sim$ 15 e$^-$ rms	$\sim$ 50 e$^-$ rms

Table 4.1: Orion Multichip Redout Electronic Requirements (Mele et al. 2021).

To cover the full range of charges required in the X and gamma branches, the test was done stimulating the *Test input* pin with electrical pulses of different amplitudes and a shape similar to the signal produced in the SDD (see Figure 3.14). The ORION-BE was operate in shaper mode with internal discrimination, stretching and ADC funtions disabled, and the ASIC analogue data send to the MCA to collect spectra. Through the *Test input* an external pulse can stimulate the ASIC input via a test capacitor embedded in the ASIC, this capacitor, with a nominal value of 20 fF, allows to inject pulses with defined charge. We configure ORION I ASIC in shaper with the LabVIEW program.
We report also the equivalent energy of the impulses. To obtain the equivalent energies that these impulse amplitudes represent, we follow the procedure described in Campana et al. (2022).

Considering a test capacitance of 20 fF (Bertuccio et al. 2021b,a), the charge of the electron as 1.6×10^{-19} C, and that the energy needed to generate a couple e-/hole is of 3.65 eV (Mazziotta 2008), it follows that the energy E of the equivalent X-ray photon is:

$$E(keV) = Q(e^-) \times \frac{3.65}{1000} \tag{4.1}$$

Similarly, considering a realistic light yield of an electron as $\sim$ 25 e$^-$/keV for a γ ray event, given the detector design (Marisaldi et al. 2005), and assuming an equal partition between the charge collected at the Top and Bottom SDDs, then it follows that the energy E of the equivalent gamma-ray photon is:

$$E(keV) = \frac{Q}{12.5e^-/keV} \tag{4.2}$$

We report the dynamic range values for each channel, and their equivalent energies, in Table 4.2.

	Pulser (mV)	Equivalent Energy (keV)	Equivalent electrons (e$^-$)
X (Shaper)	9–310	4.1 –141.4	1123–38740
X (Stretcher)	36–310	16.4–141.4	4493–38740
γ Top (Shaper)	10–3500	100–35000	1250–437500
γ Top (Stretcher)	90–3500	900–35000	11250–437500

Table 4.2: Results from the dynamic range testing of ORION I. The input impulses were given at a frequency of 100 Hz. In the first column, we report the tested channel and operating mode. In the second column the minimum and maximum impulse amplitudes for which the system operates properly, in mV, and in the third column we report their equivalent energy in keV. For the calculation, a 20 fF value for the test capacitance was assumed.

As we can see in Table 4.2 ORION I this version of ORION I displays a wider dynamic range than what is required (2 keV –10 MeV)
It is also a wider dynamic range than that of Marchesini et al. (2021). This is due to the fact that the acquisition software they implemented was not able to keep track of data acquired above an equivalent energy of around 8000 keV. We developed a new acquisition software (see Appendix D), adjusted to the capabilities of ORION I. This way, we can now achieve compliance with the THESEUS/XGIS requirements regarding dynamic range, as listed in Table 4.1.

4.3.5 Gain vs Threshold Test

The aim of this test is to verify if there is a dependency between the gain of the X and gamma branches and the discriminator threshold, that is a programmable parameter. This behaviour was noticed in the Lyra ASIC of HERMES (Baroni 2022) of wich the ORION ASIC is an evolution, and is unwanted. The test, conducted in the same operative conditions of the previously described test, was done changing the threshold values to 80, 100, 120. All of these tests were performed for two different PCB prototypes, BE-5 and BE-6. In Figure 4.7, the results for BE-6 are shown. The X and gamma bottom branches work nominally.

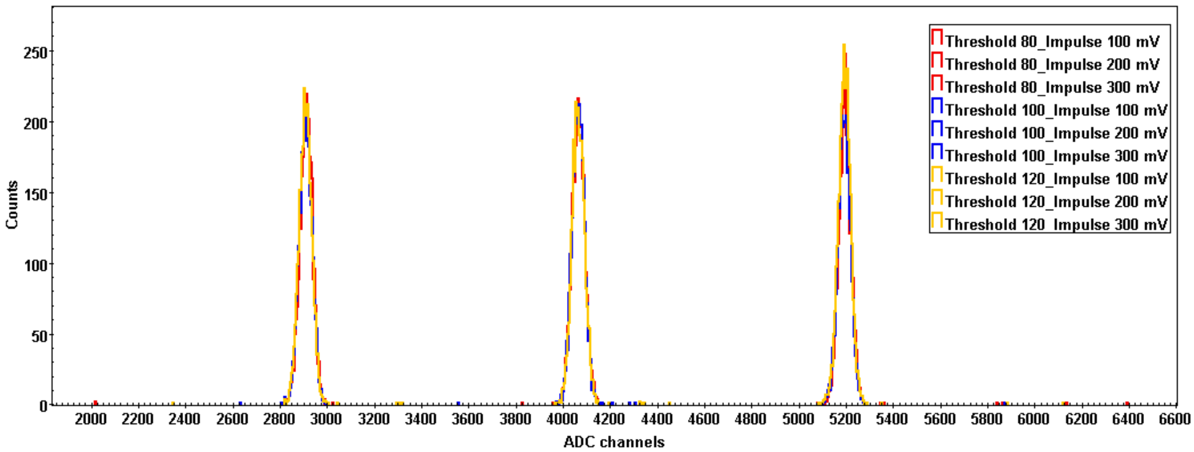

Figure 4.7: Several X-branch spectra of impulses of 100, 200 and 300 mV, with threshold values of 80, 100, 120, for prototype board BE-6.

4.4 Performance tests

Performance tests aim at verifying that the detector is not only functioning, but that is also operating within the expected performance values. These requirements are strictly related to the science goals of a given detector, since they involve crucial instrumental characteristics such as sensitivity, resolution and operating waveband. The main purpose for these tests was performed to characterize the behaviour of the ORION-FE-BE and, in particular:

- the energy calibration, energy resolution, and the linearity of ORION-FE-BE X and γ branch;

- measure the internal test capacitance of the ORION-FE-BE;
- measure the noise of the X and γ branches.

4.4.1 Energy Calibration

As mentioned, in Section 4.3.4, on average one electron is produced for every 3.65 eV of energy deposited into an SDD by incoming photons, at a temperature of 300 K (Mazziotta 2008). This means that there is a linear, proportional relation between the incoming X-ray photons and the output signal amplitude from the anode.
The calibration of all the spectra collected with ORION I, in every configuration, is performed with a pipeline called `MESCAL` (Marchesini et al. 2023), which we adapted specifically for the ORION data analysis. For each spectral line, `MESCAL` determines the parameters of the fitting Gaussian (amplitude, peak-channel, sigma) and then the linear relation between the channel and the energy:

$$Y(ADU) = gain(ADU/e^{-}) \cdot X(e^{-}) + Offset(ADU) \tag{4.3}$$

where Y and Offset are in instrumental units, E is in keV and gain is in ADU/keV, where ADU stand for Analog Digital Units (also referred as channels).
We used radioactive sources with emission lines of known energy, that cover all the operative range. We have chosen Fe-55 and Am-241, which emit at 5.9, and 6.4 keV (Fe-55) and 11.9, 13.7, 16.8, 17.7, 20.7, 26.3 and 59.5 keV (Am-241).
An example of the data output from the LabView software, together with a more detailed explanation on how it operates, can be found in Appendix D.

4.4.2 X Branch Calibration and Linearity

4.4.2.1 Definition of the calibration procedure

We proceeded to the acquisition of the spectra of these radioactive sources, by placing them in front of the SDD.
We take two measures, one with Fe-55 and one with Am-241 both for 20 minutes. With these two measures, we cover a wide energy range, from 5 keV to 60 keV.

The software `MESCAL` performs a Gaussian fit for every line in the histogram. The software allows a quick evaluation of the goodness of the fit, as can be seen in Figure 4.8.

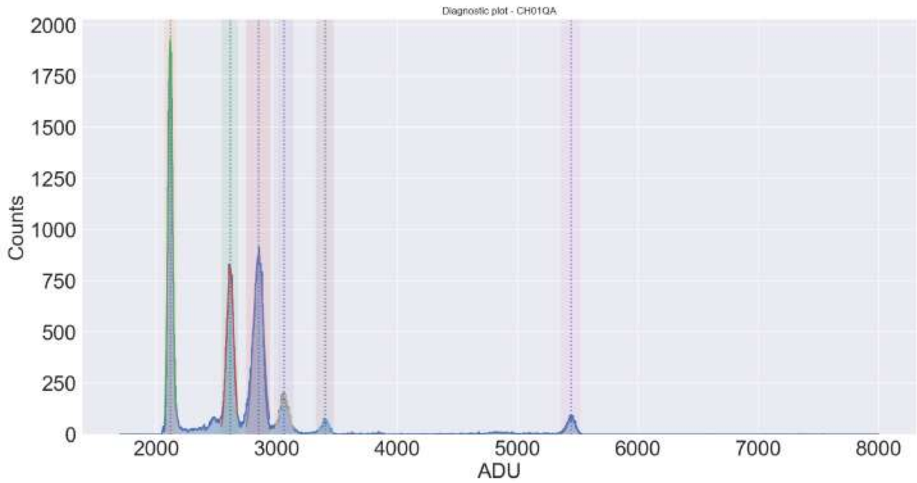

Figure 4.8: Fit of the joined spectra of Am-241 and Fe-55 in the X branch (expressed in ADU, analog to digital unit). The shaded, colored areas represent the ranges in which the software detected a feature. The solid, colored lines represent the resulting best fit of these features, obtained by the least-squares fitting of a Gaussian profile. The dotted lines represent the mean of these fitted functions.

For every line, with its relative tabulated energy, we obtain the center in ADU and its error, the FWHM of the Gaussian fit and its error, and the amplitude and its error. We report our results in Table 4.3.

Emission line	Centroid (ADU)	FWHM (ADU)	Amplitude (counts)
Fe 5.9 keV	2116,4 ± 0,3	44.5 ± 0.8	91514 ± 1404
Am 13.7 keV	2613.7 ± 0.5	69.9 ± 1.6	60883 ± 1125
Am 17.7 keV	2849.2 ± 1.0	97.9 ± 2.8	91493 ± 2150
Am 20.7 keV	3061.3 ± 1.0	89.4 ± 2.8	18431 ± 474
Am 26.3 keV	3403.9 ± 1.4	75.5 ± 4.0	5491 ± 240
Am 59.5 keV	5446.9 ± 1.5	78.0 ± 4.4	7318 ± 339

Table 4.3: Results of Gaussian fit 5 lines of Am-241 (13.7 keV, 17.7 keV,20.7 keV, 26.3 keV, 59.5 keV) and Fe-55 (5.9 keV) with `MESCAL`. The columns are, from left to right: energy of the line; the centroid of the line from the fit in ADU; the FWHM of the line in ADU; and the amplitude of the line from the fit in counts. Errors are 1σ.

Then the SW performs a linear fit between the tabulated energies of the lines, and their Gaussian centroids in ADUs. This way, the linear function parameters (slope, or gain, and offset), and a Pearson correlation coefficient are shown in Table 4.4.

Gain (ADU/keV)	Offset (ch)	Pearson correlation index
61.8±0.2	1771±9	0.99993

Table 4.4: Gain, Offset and Pearson correlation coefficient obtained with software `MESCAL`.

The calibrated spectrum is shown in Figure 4.9. The spectrum shows a shift in the 5.9 keV line of Fe-55. The `MESCAL` software also provides a plot with the data, the chosen best fit and the residuals. This plot is shown in Figure 4.10, in which the Fe-55 line shift is apparent.

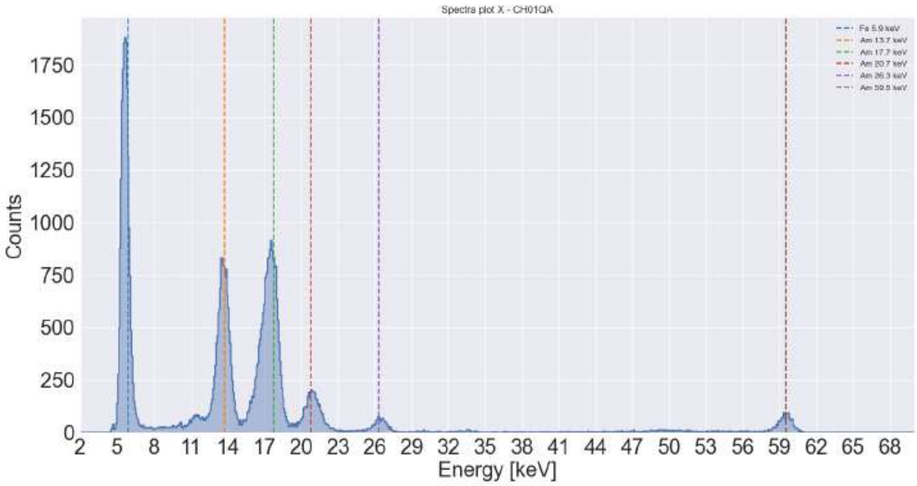

Figure 4.9: Calibrated spectrum of the joined spectra of Am-241 and Fe-55 in the X branch. Dotted lines represent the real, tabulated energy of each emission line.

From Figure 4.9 and 4.10 preliminary conclusions can be derived. We noticed that the 5.9 keV Fe-55 peak shows a deviation of linearity of around 1.5%. This issue may be due to the inclusion of the 59.5 keV line of Am-241 in the calibration procedure. A 60 keV photon corresponds to 16300 electrons generated in the SDD, and with very low efficiency (around 5%, Fuschino et al. (2021)). The requirements for the XGIS system (see Table 4.1) state that the X-Branch should be linear up to 10000 e^-. Thus, the 59.5

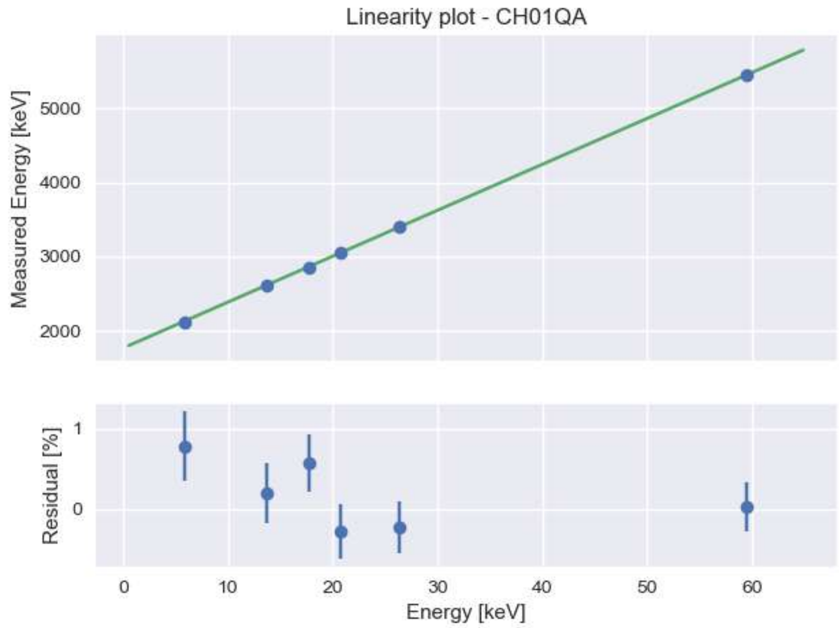

Figure 4.10: Upper panel: Linearity fit of the AM-241, Fe-55 spectra. Lower: Residuals in percentage of the energy value.

keV line can be excluded from the analysis. Furthermore, the Fe-55 line displays a sharp cutoff towards the lower energies, which could indicate that the threshold value used was too high to completely sample the line profile.

We made a new calibration excluding the 59.5 peak. The calibration parameters derived from this new fit are reported in Table 4.5. The resulting calibrated spectrum is shown in Figure 4.11. The calibration has improved, since there is little to no shift present in the 5.9 keV Fe55 line. This can be seen from the linearity plot, which we show in Figure 4.12.

Gain (ADU/keV)	Offset (ch)	Pearson correlation coefficient
63.7±0.8	1727±18	0.9998

Table 4.5: Gain, Offset and Pearson correlation coefficient obtained for the second energy calibration.

For the Fe-55 line the peak parameter indicate a centroid at ADU 2116.5 that, using the calibration parameter of Table 4.5 results in a 6.06 keV energy, which is above the

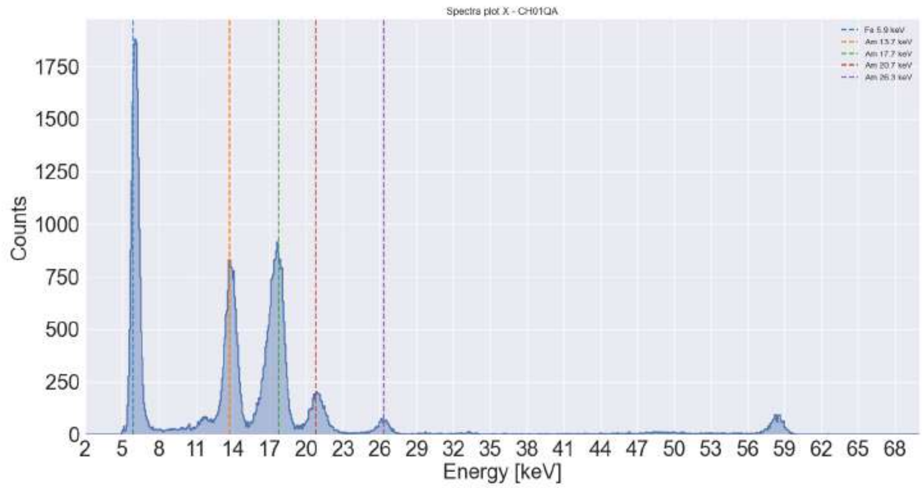

Figure 4.11: Second calibrated spectrum of the joined spectra of Am-241 and Fe-55 in the X branch (5.9, 13.7,17.7, 20.7, 26.3 keV). Dotted lines represent the real, tabulated energy of each emission line.

numerical error. This effect seems due to the threshold of the ASIC that *cuts* the lower part of the peak. This is a feature of the discriminator of the ORION I ASIC. When acquired with an external ADC, i.e. in a configuration where the ASIC threshold has no effect, the Fe-55 line is in its correct position (see Figure 4.13). The ASIC discriminator problem of ORION I was partly solved in the successive version of the ASIC.

4.4.3 γ branch Calibration and Linearity

For the γ-bottom chain, we can only check the linearity with the test pulse, since it is not connected to an SDD. In this version, we have only the γ-Top connected to the SDD. The γ branch has a gain 8 times lower that that of the X branch. Due to the discriminator threshold behaviour, when the SDD is exposed to Am241 radiation, the γ branch can only detect the emission lines with the highest energies, i.e. 26.3 and 59.5 keV. The latter is detected by the SDD with an efficiency of less than 5% (Fuschino et al. 2021), which renders it too faint for calibration purposes (see Figure 4.14). Thus we calibrated the whole gamma branch only with test impulses. We acquired a spectrum of 5 electric impulses within the gamma operative range (see Figure 4.15).

It is evident that the two lower impulses are deviated from the linear regime. We show the linearity plot of this fit in Figure 4.16.

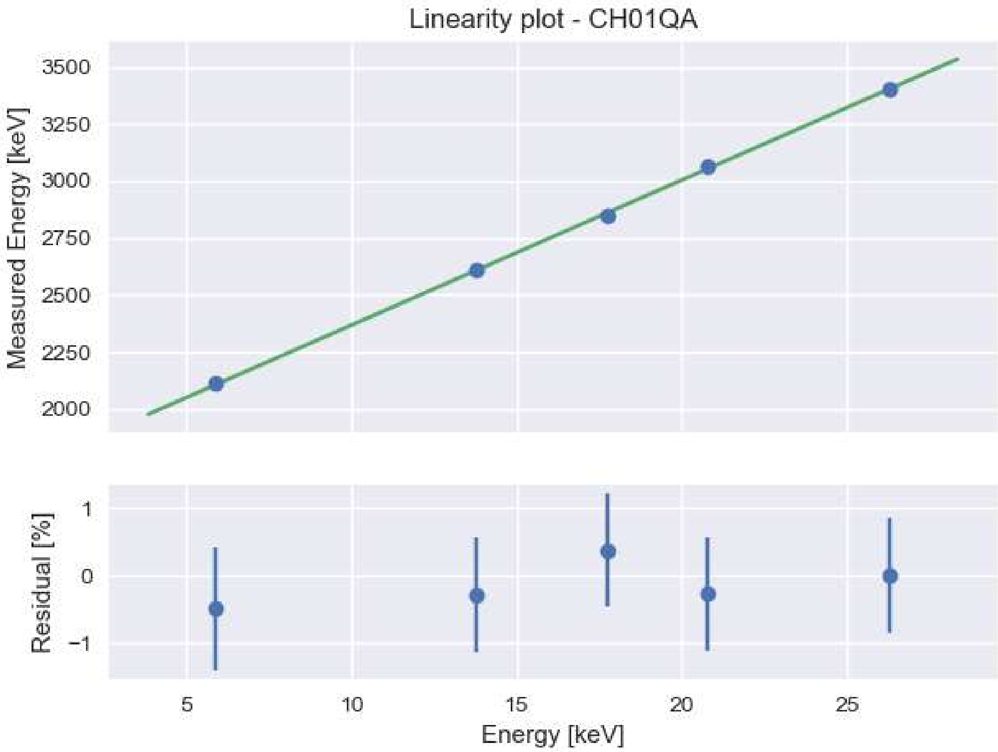

Figure 4.12: Upper panel: Linearity fit of the Am-241 and Fe-55 spectra, without considering the 59.5 keV Am-241 emission line. Lower: Residuals as a percentage of the energy value.

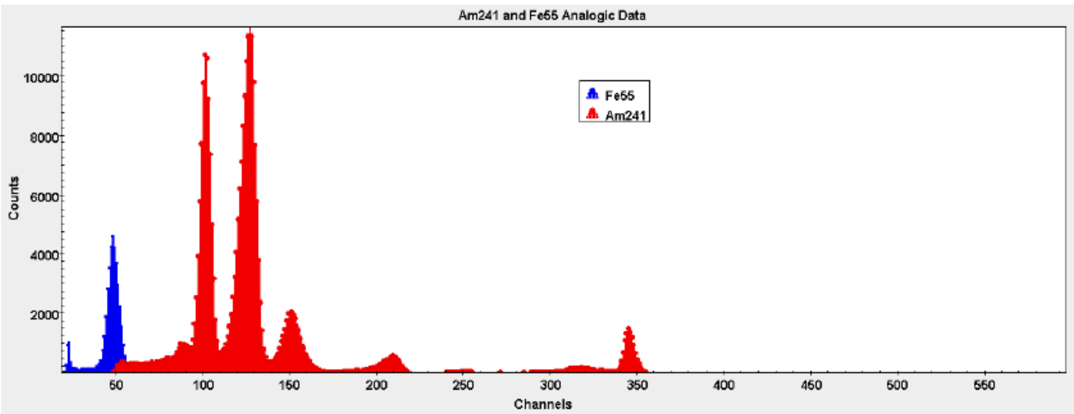

Figure 4.13: Histrogram of events taken with MCA in shaper mode, from the X branch ORION I, with Fe-55 and Am-241.

The deviation of these features is of around 2 % at 100 mV. This means that the dynamic range for the γ processor is 98% in the range from 1 to 30 MeV, which is slightly lower

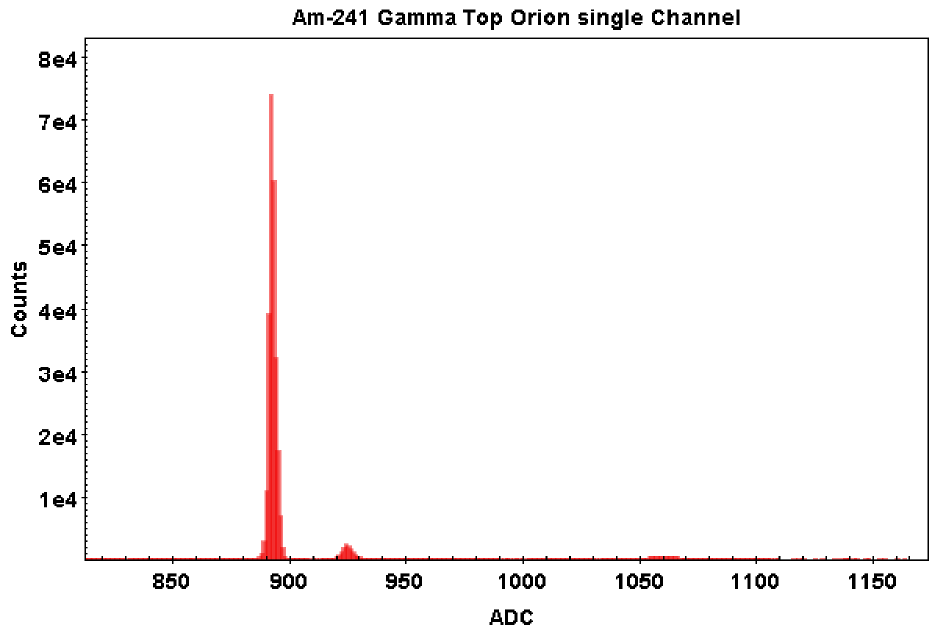

Figure 4.14: Spectrum of Am-241 in the γ-Top branch, taken in stretcher mode, analyzed with the internal ADC of the ORION I ASIC.

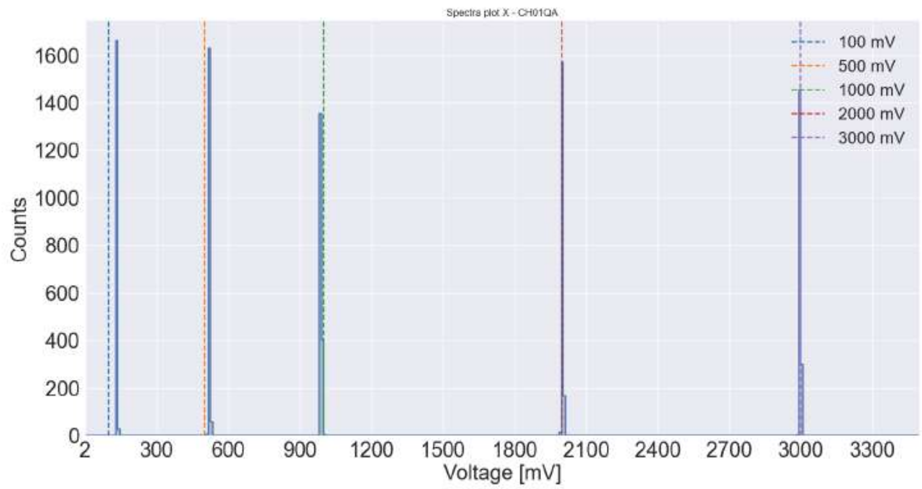

Figure 4.15: Calibrated spectrum of the 5 pulses (100, 500, 1000, 2000, 3000 mV) in the γ-Top branch, with counts and voltage (mV). Dotted lines represent the real, tabulated voltage of each line.

than what was reported by both Mele et al. (2021) and Grassi et al. (2022), of 98.5%. However, it is worth noting that our measurements cover a much wider dynamic range.

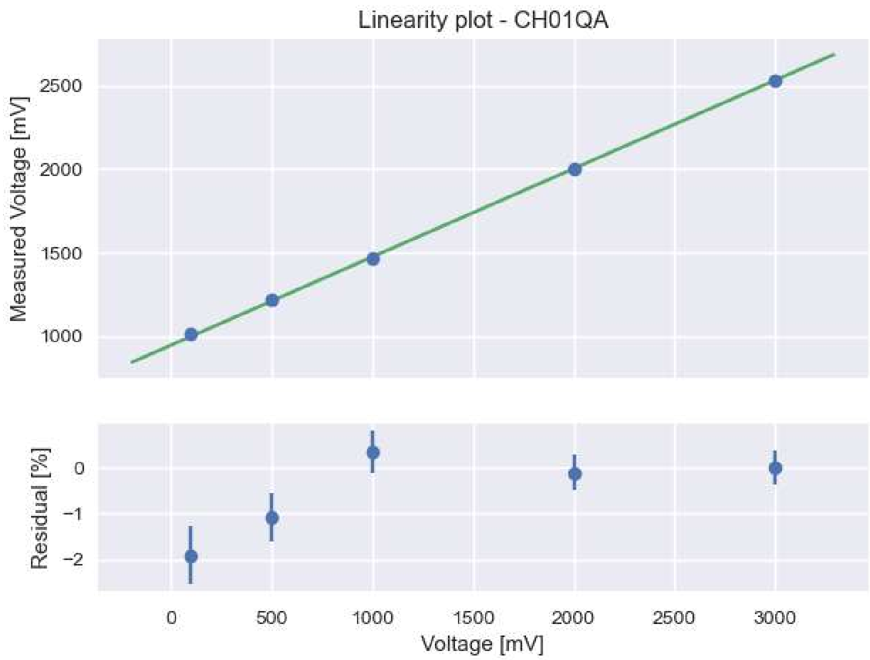

Figure 4.16: Upper panel: Linearity fit of the centroids of the pulser in the γ-Top branch. Lower: Residuals in percentage of the energy value.

4.4.4 Electronic noise evaluation

The evaluation of the electronic noise, in this case of the X-branch, is derived from the width of the measured peak. It is usual to estimate the electrical noise in e^- r.m.s. so it is convenient to change the representation of a spectra (e.g. Figure 4.12) in e^- instead of keV. The total width of a peak is determined by the statistical noise and the electrical noise by the relation 4.4:

$$\sigma_{tot}^2 = \sigma_{el}^2 + \sigma_P^2 \tag{4.4}$$

Where σ_{tot} denotes the total noise, σ_{el} the electronic noise and σ_P the statistical noise, that follows a Poisson statistic and depends on the number of detected electron being the square root of detected electrons corrected for semiconductor detector by a Fano factor that in Silicon is 0.1 (Perotti & Fiorini 1999). Assuming a Gaussian distribution of the total noise, the electronic noise can be derived as a function of the Full Width at Half Maximum (FWHM) as:

$$\sigma_{tot} = FWHM/2.355 \tag{4.5}$$

$$\sigma_{el}^2 = \frac{FWHM}{2.355} - 0.1 \times \sqrt{N_e} \tag{4.6}$$

where N_e is the number of detected electrons.

The measured electronic noise is of the order of $\sim$ 117.4 e^- much greater than expected (see Table 4.1) and probably due to the quality of the SDD.

Line energy (keV)	$\sigma_{\rm tot}$ $(e^-)r.m.s.$	$\sigma_{\rm P}$ $(e^-)r.m.s.$	$\sigma_{\rm el}$ (e^-) r.m.s.
6.95	130.3	4.4	130.2
18.5	115.1	7.1	114.9
37.2	114.0	10.1	113.6
55.4	111.5	12.3	111.0

Table 4.6: Results from the calculation of the electronic noise. In column 1 we report the equivalent energy of the pulser line; in column 2 the total noise of the lines; in column 3 Poissonial noise; in the final column the electrical noise.

4.4.5 Capacitance Test

The aim of this test is to verify the ORION I internal test capacitance of the test board. This test was performed the X channel, since an absolute energy calibration is needed. To study the internal test capacitance of the ASIC we need to do a test impulse and a source calibration. The impulses input voltage will be converted into energy with the gain and offset of the energy calibration, using the same linear formula as in Equation 4.3. These values will be converted into charge. Then, the charge of each peak can be calibrated with the relation 4.7:

$$Q(C) = \frac{E(keV)}{3.65(eV/e^-)} \times 1.6 \times 10^{-19}(C/e^-) \tag{4.7}$$

where Q is the charge, in Coulomb, corresponding to the peak of Energy E, in eV, 3.65 (eV) is the energy necessary to produce an e^-/hole pair in Silicon, and 1.6×10^{-19} is the e- charge in Coulomb. With the charge and the input voltage, it is straightforward to derive the capacity, defined as:

$$C = Q(C)/V(V) \tag{4.8}$$

The fit plot of the four pulses used for the test is shown in Figure 4.17.

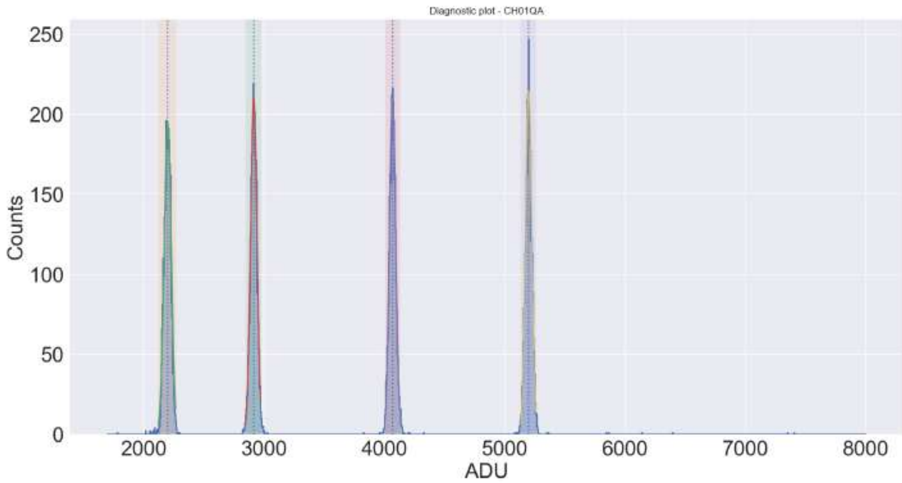

Figure 4.17: Gaussian fit of 4 pulses int he X branch (40 mV, 100 mV, 200 mV, 300 mV). The shaded, colored areas represent the ranges in which the software detected a feature. The solid, colored lines represent the resulting best fit of these features, obtained by the least-squares fitting of a Gaussian profile. The dotted lines represent the mean of these fitted functions.

The results are reported in Table 4.7. Averaging over all the lines used in the calibration, we derived a mean capacitance of C=8.0±0.7.

Energy (keV)	Voltage (V)	Charge (e^-)	Charge (C)	Capacitance (fF)
6.90	0.04	1891 ± 130	$3.0 \pm 0.2 \cdot 10^{-16}$	7.6 ± 0.5
18.5	0.1	5063 ± 115	$8.1 \pm 0.2 \cdot 10^{-16}$	8.1 ± 0.2
37.2	0.2	10176 ± 114	$1.63 \pm 0.02 \cdot 10^{-15}$	8.1± 0.1
55.4	0.3	15185 ± 112	$2.43 \pm 0.02 \cdot 10^{-15}$	8.1 ± 0.16

Table 4.7: Results from the calculation of the capacitance. In column 1 is present the equivalent energy, in column 2 the change in electron, in column 3 the charge in Coulomb, in column 4 the voltage; and 5 the capacity and their respective errors, that were derived for every impulse. Errros are 1σ.

This value is significantly lower than the one found by Mele et al. (2021) and by Grassi et al. (2022), which is 20 fF. The two values are not compatible even within the errors. This could be related to the fact that we are using an SDD significantly different, in geometry with respect to the one for which ORION I was designed, thus the longer bonding wires may be contributing to the stray capacitance of ORION I.

4.5 Environmental tests

The XGIS SDD is required to operate in the temperature range of -30 °C to +10 °C (Labanti et al. 2021b). Moreover, it is required that it can sustain severe vibrations, produced during the launch, and particle bombardment, which is normal during certain orbital phases (ECSS 2008). Thus, environmental tests aim at evaluating the capacity of the system to operate in space conditions, while maintaining its performance.

4.5.1 Thermal Cycle Test

The aim of this test is to verify that the detector works properly at different temperatures while maintaining its performance (see Section 4.4). The spectral resolution, in particular, can even be improved at lower temperatures, due to reduced thermal noise contribution (Gilmore 2008).

The aim of this test is to verify that the detector works properly at different temperatures, while maintaining its performance. This test was done inside the Climatic Chamber (from now on CC) at INAF/OAS laboratories in Bologna. We acquired 5 measures of the Am-241 starting from room temperature $\sim 22°$ C, in a step of 10 °C down to -20°C. The System under test was food with dry Nitrogen to avoid water vapor to contaminate the circuitery. With the software WinKratos [3] we programmed the CC to vary the internal temperature as needed.

At -20 °C, the experiment failed. A visual inspection at the microscope showed that the bondings between the SDD and the ASIC-FE were broken. In Table 4.8 the noise measured before system damage is reported.

The FWHM of ORION I is compatible with a value of 1000 eV at 0° for the 13.7 keV line of Am-241.

We conclude that the test setup setup needs to be enhanced to avoid both stray capacity contribution, and extra noise contribution. Moreover, the implementation of the

[3] `https://www.acstestchambers.com/it/software/`

Temperature CC (°C)	σ_{tot} (e^-) r.m.s.
20	125 ± 2
10	123 ± 1
0	117 ± 2
-10	128 ± 1

Table 4.8: Results from the line of Am-241 13.7 keV from the Software `MESCAL`. For the different temperature of the measures is presented the σ_{tot} in electrons.

THESEUS SDDs may help avoiding issues due to a difference in the thermal expansion coefficients involved.

Chapter 5

Characterization of the four-channel ORION IV ASIC

In this chapter we describe in detail the testing of the ORION Four Channels ASIC (from now on called ORION IV) with eight SDDs connected, and without scintillator crystal, following the testing of the ORION single channel ASIC described in Chapter 4. The ASIC circuit is presented in Section 5.1. We will show the test setup in Section 5.2, and the procedure and the result of the functionality tests in Section 5.3. The procedure and the results of the performance test are presented in Section 5.4. In particular, we will describe the energy calibration and linearity of the X branch, Section 5.4.1 and the energy calibration and linearity of the γ branch, Section 5.4.2.

5.1 ORION IV ASIC circuit

The ORION Four Channels ASIC consists of an evolution of the ORION I. The system under test is assembled on the Printed Circuit Board (PCB) W92-3, Figure 5.1, and consist of:

- A top PCB with an array of 4 SDD, each one of the same size (5×5 mm^2) and electrically similar to the XGIS ones, and 4 ORION-FE version II that electrically are as the first version but with a modified topology;
- A bottom PCB with an array of 4 SDD and 4 ORION-FE version II, plus an ORION-BE.

The top and bottom PCB are electrically connected (flat wire $\sim$ 3 cm long) so that all the 4+4 ORION-FE signals are connected to the ORION-BE IV. Furthermore the 4 top SDD are mechanically aligned to the 4 bottom SDD so that four scintillator elements can be mounted. The scintillators were not present during these tests.

5.1.1 Logic elements of ORION IV

The ORION IV includes 4 channels with the same structure and logic of the ORION I version in Figure 3.13, plus some circuitry to send the data via a serial interface. As in the first version, external pins are available as probes for the discriminators of the X and gamma branches, their logical OR, and the LAM (Look At Me) signal indicating the readiness of the digital data. In ORION IV each of these signals is the OR of the corresponding signal in the 4 channels.

5.2 Test setup

The test setup consists of a modified version with a similar structure of the one presented in Section 4.2 for ORION Single Channel. The main power supply, data configuration and data acquisition components of the test setup are shown in Figure 5.2.
As in the previous ORION I the Test Equipemt (TE) was based on a NI board with the function of commanding the ASIC setting, and ASIC interface during operation and data acquisition. The Labview SW was updated and adapted to serial data exchange; care was done in the hardware setting, electrically shielding the system to reduce extra noise due to the system noise.

5.3 Functionality tests

We report the procedure for the functionality tests, as done for the previous prototype, see Section 4.3. In Figure 5.3, we show a diagram explaining the order by which the different tests were performed. Firstly, we aim at testing whether ORION IV is able to read the charge collected by the SDD and generate an appropriate semi-Gaussian form to fit the received signal, both in X and γ branches. For Orion IV, we skipped the tests

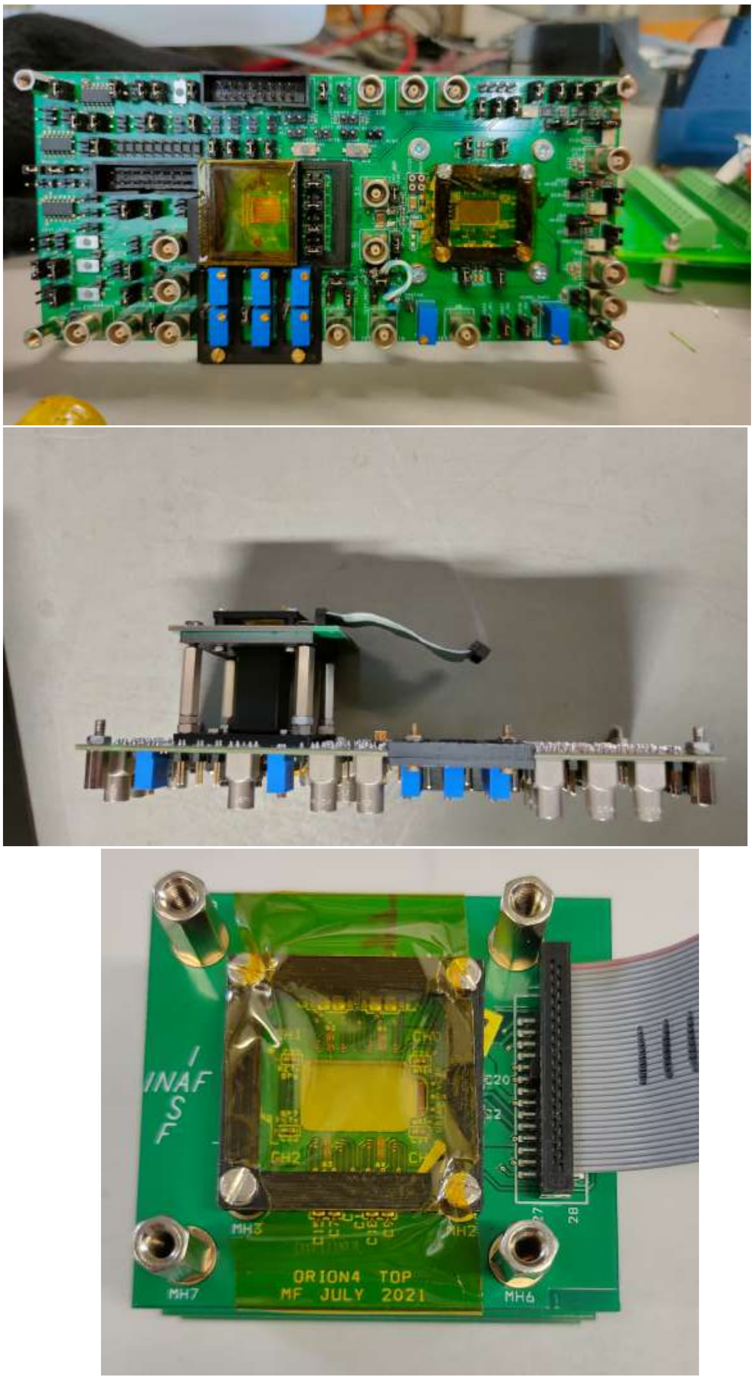

Figure 5.1: Images of the test board W92-3. Upper: Front view of the board where the 4 bottom SDD, the 4 FEs and the BE are placed. Middle: side view of the board where the flat wires connect the SDD Top to the SDD Bottom. From this angle, the dedicated place for the scintillation crystal is evident. Bottom: View of the ORION IV Top, with the 4 FEs and 4 SDDs and the flat wires that connect to the BE.

done with the external ADC, going directly to testing the internal ADC. We want to verify if the internal ADC is able to properly digitize the analogic output, and compare

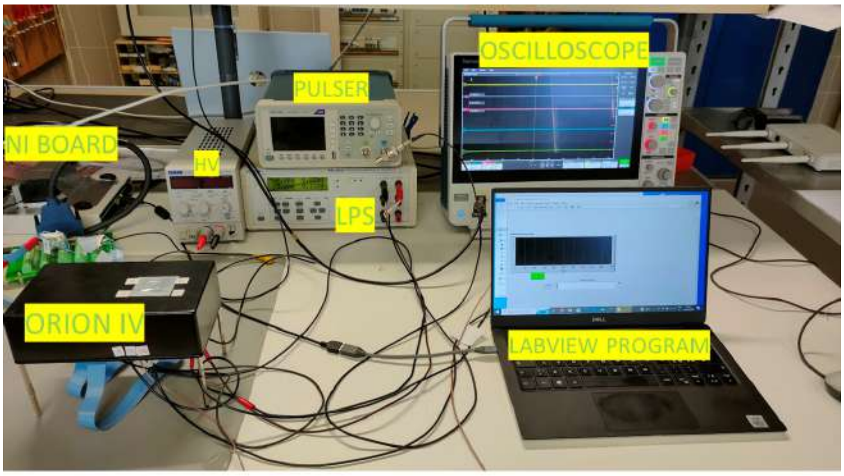

Figure 5.2: Image of the Test setup for ORION IV. In the image the LabVIEW program in the user interface, the box which contains the prototype of ORION IV, the LPS and HV, the NI board, the pulser, and the oscilloscope are shown.

this output spectrum with the spectrum of the calibration source.

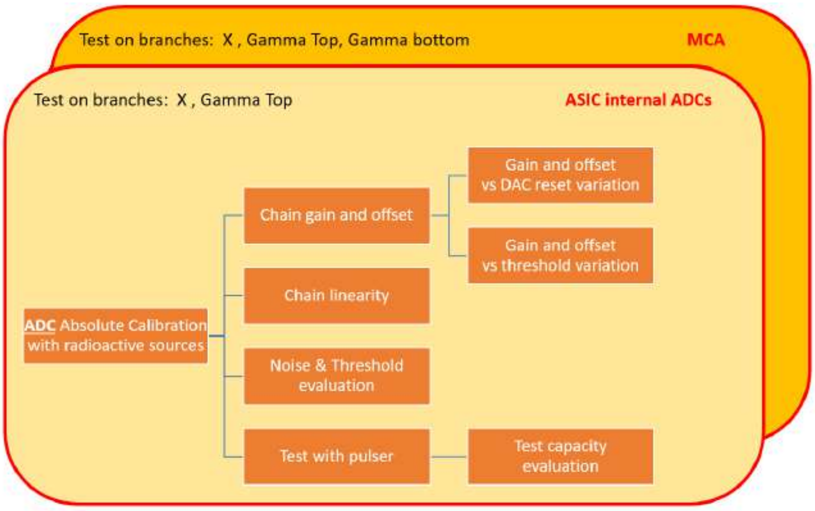

Figure 5.3: Diagram of the tests functionality procedure. The layers show the steps to followed, from the dark orange (MCA) as the initial test, to light orange (ASIC internal ADCs) as the final functionality test.

5.3.1 Shaper Test

In this section, we test the ORION IV shaper mode. We want to verify the correct behaviour of the three shaper chains, X, γ-Top, γ-Bottom with differences in time shaping and different amplification.

We expect that the signal sent with the pulser is shaped properly by the ASIC. We can test this by connecting the pulser and connecting the MCA, configuring the ASIC with shaper mode enabled. This way, we avoid using the discriminator and the internal ADC (see Figure 3.13).

The correct functionality of the three shaping chains X, γ-Top, γ-Bottom of one of the channel is shown in Figure 5.4.

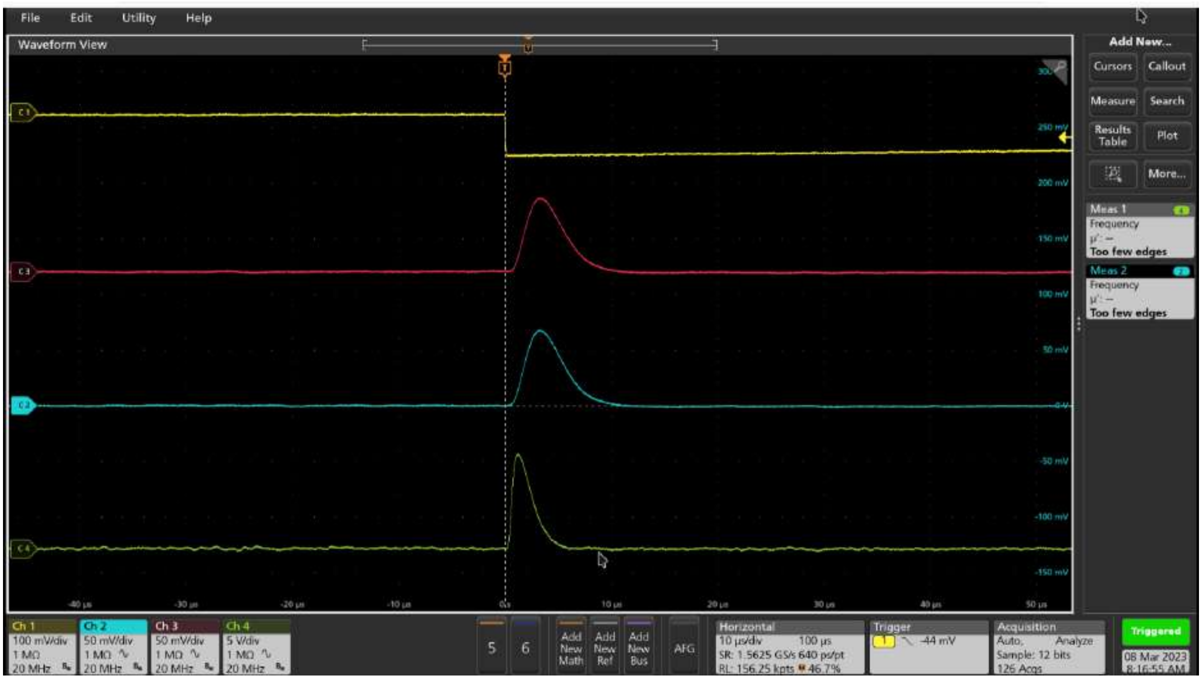

Figure 5.4: Screenshot of the oscilloscope with shaping function after the impulse. The yellow signal is the voltage test pulse. The red and blue are the shaped signal from the γ branch, Top and Bottom. The green one is the shaping of the X branch. It is possible to observe the difference in shaping time between the X branch and the γ branch.

5.3.2 ORION IV internal ADC test

In this section, we test the internal ADC of ORION, in stretcher mode. We tested the functionality of the circuits involving discriminator, stretcher and ADC, illuminating the SDD top with an Am-241 calibrated source and collecting the digital data. The obtained spectrum is shown in Figure 5.5, corresponds to the X branch of Ch.0, and means that the acquisition chain is working properly.

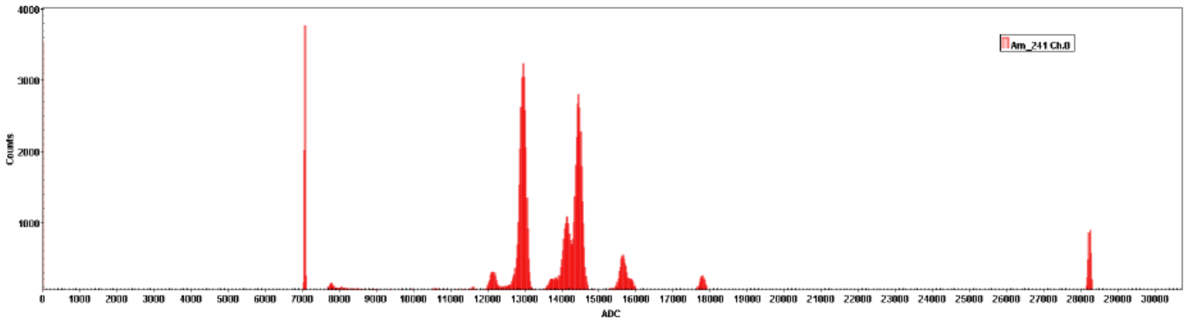

Figure 5.5: Histogram of Am-241 spectrum (X branch), taken in stretcher mode, with the internal ADC of the ORION IV ASIC.

5.3.2.1 Dynamical Range Test

With the procedure described in Section 4.3.4, we tested the dynamic range of all the channels and all the branches. The results are shown in Table 5.1. Ch.3 is highlighted in the results table, as it is the least performant.
Note that the equivalent energy for the γ branch is calculated as the energy the SDD should see if a crystal is mounted. We would like to emphasize that the reported values for the stretcher in yellow are due to issues with Channel 3, which is not functioning correctly. As a result, we had to modify the standard configuration and increase the fine thresholds for γ and X in order to ensure the proper operation of the channel.
As we can see in Table 5.1 with ORION IV we have a dynamic range that is narrower than the one of ORION I but that is compliant with the requirements, which are listed in Table 4.1.

5.4 Performance tests

The main purpose for which these tests were performed to characterize the behaviour of ORION-FE-BE, similarly to the ORION in Section 4.4. The following test were done:

- energy calibration of ORION IV for the X branch;
- energy calibration of ORION IV for the γ Bottom branch;
- linearity of ORION IV for the X branch;
- linearity of ORION IV for the γ Bottom branch;

	Pulser (mV)	Equivalent Energy (keV)	Out X (mV)	Out γ Top (mV)	Out γ Bottom (mV)
ASIC ch 0					
X (Shaper)	3–87	1.36–39.69	49.83–896.0	5.244–86	5.284– 92
X (Stretcher)	6–87	2.7–39.69	116.1–896.0	29.16–86	27.31–92
γ Top (Shaper)	3–1210	30–12100	49.83–1680	5.244–1040	5.284–1040
γ Top (Stretcher)	27–1210	270–12100	345.5–1680	41.13–1040	63.55–1040
γ Bot (Shaper)	3–1130	30–11300	49.83–1680	5.244–968	5.284– 1016
γ Bot (Stretcher)	27–1130	270–11300	347.3–1680	39.10–968	62.23–1016
ASIC ch 1					
X (Shaper)	4–85.0	1.8–38.8	74.46–912.0	5.624–120.0	6.575–79.2
X (Stretcher)	10–85.0	4.5–38.8	165.3–912	25.37–120.0	45.78–79.2
γ Top (Shaper)	4–1120	40–11200	74.46–1696	5.624–952	6.575–944
γ Top (Stretcher)	220–1120	2200–11200	1500–1696	226.3–952	245.3–944
γ Bot (Shaper)	4–1180	40–11800	74.46–1696	5.624–1000	6.575–1000
γ Bot (Stretcher)	260–1180	2600–11800	1633-1696	262.9–1000	278.5–1000
ASIC Ch 2					
X (Shaper)	5–80.0	2.3–36.5	79.59–800	15.62–88	8.492–82
X (Stretcher)	6–80.0	2.7-36.5	127.7–800	24.81–88	25.41–82
γ Top (Shaper)	3–1050	30–10500	65.00–1640	4.438–1008	6.945–1016
γ Top (Stretcher)	11–1050	110–10500	171.9-1640	22.7–1008	48.56–1016
γ Bot (Shaper)	3–1030	30–10300	70.91–1648	5.984–1000	5.814–1008
γ Bot (Stretcher)	11–1030	110–10300	179.4–1648	23.56–1000	44.73–1008
ASIC Ch 3					
X (Shaper)	5–81	2.3–36.96	77.91–880	8.009–84	6.037–68.81
X (Stretcher)	6–81	2.7–36.96	116.0–880	16.00–84	15.2–68.81
γ Top (Shaper)	4–1030	40–10300	82.69–1656	6.075–1000	5.356–900
γ Top (Stretcher)	37–1030	370–10300	458.9–1656	22.52–1000	24.03–900
γ Bot (Shaper)	4–1200	40–12000	74.23–1664	5.939–1048	4.878–1008
γ Bot (Stretcher)	240–1200	2400–12000	1.743–1664	28.36–1048	24.89–1008

Table 5.1: Results from the dynamic range testing of ORION IV. The input impulses were given at a frequency of 100 Hz. In the first column, we report the tested channel and operating mode. In the second column, the minimum and maximum impulse amplitudes for which the system operates, in mV, are reported. In the third column, we show their equivalent energy in keV. For the calculation, a 20fF capacitance was adopted. In columns 4, 5, and 6 the amplification output of the X, γ-Top, and γ-Bottom are shown. Yellow rows display the values for the stretcher in Ch.3, which has been modified from the standard configuration used in other channels.

- measure the test capacitance;
- measure the electronic noise.

The test procedures were the same described in Section 4.4.1 and were done on all the four channels of the ASIC. The γ-Top branch was considered to be similar, by design, to the γ-Bottom branch.

Prior to the energy calibration, we provide an overview of the data format used in ORION IV, during performance testing. This new version generates an event table based on the data obtained from SDD Bottom, SDD Top, and the flags from the ADC that distinguish between X, γ Top, and γ Bottom events. The *event list* describes in each line the information collected by the four channel of the ASIC for each event. The file format is shown in Figure 5.2

Ch.0							Ch.1	Ch.2	Ch.3
SDD Bottom	SDD Top	XG	TRG γ	TRG X	ADDRS	Time	...	...	...
0	9989	0	0	1	0	820247	...	...	...
0	14176	0	0	1	0	13793188	...	...	...
8073	7063	1	1	0	0	15561841	...	...	...
0	12812	0	0	1	0	193885	...	...	...
...	...	...	...	...	...	...	...	...	...

Table 5.2: Output file format, explanation of the column in the paragraph. For Ch.1, Ch.2, Ch.3 the columns repeat the same order.

The data are organized as follows for one channel, and repeated in a similar way for the next three:

- SDD Bottom, the ADC value from the bottom FE;
- SDD Top, the ADC value from the bottom FE;
- XG, a flag that can be 0 or 1 to discriminate X events (0), γ events (1);
- TRG G, a flag that can be 0 or 1, 0 in case of an X event and 1 in case of γ event;
- TRG X, a flag that can be 0 or 1, 1 in case of an X event and 0 in case of γ event;

- ADDRS, channel address, i.e. 0,1,2 or 3;
- TIME, time tag of each event.

5.4.1 X branch

5.4.1.1 Energy Calibration

The test was done exposing the four top SDD to Fe-55 and Am-241 calibration radioactive sources and collecting the spectra from the four channels. In Figure 5.6 we show the spectra from the X branch, Ch. 0. For comparison we also show the spectrum of only Am241 as seen by the gamma bottom SDD. The difference in gain of the two branches is evident. In Table 5.6 and Figure 5.7 we show the calibration results for Ch. 0, following the procedure described in Section 4.4.2. For comparison, we show the calibration results of the defective channel, Ch.3, in Figure 5.8 and Table 5.4.

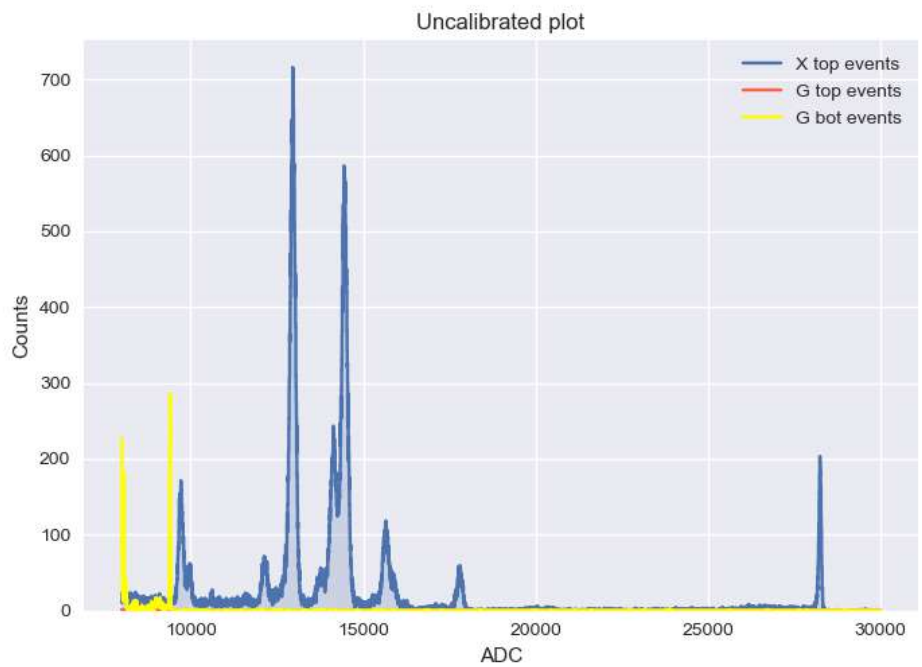

Figure 5.6: Histogram of events of Am-241 and Fe-55, in Ch.0, with counts and ADC channels (expressed in ADU, analog to digital unit). The blue line shows the X events. The red line would be γ-Top discriminated events (none are present). The yellow is γ-Bottom discriminated events.

We show in Figure 5.7 the spectrum converted into energy units.

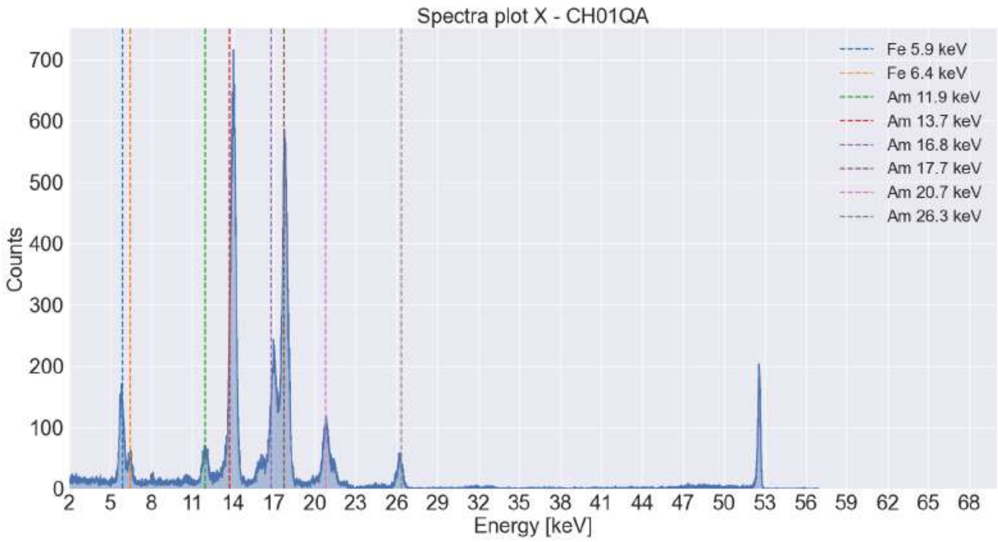

Figure 5.7: The calibrated spectrum of the joined spectra of Am-241 and Fe-55 (5.9, 6.4, 11.9, 13.7, 16.8, 17.7, 20.7, 26.3 keV) in the X branch of Ch0. Dotted lines represent the real, tabulated energy of each emission line.

Emission line (keV)	Centroid (ADU)	FWHM (ADU)	Amplitude (counts)
(1)	(2)	(3)	(4)
Fe 5.9	9717 ± 1	160 ± 3	26504 ± 459
Fe 6.4	9958 ± 4	161 ± 16	9399 ± 766
Am 11.9	1249 ± 3	222 ± 9	14816 ± 473
Am 13.7	12962 ± 1	186 ± 2	127468 ± 1401
Am 16.8	14148 ± 2	239 ± 7	54549 ± 1363
Am 17.7	14463 ± 1	203 ± 3	117670 ± 1619
Am 20.7	15665 ± 2	244 ± 7	26928 ± 627
Am 26.3	17806 ± 3	191 ± 8	10109 ± 347

Table 5.3: Results of Gaussian fit 5 lines of Am-241 (13.7 keV, 17.7 keV,20.7 keV, 26.3 keV) and Fe-55 (5.9 keV, 6.4 keV). The columns are: (1) the energy of the line; (2) the centroid of the line from the fit in ADU; (3) the FWHM of the line in ADU; (4) the amplitude of the line from the fit in counts. Errors are 1σ. Fit of Ch.0.

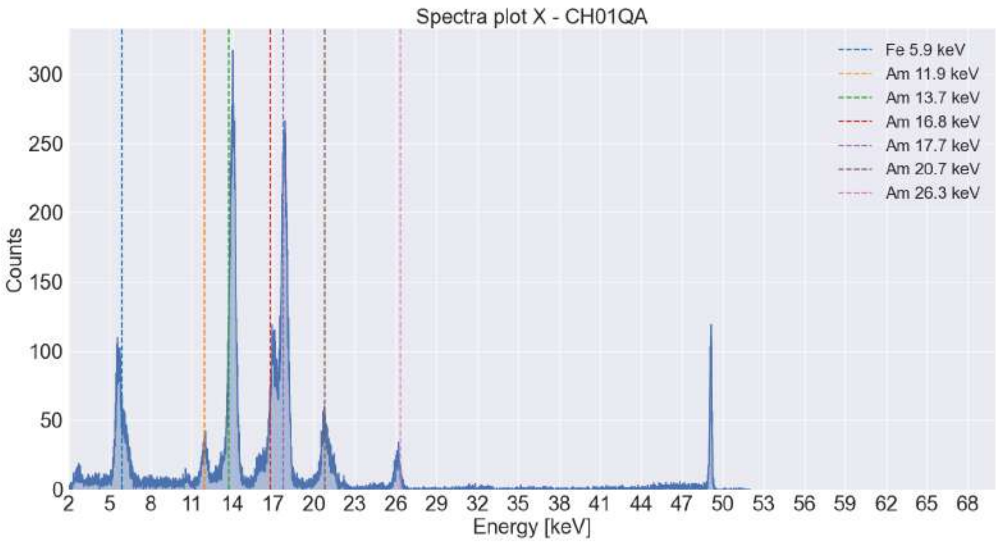

Figure 5.8: Calibrated spectrum of the joined spectra of Am-241 and Fe-55 (5.9, 11.9, 13.7, 16.8, 17.7, 20.7, 26.3 keV) in the X branch of Ch.3, with counts and Energy (keV). Dotted lines represent the real, tabulated energy of each emission line.

Emission line (keV)	Centroid (ADU)	FWHM (ADU)	Amplitude (counts)
(1)	(2)	(3)	(4)
Fe 5.9	9814 ± 4	283 ± 11	28022 ± 931
Am 11.9	12564 ± 4	238 ± 12	7819 ± 325
Am 13.7	13458 ± 1	228 ± 3	67332 ± 855
Am 16.8	14771 ± 4	296 ± 19	33122 ± 1786
Am 17.7	15103 ± 1	244 ± 4	64824 ± 839
Am 20.7	16413 ± 5	326 ± 13	16028 ± 527
Am 26.3	18726 ± 4	230 ± 13	5798 ± 258

Table 5.4: Results of Gaussian fit 5 lines of Am-241 (13.7 keV, 17.7 keV,20.7 keV, 26.3 keV) and Fe-55 (5.9 keV). The columns are: (1) the energy of the line; (2) the centroid of the line from the fit in ADU; (3) the FWHM of the line in ADU; (4) the amplitude of the line from the fit in counts. Errors are 1σ. Fit for Ch.3.

5.4.1.2 Energy Resolution

Once the energy calibration is done, following the procedure explained in Section 4.4.1, the energy resolution for example for the line at 13.7 keV is evaluated. We list our results in Table 5.5.

Channel	FWHM (ADU)	FWHM (e^-)	FWHM (eV)
Ch.0	186 ± 2	119 ± 14	434 ± 50
Ch.1	211 ± 3	122 ± 14	446 ± 50
Ch.2	210 ± 3	122 ± 14	444 ± 50
Ch.3	228 ± 4	125 ± 16	458 ± 57

Table 5.5: Table with the calculated FWHM for the line at 13.7 keV for every channel in X branch of ORION IV. In the Table the FWHM is reported in ADC units, in electrons and in keV.

5.4.1.3 Linearity

We the linearity of each channel with the same procedure described in Section 4.4.2. The results are shown in Figure 5.9 for Ch.0 and in Table 5.6 for all channels.

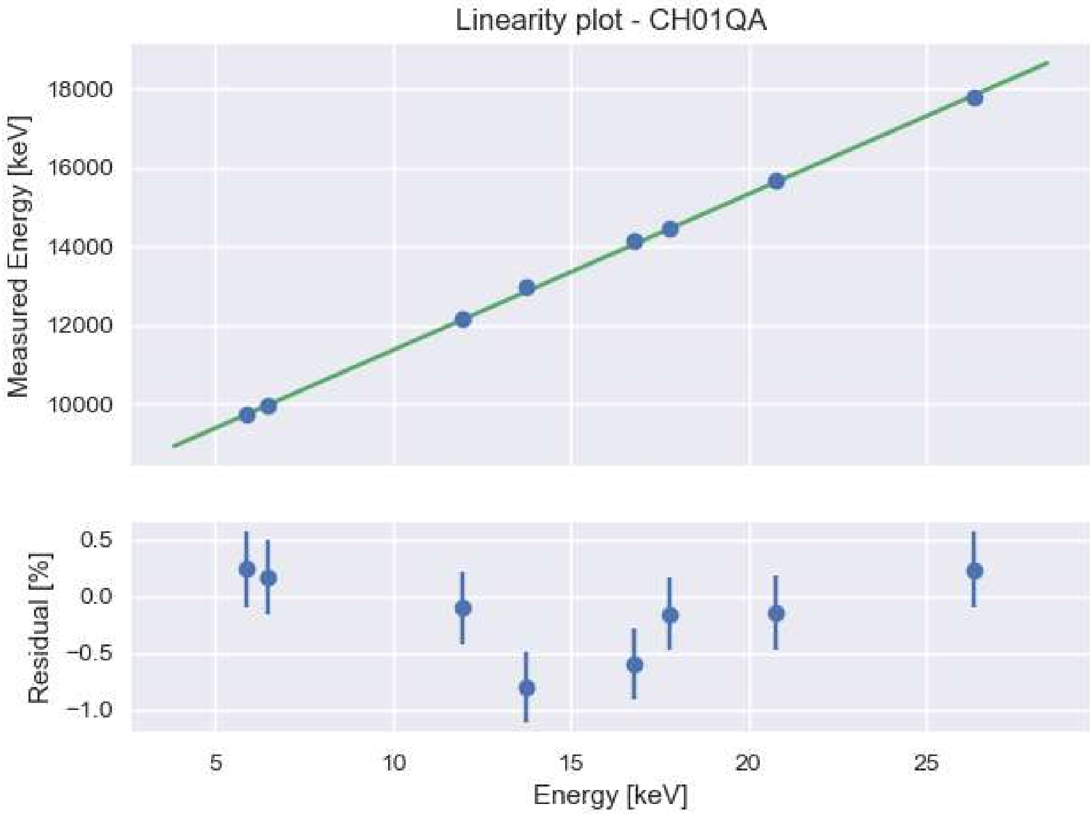

Figure 5.9: Upper panel: Linearity fit of the centroids of the Am-241, Fe-55 spectrum in the X branch of Ch.0. Lower: Residuals in percentage of the energy value.

Channel	Gain (ADU/keV)	Offset (ADU)	Pearson Correlation Coefficient
Ch.0	397 ± 2	7400 ± 31	0.9989
Ch.1	426 ± 3	7787 ± 64	0.9976
Ch.2	427 ± 4	7899 ± 78	0.9966
Ch.3	436 ± 5	7340 ± 93	0.9888

Table 5.6: Gain, Offset and Pearson correlation coefficient obtained from the fit of Am-241 and Fe-55 from software `MESCAL` for every channel of ORION IV.

5.4.2 γ Bottom Branch

We characterized the γ bottom branch following the same procedure as with the X branch.

5.4.2.1 Energy calibration

Due to time constraints, we were able to calibrate only Channel 0. Figure 5.10 and 5.11 show the calibrated spectra and linearity fit for Ch.0 γ-bottom branch. Due to the different shaping of the gamma branch the resolution is worse than in the X branch, so that the Am-241 lines at 17 and 20 keV cannot be resolved, their weighted blend is anyway used.

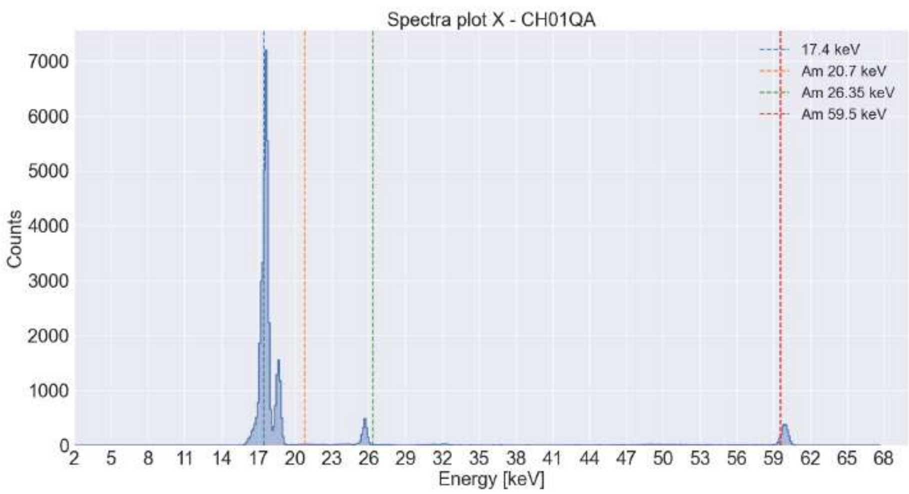

Figure 5.10: Calibrated spectrum of the spectrum of Am-241 (17.4, 20.7, 26.3, 59.5 keV) in the γ-Bottom branch of Ch.0, with counts and Energy (keV). Dotted lines represent the real, tabulated energy of each emission line.

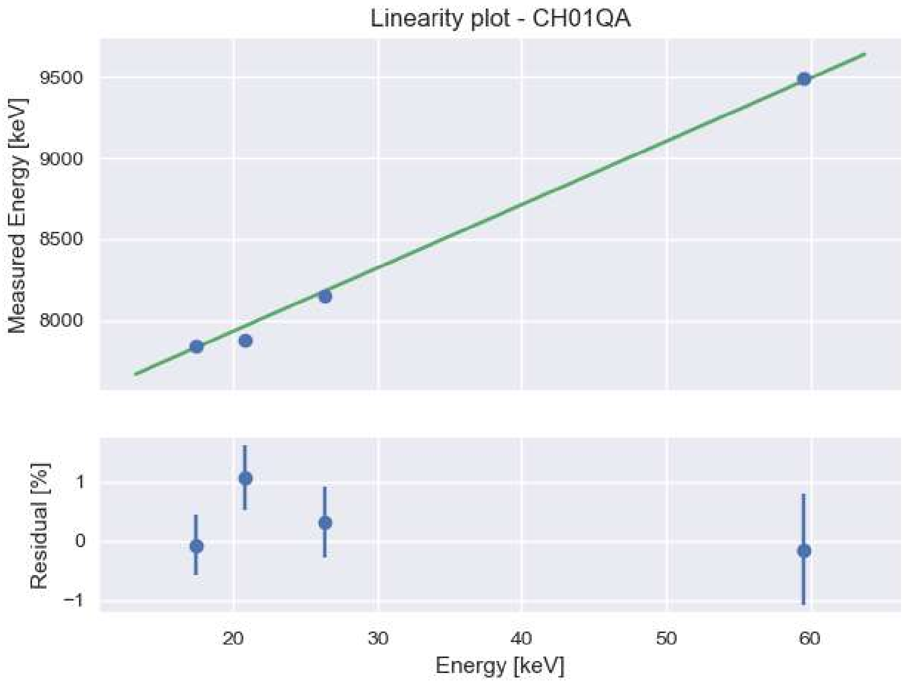

Figure 5.11: Upper panel: Linearity fit of the centroids of the Am-241 spectrum in the γ-Bottom branch of Ch.0. Plotted measured energy (calculated with gain and offset) against energy tabulated. Lower: Lower: Residuals in percentage of the energy value.

5.4.2.2 Linearity

To verify the ADC linearity over the operative range, we employed electrical test pulse of different amplitudes to mimick the signal from scintillation.

We selected 7 impulses in the dynamical range of the γ branch: 150, 200, 300, 450, 600, 700, and 750 mV, collecting the spectra as shown in Figure 5.12 and 5.13 for Ch.0. We report in Table 5.7 the test result of all the channels with the Gain, Offset, and Pearson correlation coefficient.

5.4.3 Capacitance Test CH.0

The aim of this test is to verify ORION IV internal capacitance and the electrical noise of the test board found in the characterization of Mele et al. (2021) and in Grassi et al. (2022).

This test was done on the Ch.0 following a procedure similar to the one illustrated before

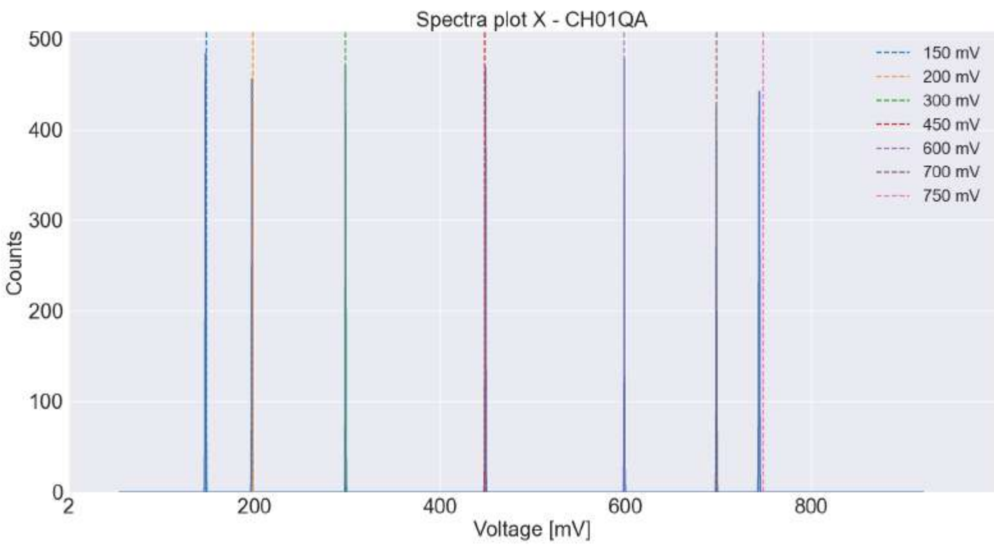

Figure 5.12: Calibrated spectrum of the impulses (150, 200, 300, 450, 600, 700, 750 mV) in the γ-Bottom branch of Ch.0, with counts and Voltage (mV). Dotted lines represent the real, tabulated voltage of each line.

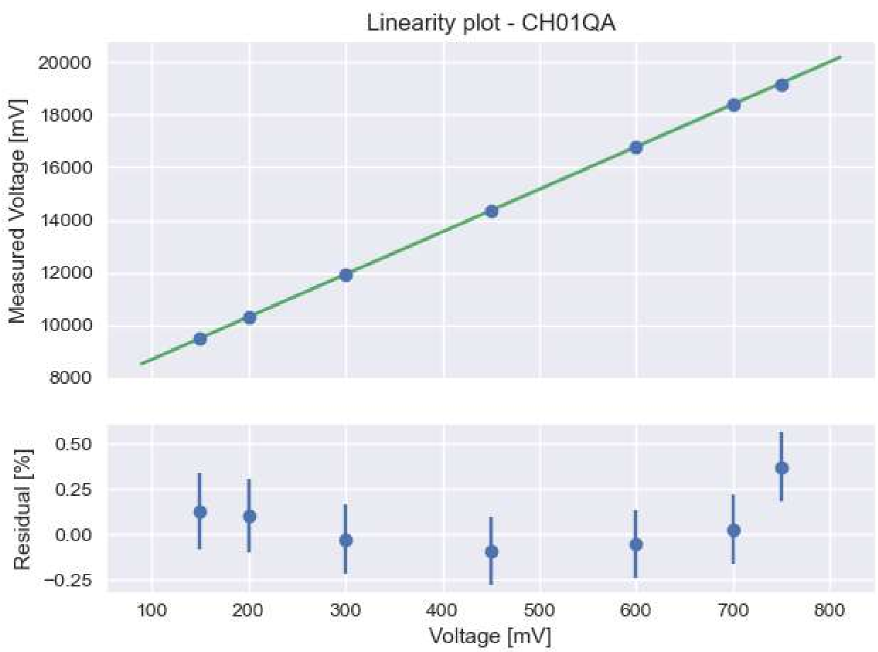

Figure 5.13: Upper panel: Linearity fit of the centroids of the impulses in the γ-Bottom branch of Ch.0. Plotted measured voltage (calculated with gain and offset) against voltage tabulated. Lower: Lower: Residuals in percentage of the energy value.

(Section 4.4.5).

Channel	Gain (ADC/mV)	Offset (ADU)	PCC
Ch.0	16.16 ± 0.04	7083 ± 19	0.99995
Ch.1	14.58 ± 0.06	7033 ± 44	0.99970
Ch.2	16.32 ± 0.06	7520 ± 33	0.99989
Ch.3	14.20 ± 0.04	6727 ± 21	0.99994

Table 5.7: Gain, Offset and Pearson correlation coefficient for every channel in ORION IV.

5.4.3.1 Test Capacitance Evaluation X branch

Following the procedure indicated in Section 4.4.5, we selected three pulses amplitudes (see Figure 5.14), i.e. 50, 70, 100 mV.

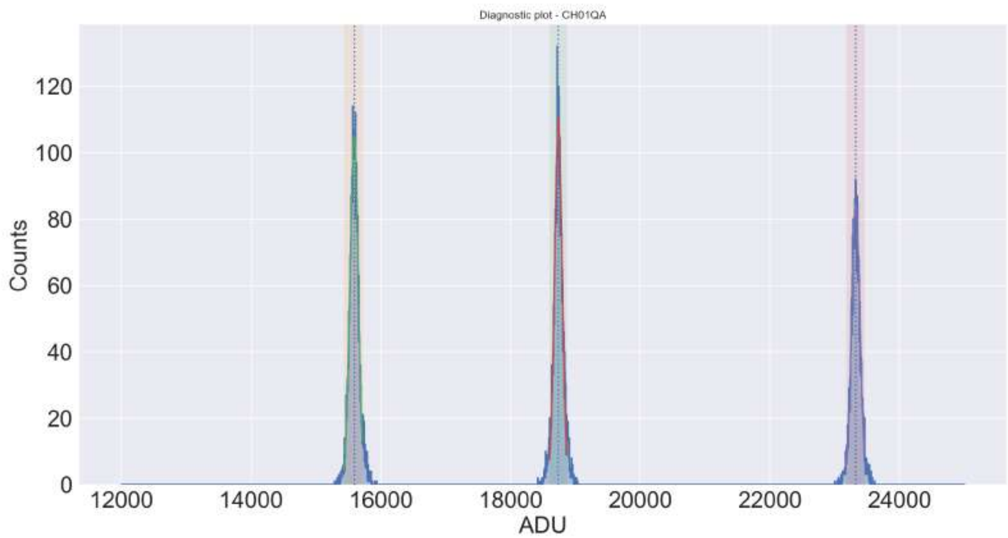

Figure 5.14: Fit of the 3 impulses (50, 70, 100 mV) in the X branch of Ch.0, with counts and ADC channels (expressed in ADU, analog to digital unit). The shaded, colored areas represent the ranges at which the software detected a feature. The solid, colored lines represent the resulting best fit of these features, obtained by the least-squares fitting of a Gaussian profile. The dotted lines represent the mean of these fitted functions.

In Table 5.8 we report the fit of the three lines we will use for the calculation of the capacitance.

With the gain and offset, we can convert the signal from mV to energy; the results are reported in Table 5.8.

Pulser line (mV)	Centroid (ADC)	FWHM (ADU)	Amplitude (counts)
50	15589 ± 1	147.8 ± 3.7	16503 ± 341
70	18737 ± 2	137.1 ± 4.7	16106 ± 455
100	23322 ± 2	148 ± 5	13348 ± 367

Table 5.8: Results from the Gaussian fit 3 impulses (50, 70, 100 mV) from the Software `MESCAL`. The columns are: first show the voltage of the line; the second present the centroid of the line from the fit in ADU; in the third is tabulated the FWHM of the line in ADU; in fourth is presented the amplitude of the line from the fit in counts. Errors are 1σ.

In Table 5.9 we present the calculation of the capacitance for the X-branch.

Energy Charge (keV)	Voltage (V)	Charge (e^-)	Charge (C)	Capacitance (fF)
20.6	0.05	5635 ± 44	$9.01 \pm 0.07 \cdot 10^{-16}$	18.0 ± 0.1
28.6	0.07	7849 ± 41	$1.26 \pm 0.01 \cdot 10^{-15}$	17.9 ± 0.1
40.4	0.1	11075 ± 44	$1.77 \pm 0.01 \cdot 10^{-15}$	17.7 ± 0.1

Table 5.9: Table with the result for the calculation of the capacitance. This table shows: equivalent energy, voltage, charge in Coulomb, and charge in electron, and capacitance calculated for every impulse. For every value, it has been calculated the σ.

We derived the test capacitance value of Ch.0 of 18 fF, which is comparable with the value defined by the ASIC designer (Bertuccio et al. 2021b) and (Bertuccio et al. 2021a).

5.4.3.2 Electric noise Calculation X branch

Following the procedure reported in Section 4.4.4, we proceeded with the calculation of the electronic noise for the X branch. The results are shown in Table 5.10.
The electronic r.m.s of ORION IV is comparable with a value of $\sim$ 43 e^-.

5.4.3.3 Test Capacitance Evaluation γ branch

We performed the same calculation for the γ branch to have a double check from the value gained in Section 5.4.3.1.

Line energy (keV)	σ_{tot} (e^-)	σ_{Poisson} (e^-)	σ_{el} (e^-)
(1)	(2)	(3)	(4)
20.6	44.2	7.5	43.5
28.6	40.9	8.5	40.0
40.4	44.3	10.5	43.1

Table 5.10: Results from the calculation of the electronic noise. In column (1) we report the equivalent energy of the line; in column (2) the total noise of the lines; in column (3) Poissonial noise; in column (4) the electrical noise.

In Table 5.11 we present the calculation of the capacitance for the γ-branch.
The calculated capacitance for the γ-bottom is $\sim$ 18 fF, is consistent with the value calculated in the X branch. This compatibility is expected since the test capacitance resides in the ORION FE and remains independent of the X or γ chain.

Energy Charge (keV)	Voltage (V)	Charge (e^-)	Charge (C)	Capacitance (fF)
122.4	0.30	33524 ± 41	$5.36 \pm 0.01 \cdot 10^{-15}$	17.88 ± 0.02
184.6	0.45	50574 ± 44	$8.09 \pm 0.01 \cdot 10^{-15}$	17.98 ± 0.01
246.4	0.60	67527 ± 44	$1.079 \pm 0.001 \cdot 10^{-14}$	18.00 ± 0.01

Table 5.11: Results from the calculation of the capacitance. In column 1 is present the equivalent energy, in column 2 the change in electron, in column 3 the charge in Coulomb, in column 4-5 the voltage and capacitance and their respective errors, were derived for every impulse. Errros are 1σ

Conclusions

The gamma-ray sky is populated by highly energetic transient events called Gamma-Ray Bursts (GRBs). GRBs are short flashes of gamma-rays, that last between 0.01 and 100 seconds. It is impossible to predict when and from where they will arrive. Their emission is shows a prompt phase, characterized by an emission mostly in the gamma-ray band, and a lower energy afterglow, that last from hours up to weeks. Since their discovery in the 1960s by the Vela satellites, the study of these sources has been closely related to the history of gamma-ray missions. The Italian/Dutch mission Beppo-SAX set the standard for detecting GRBs it comprised: a γ-ray monitor, along with lower energy detectors and the capability of repointing, in order to detect the source at high energies and then follow up the afterglow. This allowed for the first identification of the host galaxy of a GRB. The still ongoing Swift mission improved this concept, by implementing a much faster repointing capability (8/6 hours of SAX vs 70 seconds of Swift). Nowadays, thanks to the follow-up capabilities of Fermi, INTEGRAL and Swift, GRBs have also been linked to the electromagnetic counterparts of gravitational wave events, after the detection of GW170817.

The *Transient High-Energy Sky and Early Universe Surveyor* (THESEUS) is a proposed space mission developed by a large European collaboration and submitted in 2016 to ESA, for the M5 call within the Cosmic Vision Program. In 2018, THESEUS, along with other two mission concepts, it was chosen by ESA for a 3-year Phase A assessment study, but in the end was not selected. Nevertheless, THESEUS was proposed again to the ESA M7 call, successfully concluding the preliminary phase 0 and undergoing the CDF (Concurrent Design Facility) analysis. Currently, THESEUS is awaiting the ESA decision regarding its admission into the subsequent selection phases. THESEUS will present a wide sky monitoring, encompassing an extended energy range (0.3 keV–10 MeV) while highlighting focusing capabilities in the soft X-ray band. With a formidable grasp and angular resolution, THESEUS incorporates on-board near-IR capabilities to follow-up infrared observations aimed at determining the GRB redshifts. It boasts a remarkable degree of spacecraft autonomy and agility, with the capability of promptly transmitting transient trigger information to ground stations. The instrumental ensemble on THESEUS comprises the XGIS (X-Gamma rays Imaging Spectrometer), a duo of coded-mask monitoring cameras equipped with monolithic SDD (Silicon Drift Device) and CsI(Tl), X-ray and gamma-ray detectors. These instruments are purpose-built for detecting GRBs, with imaging capabilities up to 150 keV and precise spectroscopy up to 10 MeV. Additionally, the SXI (Soft X-ray Imager), a twin lobster eye monitor, conducts follow-up observations in the soft X-rays after XGIS detections. Lastly, the IRT (InfraRed Telescope) presents both imaging and spectroscopy capabilities dedicated to the follow-up in infrared waveband investigations and the discernment of GRB redshifts. My thesis is focused on the characterization of the first prototypes of the ORION ASIC (Application specific integrated circuit), a multi-chip readout circuit designed for XGIS. In particular, my work deals with the characterization of two detectors prototypes with ORION, to test if they are compliant with the official requirements. These specifications, intricately tailored to amplify and optimize the scientific output of the XGIS detector, are closely related with the scientific objectives at the heart of the THESEUS mission. The present work was carried out at the INAF Observatory for Astrophysics and Space Science in Bologna (OAS-Bologna).

This thesis follows the works started by Mele et al. (2021) and Grassi et al. (2022). In these works, the first prototype of ORION was tested in two different configurations which did not include all the components of the acquisition chain (see Figure 5.15, upper panel). We proceeded to test a prototype of ORION with the full acquisition chain, including an SDD. Furthermore, we also tested the newly developed ORION IV, which implements four channels instead of only one (see Figure 5.15, lower panel). This was the first time this prototype was ever tested.

The first part of my work addresses the experimental tests on the test board with ORION I, a single channel version of the ASIC, and a SDD (Chapter 4). The SDD anode is connected to a front-end chipset, composed of two different ASICs: the ORION-FE, which reads and processes the signal from SDD acting as a preamplifier, signal shaper and transmitter, and the ORION-BE ASIC, used to read and process the output of a ORION-FE, and including a discriminator, a peak stretching circuit, a smart logic and a analog to digital converter (ADC). The first prototype is a board with a SDD and

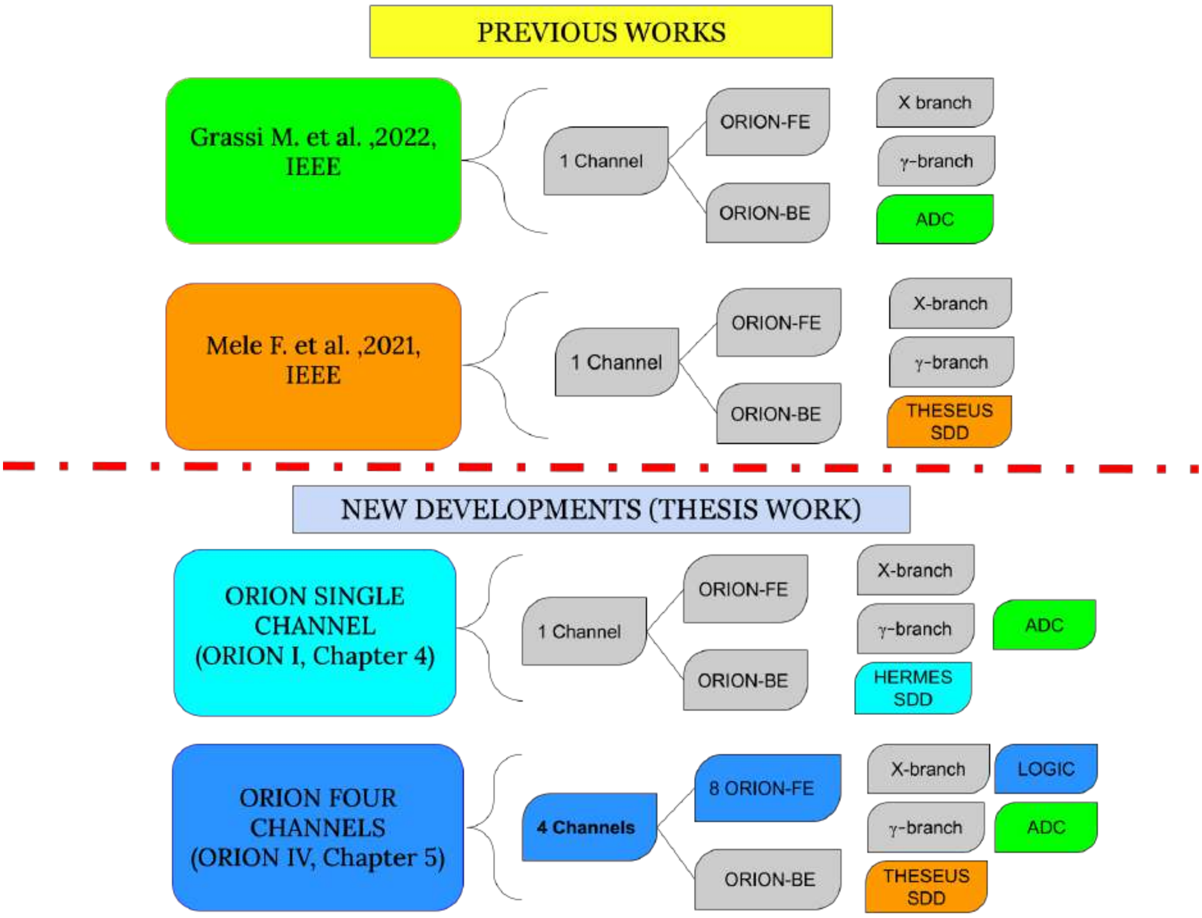

Figure 5.15: Schematic diagram of tests performed on prototypes of ORION and XGIS design. The gray blocks represent shared components across all the tested configurations. The color code indicates the components that differ between different experiments. In the upper panel, we show the tests published in the literature for ORION I. In the lower panel, we show the tests performed in this thesis, both for ORION I and ORION IV.

the complete ORION I electronics. To this aim, we first developed a new acquisition software in LabView (see Appendix D), and an adaptation of the `MESCAL` software for data analysis (see Appendix E). We characterized ORION I by performing:

- functionality tests on both shaper and stretcher, to observe the ability of the ASIC to shape and digitise a X or γ signal;
- dynamic range, to verify the operative range of the detector;
- threshold dependence on the gain, to observe if there is a relation between the gain of the ASIC and the discriminator threshold;

- energy resolution, to characterize the energy resolution of the detector;
- linearity, to confirm that the output of the ASIC is proportional to the given input, within the operative range;
- test capacitance, to validate the design capacitance test;
- electronic noise, needed to calculate the electronic noise of the ASIC;
- performance under different temperatures, to observe the behaviour of the detector under the different temperatures and characterize the variation of performance.

In particular, we noticed that the dynamic range (4.1–141.4 keV) and linearity (99%) are within requirements and are compatible with those reported in literature (Grassi et al. 2022; Mele et al. 2021). However, we also noticed that the electronic noise and energy resolution ($\sigma_{\mathrm{el}} \sim 117.4$ e$^-$ and 1080 eV at 13.7 keV, respectively) are worse than what is required (15 e$^-$ and 300 eV at 6 keV), while the capacitance is lower (8 fF).
In the second part of my thesis, we characterized the the ORION IV prototype, with 4 complete channels in the final configuration designed for XGIS, with 8 FE and 1 BE, connected to an SDD. Moreover, the implemented SDD is an adaptation of the final version for the XGIS SDD. Following the procedure implemented for the first prototype, we performed:

- functionality on both shaper and stretcher;
- dynamic range;
- energy resolution;
- linearity;
- test capacitance;
- electronic noise.

We noticed that the operative range of ORION IV ($\sim$1.4–40 keV) and linearity (99%) are within requirements and in line with those in literature. These values are in line with the literature (Grassi et al. 2022; Mele et al. 2021). The electronic noise and the energy resolution (40 e$^-$ and 434 eV at 13.7 keV, respectively) are higher than what is required

(15 e^- and 300 eV at 6 keV), while the capacitance is lower (18 fF), although they are all values better than those of ORION I.
In Table 5.12, we show the main results of this thesis: the performance results for each of the two prototypes we tested, and the corresponding requirements as mandated by ESA.
The next steps will be a complete characterization of the prototype ORION IV, with the addition of the scintillators to complete the detector, and the environmental tests. Being the first multi-channel prototype, its complete characterisation requires a thorough knowledge of the logic and understanding of how the different channels interact. We expect the 4 channels to operate in parallel without blocking each other's activity but there could be cross-talk problems in the BE that we are not aware of. The implementation of a crystal, instead, requires the use of a silicon layer and then a recalibration of the whole gamma branch. We expect the characterisation to proceed without any hardware problems. ORION IV is bringing many innovations, and its performance is surprising in terms of the progress made in the space of a single prototype.

THESEUS is currently under review within the M7 ESA call. All the results achieved by this thesis will provide as a feedback to the ASIC design team and will hopefully allow an improvement in future versions of the XGIS detector. The experience provided by the development of this front-end electronics for the XGIS instrument; will also facilitate the implementation of the siswich concept for future missions drawing inspiration from the HERMES and THESEUS/XGIS instrument, one can envision CubeSat expeditions dedicated to planetary surface spectroscopy (such as the ongoing ASI TASTE mission in Phase A), or upgraded detectors for capturing high-energy phenomena, thus bridging the gap between theoretical and experimental research.

General

	Requirements	ORION I	ORION IV
Discrimination (X/γ)	✓	✓	To Be Done
Shaping capability	✓	✓	✓
Stretching capability	✓	✓	✓
Temperature Range	[-20 °C; 20°C]	[0 °C; 20°C]	-
Internal Capacity(fF)	20	8.1	18

X-processor

	Requirements	ORION I	ORION IV
Dynamic Range	545–10000 e^- (2–30 keV)	450–15500 e^- (4.1–141.4 keV)	338–9788 e^-(1.4–40 keV)
Linearity	99%	99% (5.9–26.3 keV)	99% (in 5.9–26.3 keV)
Energy Resolution	300 eV (at 6 keV EoL)	1080 eV (at 13.7 keV, 20°)	434 eV (at 13.7 keV 20°C)
ENC (rms)	15 e^-	~111 e^-	~ 40 e^-

γ-processor

	Requirements	ORION I	ORION IV
Dynamic Range	90000 e^- (7.2 MeV)	Top 500 – 150000 e^- (40 keV – 12 MeV) Bottom -	Top 136000 e^-(27 keV – 10.9 MeV) Bottom 338 – 127000 e^- (27 keV – 10.2 MeV)
Linearity	99%	Top 98% Bottom -	Top - Bottom 99.5%

Table 5.12: Table with the results from the tests on ORION I and ORION IV. In the first column is listed the test performed. In second column are showed the requirement from ESA. In third column are presented the results for the prototype ORION I. In fourth column are exhibited the results for the prototype ORION IV. The rows are divided in general test for both X and γ branch, X processor and γ processor. In yellow is not a requirement but a verification with the value of the design.

Appendix A

Coded Mask

Coded masks are widely used in radiation imaging methods to detect and locate radioactive events as an improvement of the collimators. A coded mask is a patterned mask with a specific arrangement of openings or codes. When radiation passes through the mask, it creates a unique pattern on the detector, allowing for the identification and localization of the source.
The working principle of the coded mask is shown in Figure A.1.

The coded-aperture was firstly developed from a scatter-hole cameras for X-rays and γ-rays. The introduction of a multi-hole mask enhances the signal-to-noise ratio (S/N) while preserving excellent angular resolution in small-diameter, single-hole imaging devices Dicke (1968). Mathematically, masks are represented as binary arrays, where ones correspond to pinholes and zeros represent opaque elements within the aperture. In the early work on coded-apertures, pinholes were randomly distributed on the mask and placed in front of a source to be analysed. The source casts multiple overlapping shadows on the detector through the mask. Fourier convolution theorem is then used to reconstruct a single, high-resolution image from the photons counted on the detector plane Ables (1968). If the distribution of the transparent and opaque elements of the aperture can be represented as a binary encoding array A and the decoding array as G, then A and G can be chosen such that the reconstructed image (correlation of A and G with addition of some noise signal N) approximates a delta function. Delta function is represented by a single impulse located at the central point in signal analysis. In radiation detectors, the impulse indicates the location of the reconstructed source (Poularikas, 2006).

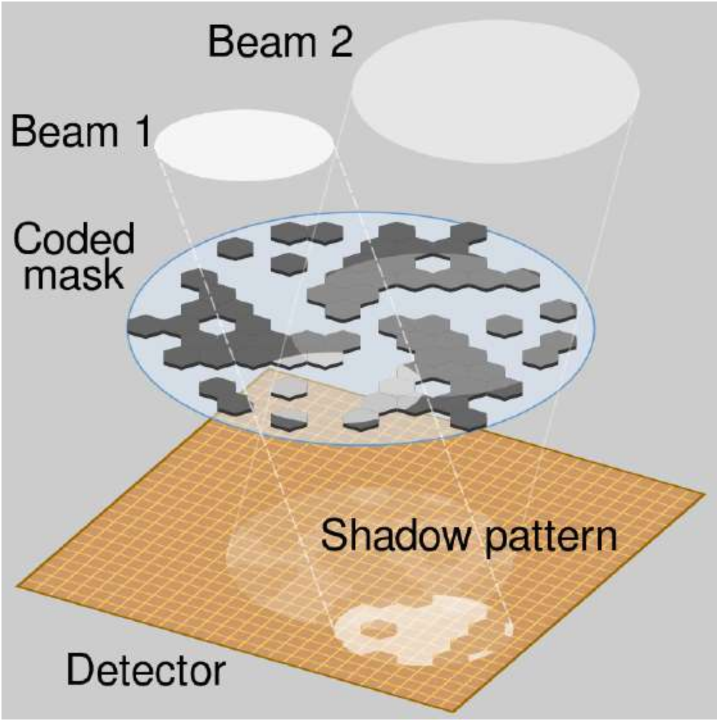

Figure A.1: Simplified principle of operation of a HURA hexagonal coded aperture mask used in the SPI instrument of the INTEGRAL space telescope by CMG Lee[1].

As the dimensions of the aperture elements are kept small, the overall size of the aperture may also be small and reduce the field of view (FOV) of the device. However, multiple devices can be built (in e.g. 2×2 configuration), which will compensate for FOV reduction at the cost of a larger number of signals required to be processed on the output. This may, in turn, affect the detection speed as signals from the position sensitive detector require decoding to localise the source of radiation in the coded-aperture imaging systems Cieślak et al. (2016).

[1] https://commons.wikimedia.org/wiki/File:HURA_hexagonal_coded_aperture_mask_principle.svg

Appendix B

Anticoincidence shielding

In the case of a particle-emitting source detected by detectors 1 and 2, the signals from the detectors are directed to a timing circuit, which generates a pulse indicating the occurrence time of the corresponding event in either detector (1) or (2). These timing signals are then fed into a coincidence unit designed to produce an output signal only when both timing pulses coincide (Tsoulfanidis & Landsberger 2021). The principle of anticoincidence shielding dictates that if both detectors receive a pulse outside a certain small time interval of each other, the output signal generated by the detector is blocked and not registered Gilmore (2008). Anticoincidence shielding is also used to suppress the Compton continuum in the recorded spectrum, because a Compton-scattered gamma ray from the primary detector may also interact within the surrounding detector. Highly penetrating cosmic radiations are eliminated through the use of an anticoincidence shield or guard counter. The primary detector is surrounded by a second detector (or an array of detectors), and the output of the primary detector is accepted only when it is not accompanied by a coincident pulse in the outer detector. The source to be counted is oriented and shielded so that it produces interactions only in the primary detector. Therefore, no pulses are affected that correspond to the complete absorption of the source radiation within the primary detector Knoll (2010). The anticoincidence shield on the instrument EGRET is shown in Image B.1.

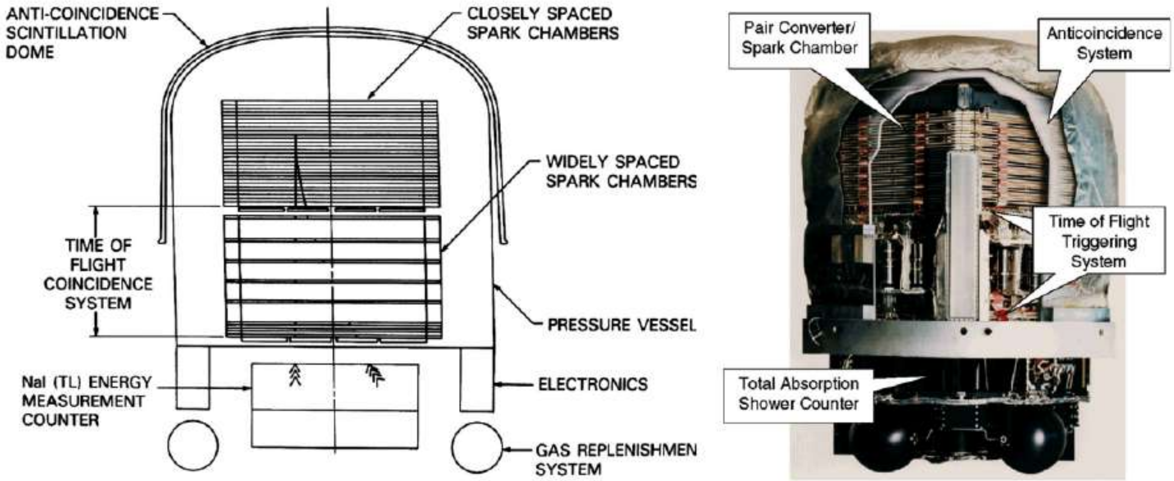

Figure B.1: Left: schematic diagram of EGRET onboard CGRO. Right: composite photo of EGRET, showing the various components, spark chambers, anticoincidence shield, triggering system and total absorbtion shower counter. Image taken from Thompson (2015).

Appendix C

Wolter Mirrors

Focusing systems for soft X-ray energies are based on the external reflection of photons incident, at small grazing' angles of incidence less than some critical angle (θc), which depends on the composition of the reflecting material and decreases with increasing X-ray energy. A paraboloid mirror is the simplest focusing element. The image of a point X-ray source at infinity is a circle in the focal plane, whose radius is proportional to the off-axis angle. The paraboloid can not be used to form an image; but it can be used as a flux concentrator of the source. The Wolter mirrors, called after Hans Wolter, who in 1952 described this type of optics (Wolter 1952), consist of a parabolic mirror followed by a hyperbolic mirror.

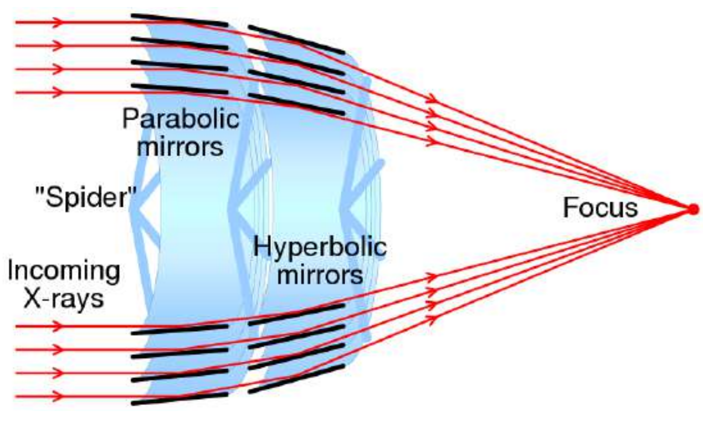

Figure C.1: Diagram of the Wolter mirrors nested in the Chandra telescope, with an X-ray incident in the parabolic and hyperbolic mirrors. Image by CMG Lee[2].

[2]https://commons.wikimedia.org/wiki/File:Xray_telescope_lens.svg

The paraboloid and hyperboloid are confocal.The utilization of Wolter's Type I configuration, combining double grazing incidence with a paraboloid and hyperboloid, enables the effective focusing of photons onto the detector plane while achieving a reduced focal length compared to using solely a paraboloid or hyperboloid mirror (Fraser 2009).
Wolter optics are widely used in X-ray astronomy, for the observation of sources emitting X-rays, such as neutron star, and active galactic nuclei. Wolter mirrors were used in the Chandra X-ray Observatory, XMM-Newton, Einstein and Swift missions, ROSAT (Röntgensatellit), and eROSITA (extended ROentgen Survey with an Imaging Telescope Array).

Appendix D

Acquisition Software - LabVIEW

The acquisition software developed for ORION I and ORION IV was developed in LabVIEW. LabVIEW is a visual programming language. It allows users to create applications by connecting functional blocks, called virtual instruments (VIs), through a graphical user interface. LabVIEW simplifies data acquisition, analysis, and control systems development.

Our code implements the 'DAQ Assistant', which is a way to control the I/O ports of the NI USB 6259 acquisition board and its interaction with the Orion ASIC. As first operation the ORION ASICs requires the setting of its internal register in *ASIC Configuration mode* followed by the *ASIC acquisition mode*.

To fulfil the requirements to configure the ASIC and acquire data from it, the program consists of four main blocks.

Task definition: defines the tasks of the I/O ports of the NI USB 6259 acquisition board.

ASIC Configuration: a block that sets the ASIC registers allowing to define its modes of operation (shaped or stretched), threshold levels, internal trigger and ADC activity. The data are loaded into the Orion-BE register pushing the button 'LOAD'. Figures D.1 show the command panels for this operation and the allowed control of ORION I and ORION IV.

ASIC Reset: a block necessary after ASIC configuration to pass in acquisition mode and set the ASIC ready for data acquisition. It is done automatically after the 'LOAD' of register configuration. An image of the software blocks is shown in D.2

Data acquisition and file storage: a block to acquire ASIC data. If the Orion-BE sends an ASIC-Trigger signal (if **Enable Discr** was set to On during configuration), and starts the Internal ADC conversion of the signals, sends the Look At Me (LAM) and data can

Figure D.1: Upper: Screenshot of the configuration panel for ORION I. Lower panel: Screenshot of the configuration panel for ORION IV.

be collected. On LabVIEW we can observe the collection of data from the **User Panel** shown in Figure D.2.

Data are then stored in a file for further analysis. A image of the LabVIEW software used for ORION I is shown in Figure D.3.

An example of the data output from our software is shown in Table D.1.

Internal ADC X	Internal ADC γ Top	NI USB 6259 ADC-X	NI USB 6259 ADC γ Top	NI USB 6259 ADC γ Bottom
...	...	...	...	...
...	...	...	...	...
...	...	...	...	...

Table D.1: An example of the output from the acquisition software with LabView.

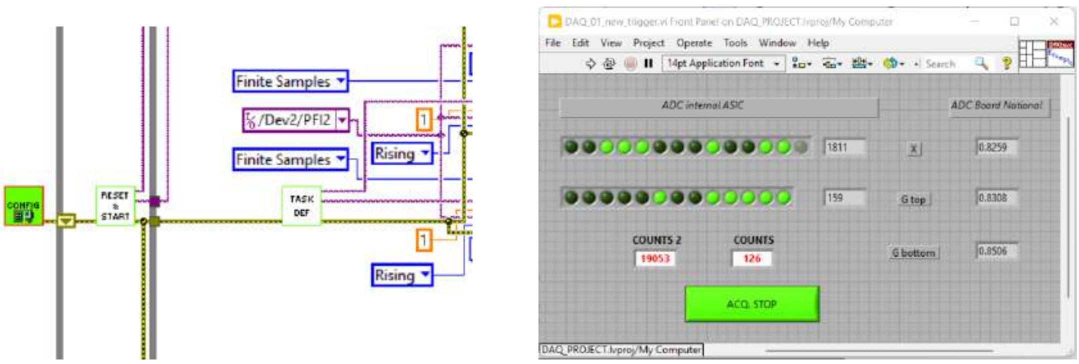

Figure D.2: Left: focus on the LabVIEW blocks of 'Configuration' and 'Reset'. Right: Screenshot of the acquisition data panel, that provides users to monitor the LabVIEW program's functionality, and control over the start and stop of the acquisition process.

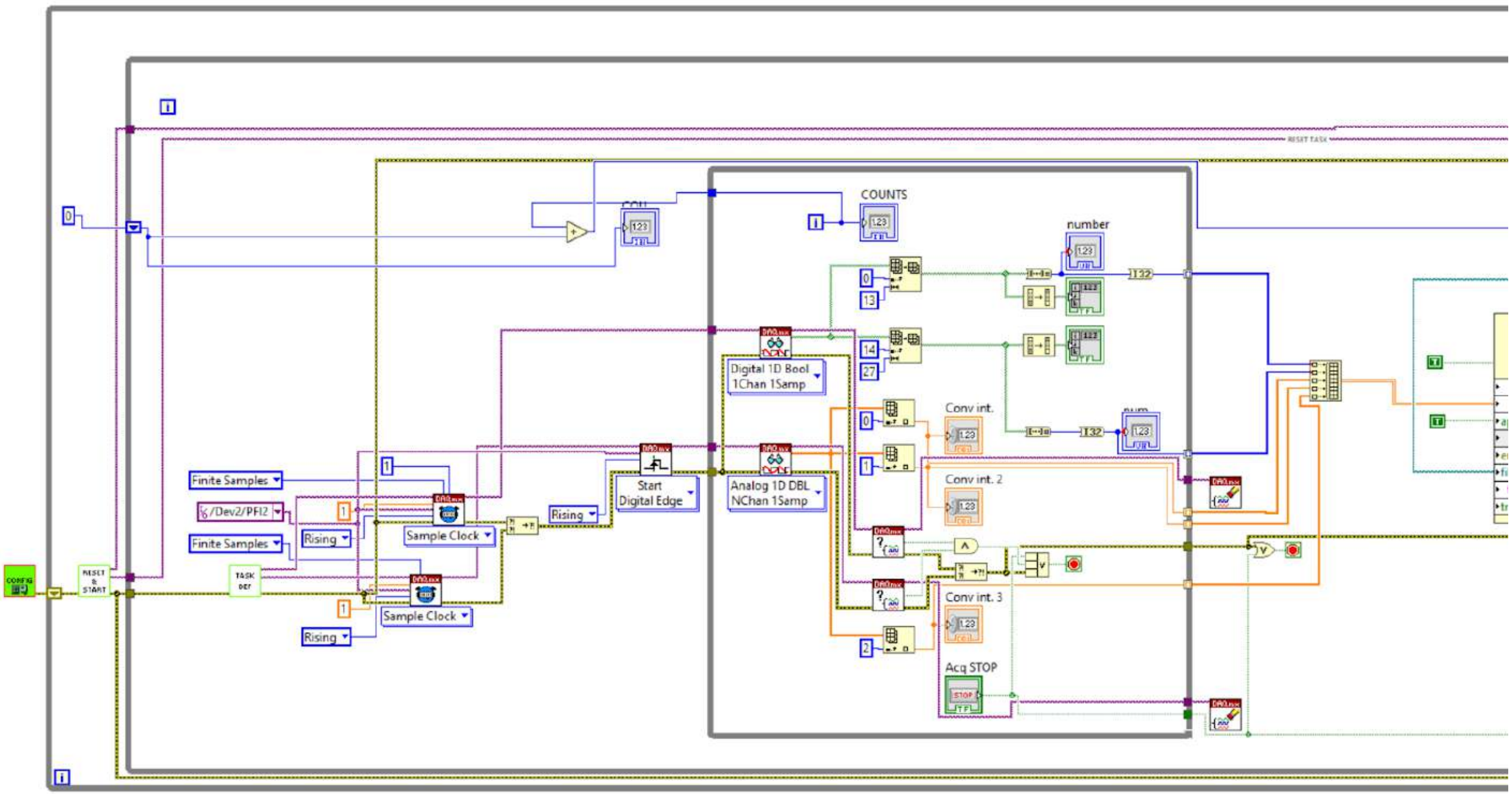

Figure D.3: Screenshot of the LabVIEW program for ORION I where is shown the 5 parallel data output: Internal ADC X data, Internal ADC γ-Top data, External ADC X data, NI external ADC γ-Top data, NI external ADC γ-Bottom data.

Appendix E

Analysis Software- `MESCAL` Pipeline

The `MESCAL` software, initially developed for the HERMES Mission, processes event data obtained from the LYRA ASIC's BE electronics. The pipeline has been modified to accommodate the output word of the ORION ASIC. `MESCAL` utilizes various algorithms, supported by Python packages such as pandas, numpy, and lmfit, to perform tasks like energy calibration, data formatting, and presentation of raw spectra from the HERMES mission.

The primary objective of `MESCAL` is to analyze a large amount of raw data and derive calibration parameters to be stored in the calibration database. The pipeline, implemented in Python 3, requires a FITS Level 0 file as input. Events are stored in a pandas dataframe.

`MESCAL` builds spectrum histograms for event amplitudes per channel and applies a peak detection algorithm to identify local maxima in the histogram. The algorithm selects a set of maxima, defines ranges for each maximum, and performs Gaussian fitting using the `lmfit` package. This fitting process determines the position and width of each emission line, represented by the centroid and FWHM of the Gaussian profile.

Once the main parameters for each emission line are obtained in instrumental units, `MESCAL` proceeds with energy calibration for the X-mode events. The gain and offset parameters are determined using linear least squares fitting of known line energies versus detected peak amplitudes. These calibration parameters are stored as part of the data products generated by `MESCAL`. The S-mode (for γ events) discrimination and calibration is disabled in `MESCAL` due to the fact that in ORION prototypes tested there is no scintillator crystal.

The data products generated by `MESCAL` include data tables, data plots, and event lists.

The data reports contain calibration information and are presented in xsl format, with separate reports for gain and offset (`cal` report) and fitting parameters (`xfit` report). `MESCAL` also produces several plots to visualize detector performance, including uncalibrated raw spectra per channel, diagnostic plots with Gaussian profile fits, linearity plots displaying the best linear fit and residual, and calibrated spectra in energy units.
For the energy calibration of the `MESCAL`, is adopted an algorithm that utilizes user-provided information and peak features. It identifies local maxima in the histogram using the `findpeaks` function from the `scipy` package. A selection process based on normalization, prominence, and width is performed to determine the final list of emission lines. Additionally, `MESCAL` provides a command-line interpreter tool that allows users to access various options for displaying data, diagnostic tools, and exporting data products. The command-line interpreter was developed using Python's `cmd` module, and the terminal user interface incorporates the `rich` Python library for formatting console output. The user interface is presented in Image E.1.

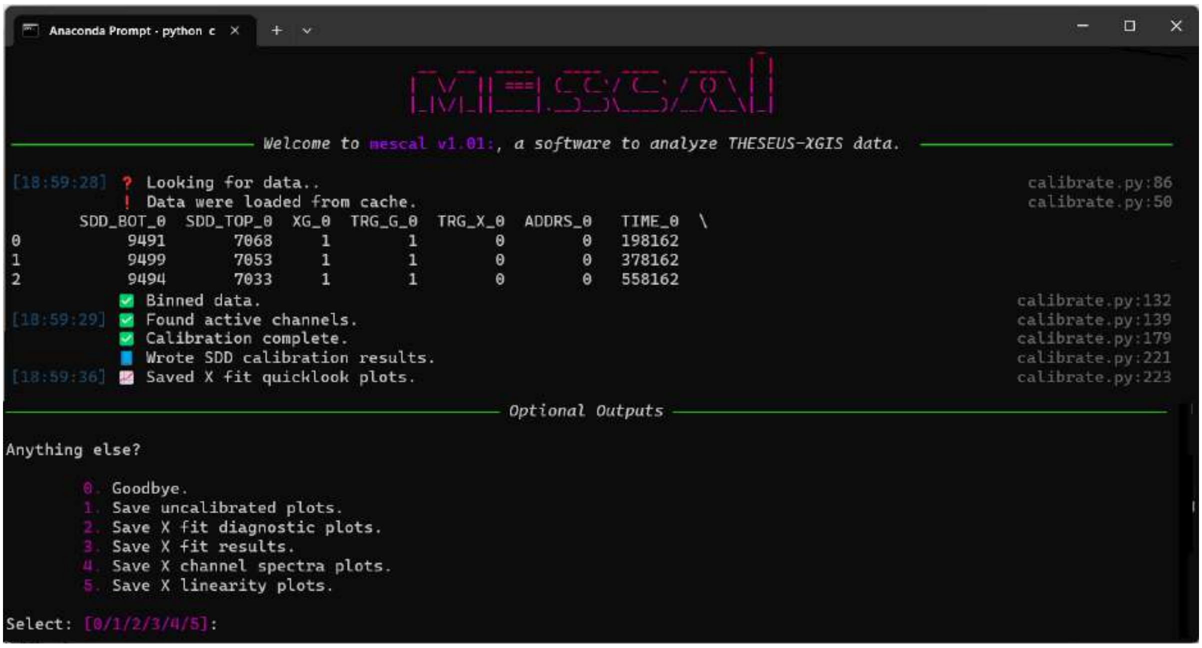

Figure E.1: Image of the user interface of `MESCAL` version for THESEUS-XGIS data.

Appendix F

HERMES Mission

The High Energy Rapid Modular Ensemble of Satellites (HERMES) is a new mission concept that aims to develop a constellation of nano-satellites. It hosts X-ray detectors, characterized by a large energy band (2 keV to 2 MeV) and excellent temporal resolution, and thus optimized for the monitoring of Cosmic High Energy transients such as Gamma Ray BurstsGandola et al. (2019). The main advantages of HERMES are: the modularity and quick development with limited costs. In particular, modularity allows: to fly a reduced versions of HERMES (the HERMES pathfinders) to prove the concept in space; to avoid single (or even multiple) point failures: if one or several units are lost, the constellation and the experiment can still be operative; to fully test the hardware in orbit with the first launches.

The Service Module (SM) selected for the HERMES-TP/SP project is a CubeSat of the 3U class. It offers a volume of 10×10×30 cm and a total mass of the order of 5–6 kg. The HERMES detector is designed to provide a sensitive area >50 cm^2 (Fuschino et al. 2020a).
The energy range of HERMES is from 2 keV to 2 MeV. The detector of HERMES is a scintillator-based detector. The 450 μm thick silicon drift detector is able to detect X-ray radiation with a good efficiency up to 20–30 keV. Detection of hard X-rays/gamma-rays is obtained with a two-stage process that first converts the photon energy into visible light produced by a scintillating material, which is then collected and converted into electric charge in a photodetector. The inorganic scintillator selected for HERMES is the Cerium-doped Gadolinium-Aluminum-Gallium Garnet (GAGG) (Fuschino et al. 2020a,b). An image of the SDD and of the GAGG integrated in the payload is shown in

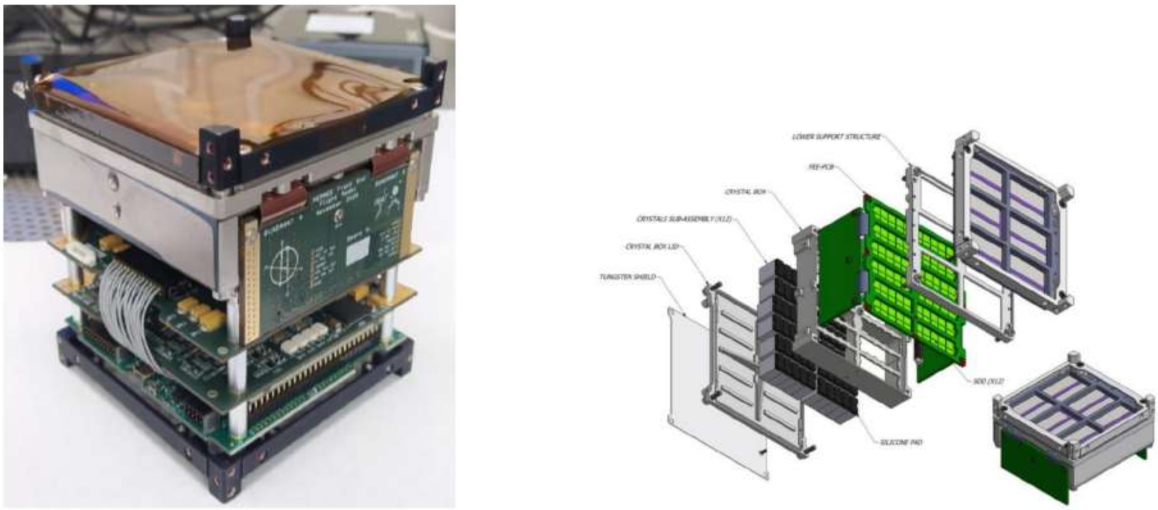

Figure F.1: Left: Image of HERMES FM payload after the integration. Image taken from HERMES[3]. Right: Structure of the X/γ ray detector (Grassi et al. 2020).

image F.2.

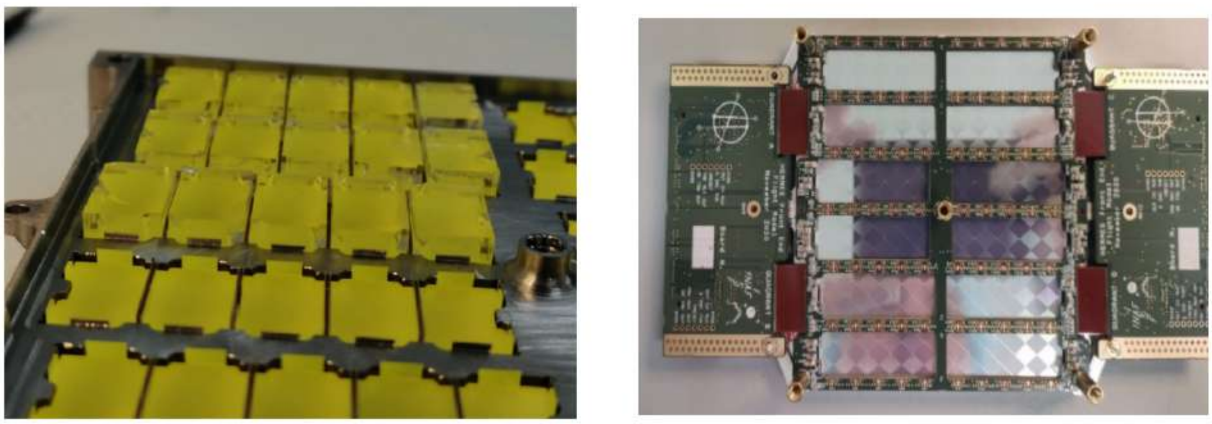

Figure F.2: Left: Image of the box of the scintillator crystal. Contains 60 wrapped GAGG crystals, optical pads are also visible. Right: Image that includes 120 LYRA-FEs, 12 SDD matrix and 4 LYRA-BEs. Images from (Fuschino et al. 2020a).

The exclusion of traditional photomultiplier readout is due to their limited efficiency (∼20% vs. 90% of Si detectors) and larger volume. A great advantage of SDDs compared to SiPM (Silicon Photomultipliers) lies in their ability to also directly detect low-energy X-rays.
To optimize the use of SDDs it's needed a readout electronics that are optimized for the

[3] `https://www.hermes-sp.eu/?p=8848`

low capacity of the charge collection anode. Furthermore, the electronics must be small and with a very low power consumption. These requirements led to the choice of two ASIC (Application Specific Integrated Circuits) as the front-end electronics and back-end electronic. The first one, the LYRA-FE, has the function of charge-sensitive pre-amplifier, directly connected with the SDD on the same board, to fully exploit their low noise (Gandola et al. 2019); the second one, the LYRA-BE, includes all the functions of a spectroscopic chain, and the analog-to-digital converters (ADCs) and a fast discriminator for the timing of the events (Grassi et al. 2020).

The HERMES SDD design is shown in Figure F.2. The nominal thickness of the SDD arrays is 450 μm. The SDD is organized in a 2×5 array. A single crystal ($\sim 2.1 \times 6.94$ mm^2 and 15.0 mm thick) is coupled with two SDD channels on the p-side. On this side, to avoid optical cross-talk coming from different crystals, a metal implant strip 0.5 mm wide is present between adjoining couple of cells. With this configuration, a signal from a single isolated SDD channel will be considered to be originated by the direct absorption of an X-ray in silicon, while a trigger from the two SDD channels coupled to the same crystal will be considered as a γ-ray event given the expected uniform illumination on both SDD cells by the scintillation light.

The energy resolution of HERMES-FEE (Front-End Electronic) is 800 eV at 5.9 keV and 5 keV at 600 keV (Fuschino et al. 2020a; Baroni 2022). The instrumental characteristic of HERMES are listed in Table F.1.

The scientific key goal of the Pathfinders is to prove that accurate localizations (15 arcmin for long bursts and 1 degree for short bursts, Baroni 2022) can be obtained by miniaturized instrumentation on board nano-satellites, using the delays of the arrival time of the signal to detectors positioned at thousands kilometers of distance, and using cross-correlation of the lightcurvers detected by different nanosatellites (Fuschino et al. 2020b). The localisation capability of the whole constellation is directly proportional to the number of components and inversely proportional to the average baseline distance between them (Baroni 2022). Since a minimum number of GRBs shall be detected simultaneously by at least 3 space elements, the main scientific requirements affect the baseline between the satellites and the alignment of their FOVs. At least 3 satellites shall have common FOV, within $\pm 60°$ to maintain 50% efficiency in the detector field, physical baseline between at least 3 co-observing satellites shall be larger than 1000 km.

FoV	3.2 sr FWHM
Energy Range	2 keV-2 MeV
Energy Resolution X	800 eV FWHM (at 5.9 keV)
Energy Resolution γ	5 keV FWHM (at 600 keV)
Angular Resolution	-

Table F.1: Instrumental characteristics of HERMES (Fuschino et al. 2020a).

The novel HERMES architecture enables the implementation of an inexpensive full-sky, accurate monitor, with the possibility of being expanded one module at time.

List of Figures

List of Tables

Bibliography

Abbott, B. P., Abbott, R., Abbott, T. D., et al. 2017, The Astrophysical Journal Letters, 848, L13

Abbott, B. P., Abbott, R., Abbott, T. D., et al. 2017, The Astrophysical Journal, 848, L12

Abdollahi, S., Acero, F., Ackermann, M., et al. 2020, The Astrophysical Journal Supplement, 247, 33

Ables, J. G. 1968, Publications of the Astronomical Society of Australia, 1, 172

Amati, L. 2006, Monthly Notices of the Royal Astronomical Society, 372, 233

Amati, L., Labanti, C., Mereghetti, S., et al. 2022, in Space Telescopes and Instrumentation 2022: Ultraviolet to Gamma Ray, ed. J.-W. A. den Herder, S. Nikzad, & K. Nakazawa, Vol. 12181, International Society for Optics and Photonics (SPIE), 1218126

Amati, L., O'Brien, P., Götz, D., et al. 2018, Advances in Space Research, 62, 191

Angel, J. R. P. 1979, in Space Optics Imaging X-Ray Optics Workshop, ed. M. C. Weisskopf, Vol. 0184, International Society for Optics and Photonics (SPIE), 84 – 85

Ascenzi, S., Oganesyan, G., Branchesi, M., & Ciolfi, R. 2021, Journal of Plasma Physics, 87, 845870102

Atwood, W. B., Abdo, A. A., Ackermann, M., et al. 2009, The Astrophysical Journal, 697, 1071

Band, D., Matteson, J., Ford, L., et al. 1993, The Astrophysical Journal, 413, 281

Baroni, G. 2022, Calibration of the detector flight models for the HERMES and SpIRIT nanosatellite missions.

Barthelmy, S. D., Barbier, L. M., Cummings, J. R., et al. 2005, Space Science Reviews, 120, 143

Barthelmy, S. D., Barbier, L. M., Cummings, J. R., et al. 2005, Space Science Reviews, 120, 143

Barthelmy, S. D., Cline, T. L., & Butterworth, P. 2001, AIP Conference Proceedings, 587, 213

Bertuccio, G., Dedolli, I., Grassi, M., Malcovati, P., & Mele, F. 2021a, Preliminary Measuraments of ORION-V2 ASIC, Tech. Rep. THS-PoliMi-XGIS-TN-0002

Bertuccio, G., Mele, F., Dedolli, I., Malcovati, P., & Grassi, M. 2021b, Preliminary Measuraments of ORION-V1 ASIC, Tech. Rep. THS-PoliMi-XGIS-TN-0002

Bird, A. J., Bazzano, A., Malizia, A., et al. 2016, The Astrophysical Journal Supplement Series, 223, 15

Boella, G., Butler, R. C., Perola, G. C., et al. 1997a, Astronomy & Astrophysics Supplement, 122, 299

Boella, G., Chiappetti, L., Conti, G., et al. 1997b, Astronomy & Astrophysics Supplement, 122, 327

Burrows, D. N., Hill, J. E., Nousek, J. A., et al. 2005, Space Science Reviews, 120, 165

Burrows, D. N., Hill, J. E., Nousek, J. A., et al. 2000, 4140, 64

Böck, H., Gebureck, P., & Stegemann, D. 1975, Nuclear Instruments and Methods, 123, 117

Campana, R., Baroni, G., Della Casa, G., et al. 2022, in Society of Photo-Optical Instrumentation Engineers (SPIE) Conference Series, Vol. 12181, Space Telescopes and Instrumentation 2022: Ultraviolet to Gamma Ray, ed. J.-W. A. den Herder, S. Nikzad, & K. Nakazawa, 121815K

Castoldi, A. & Guazzoni, C. 2012, IEEE Solid-State Circuits Magazine, 4, 46

Cavallo, G. & Rees, M. J. 1978, Monthly Notices of the Royal Astronomical Society, 183, 359

Christian W. Fabjan, H. S. 2020, Particle Physics Reference Library, Volume 2: Detectors for Particles and Radiation, 1st edn. (Gewerbestrasse 11, 6330 Cham, Switzerland: Springer Open Access)

Cieślak, M. J., Gamage, K. A. A., & Glover, R. 2016, Radiation Measurements, 92, 59

Costa, E., Barbanera, L., Feroci, M., et al. 2001, in American Institute of Physics Conference Series, Vol. 599, X-ray Astronomy: Stellar Endpoints, AGN, and the Diffuse X-ray Background, ed. N. E. White, G. Malaguti, & G. G. C. Palumbo, 582–585

Costa, E., Feroci, M., Piro, L., et al. 1997a, IAU Cirulars, 6576, 1

Costa, E., Frontera, F., Heise, J., et al. 1997b, Nature, 387, 783

Dicke, R. H. 1968, The Astrophysical Journal Letters, 153, L101

ECSS, S. 2008, Space engineering Technology readiness level (TRL) guidelines.

Ermis, E. E. & Celiktas, C. 2013, Journal of Radioanalytical and Nuclear Chemistry, 295

ESA/SCI(2021). 2021, THESEUS Transient High-Energy Sky and Early Universe Surveyor Assessment Study Report, 1st edn. (https://sci.esa.int/web/cosmic-vision/-/theseus-assessment-study-report-yellow-book: ESA/SCI)

Esposito, J. A., Bertsch, D. L., Chen, A. W., et al. 1999, The Astrophysical Journal Supplement, 123, 203

Feroci, M. 1999, Mem. Societa Astronomica Italiana, 70, 905

Feroci, M., Costa, E., Soffitta, P., et al. 2007, Nuclear Instruments and Methods in Physics Research A, 581, 728

Fishman, G. & Austin, R. 1977, Nuclear Instruments and Methods, 140, 193

Fishman, G. J., Meegan, C. A., Wilson, R. B., Paciesas, W. S., & Pendleton, G. N. 1992, in NASA Conference Publication, Vol. 3137, NASA Conference Publication, 26–34

Fraser, G. W. 2009, X-ray Detectors in Astronomy (Cambridge Astrophysics), 1st edn.

Frontera, F., Costa, E., dal Fiume, D., et al. 1997a, The high energy instrument PDS on-board the BeppoSAX X–ray astronomy satellite

Frontera, F., Costa, E., dal Fiume, D., et al. 1997b, Astronomy & Astrophysics Supplement, 122, 357

Fuschino, F., Campana, R., Labanti, C., et al. 2021, The XGIS instrument on-board THESEUS: the detection plane and on-board electronics

Fuschino, F., Campana, R., Labanti, C., et al. 2020a, in Society of Photo-Optical Instrumentation Engineers (SPIE) Conference Series, Vol. 11444, Space Telescopes and Instrumentation 2020: Ultraviolet to Gamma Ray, ed. J.-W. A. den Herder, S. Nikzad, & K. Nakazawa, 114441S

Fuschino, F., Campana, R., Labanti, C., et al. 2020b, in Society of Photo-Optical Instrumentation Engineers (SPIE) Conference Series, Vol. 11444, Space Telescopes and Instrumentation 2020: Ultraviolet to Gamma Ray, ed. J.-W. A. den Herder, S. Nikzad, & K. Nakazawa, 114441S

Fuschino, F., Labanti, C., Galli, M., et al. 2008, Nuclear Instruments and Methods in Physics Research A, 588, 17

Gandola, M., Grassi, M., Mele, F., Malcovati, P., & Bertuccio, G. 2019, in 2019 IEEE Nuclear Science Symposium and Medical Imaging Conference (NSS/MIC), 1–3

Gatti, E. & Rehak, P. 1984, Nuclear Instruments and Methods in Physics Research, 225, 608

Gehrels, N., Chincarini, G., Giommi, P., et al. 2004, The Astrophysical Journal, 611, 1005

Gehrels, N., Ramirez-Ruiz, E., & Fox, D. 2009, Annual Review of Astronomy and Astrophysics, 47, 567

Gehrels, N., Ramirez-Ruiz, E., & Fox, D. B. 2009, Annual Review of Astron and Astrophys, 47, 567

Gehrels, N. & Shrader, C. R. 2001, in American Institute of Physics Conference Series, Vol. 587, Gamma 2001: Gamma-Ray Astrophysics, ed. S. Ritz, N. Gehrels, & C. R. Shrader, 3–7

Giacconi, R. 2003, Rev. Mod. Phys., 75, 995

Giacconi R., e. a. 1962, Physical Review Letters, 9

Gilmore, G. R. 2008, Practical Gamma-ray Spectrometry, 2nd edn. (West Sussex PO19 8SQ, England: John Wiley & Sons, Inc.)

G.J. Fishman, e. a. 2013, Gamma-ray Bursts: 15 Years of GRB Afterglows, EAS Publications Series, 61

Grassi, M., Gandola, M., Mele, F., et al. 2020, in 2020 IEEE International Instrumentation and Measurement Technology Conference (I2MTC), 1–6

Grassi, M., Gemelli, A., Malcovati, P., et al. 2022, in 2022 IEEE International Instrumentation and Measurement Technology Conference (I2MTC), 1–6

Hartmann, R., Strüder, L., Kemmer, J., et al. 1997, Nuclear Instruments and Methods in Physics Research Section A: Accelerators, Spectrometers, Detectors and Associated Equipment, 387, 250, new Developments in Photodetection

Jager, R., Mels, W. A., Brinkman, A. C., et al. 1997, Astronomy & Astrophysics Supplement, 125, 557

Johnson, W. N., Kinzer, R. L., Kurfess, J. D., et al. 1993, The Astrophysical Journal Supplement, 86, 693

Kanbach, G., Bertsch, D. L., Fichtel, C. E., et al. 1989, Space Science Reviews, 49, 69

Kluźniak, W. & Ruderman, M. 1998, The Astrophysical Journal Letters, 508, L113

Knoll, G. F. 2010, Radiation Detection and Measurement, 4th edn. (West Sussex PO19 8SQ, England: John Wiley & Sons, Inc.)

Kouveliotou, C., Meegan, C. A., Fishman, G. J., et al. 1993, The Astrophysical Journal Letters, 413, L101

Kuulkers, E., Ferrigno, C., Kretschmar, P., et al. 2021, INTEGRAL reloaded: spacecraft, instruments and ground system

Labanti, C., Amati, L., Frontera, F., et al. 2021a, The X/Gamma-ray Imaging Spectrometer (XGIS) on-board THESEUS: design, main characteristics, and concept of operation

Labanti, C., Amati, L., Fuschino, F., et al. 2021b, Requirement Specification-THS-INAF-XGIS-RS-0001, 3

Labanti, C., Di Cocco, G., Ferro, G., et al. 2003, Astronomy & Astrophysics, 411, L149

Labanti, C., Marisaldi, M., Fuschino, F., et al. 2006, in Society of Photo-Optical Instrumentation Engineers (SPIE) Conference Series, Vol. 6266, Society of Photo-Optical Instrumentation Engineers (SPIE) Conference Series, ed. M. J. L. Turner & G. Hasinger, 62663Q

Lebrun, F., Leray, J. P., Lavocat, P., et al. 2003, Astronomy & Astrophysics, 411, L141

Levan, A. 2018, Gamma-Ray Bursts, 2514-3433 (IOP Publishing)

Longair, M. S. 2011, High Energy Astrophysics, 3rd edn. (Cambridge University Press)

Lund, N., Budtz-Jørgensen, C., Westergaard, N. J., et al. 2003, Astronomy & Astrophysics, 411, L231

Mahant, A., Rao, P., & Misra, S. 1998, Nuclear Instruments and Methods in Physics Research Section A: Accelerators, Spectrometers, Detectors and Associated Equipment, 406, 117

Manzo, G., Giarrusso, S., Santangelo, A., et al. 1997, Astronomy & Astrophysics Supplement, 122, 341

Marchesini, E. J., Campana, R., Fuschino, F., et al. 2021, ORION Single Channel ASIC Test Report, Tech. Rep. THS-INAF-XGIS-TN-0010

Marchesini, E. J., Dilillo, G., Della Casa, G., et al. 2023

Marisaldi, M., Fuschino, F., Labanti, C., et al. 2010, Journal of Geophysical Research (Space Physics), 115, A00E13

Marisaldi, M., Labanti, C., & Soltau, H. 2004, IEEE Transactions on Nuclear Science, 51, 1916

Marisaldi, M., Labanti, C., Soltau, H., et al. 2005, IEEE Transactions on Nuclear Science, 52, 1842

Mas-Hesse, J. M., Giménez, A., Culhane, J. L., et al. 2003a, Astronomy & Astrophysics, 411, L261

Mas-Hesse, J. M., Giménez, A., Culhane, J. L., et al. 2003b, Astronomy & Astrophysics, 411, L261

Mazziotta, M. 2008, Nuclear Instruments and Methods in Physics Research Section A: Accelerators, Spectrometers, Detectors and Associated Equipment, 584, 436

Meegan, C., Lichti, G., Bhat, P. N., et al. 2009, The Astrophysical Journal, 702, 791

Mele, F., Dedolli, I., Gandola, M., et al. 2021, IEEE Transactions on Nuclear Science, 68, 2801

Mereghetti, S., Balman, S., Caballero-Garcia, M., et al. 2021, Experimental Astronomy, 52, 309

Meszaros, P. 2019, Mem. Societa Astronomica Italiana, 90, 57

Meszaros, P. & Rees, M. J. 1993, The Astrophysical Journal Letters, 418, L59

Mészáros, P. & Rees, M. J. 2001, The Astrophysical Journal Letters, 556, L37

Metzger, B. D. 2017, Living Reviews in Relativity, 20, 3

Metzger, B. D., Martínez-Pinedo, G., Darbha, S., et al. 2010, Monthly Notices of the Royal Astronomical Society, 406, 2650

Neamen, D. A. 2012, Semiconductor physics and devices : basic principles

O'Brien, P., Hutchinson, I., Lerman, H. N., et al. 2021, arXiv e-prints, arXiv:2102.08700

Oh, K., Koss, M., Markwardt, C. B., et al. 2018, The Astrophysical Journal Supplement Series, 235, 4

Parmar, A. N., Martin, D., Bavdaz, M., et al. 1996, in Roentgenstrahlung from the Universe, ed. H. U. Zimmermann, J. Trümper, & H. Yorke, 687–688

Pe'er, A. 2015, Advances in Astronomy, 2015

Pe'er, A. 2015, Advances in Astronomy, 2015, 907321

Perotti, F. & Fiorini, C. 1999, Nuclear Instruments and Methods in Physics Research A, 423, 356

Peter W. A., R. e. a. 2005, Space Sci.Rev., 120

Piran, T. 1999, Physics Reports, 314, 575

Piran, T. 2005, in American Institute of Physics Conference Series, Vol. 784, Magnetic Fields in the Universe: From Laboratory and Stars to Primordial Structures., ed. E. M. de Gouveia dal Pino, G. Lugones, & A. Lazarian, 164–174

Prest, M., Barbiellini, G., Bordignon, G., et al. 2003, Nuclear Instruments and Methods in Physics Research A, 501, 280

Ray W. Klebesadel, e. a. 1973, The Astrophysical Journal, 182

Roming, P. W. A., Kennedy, T. E., Mason, K. O., et al. 2005a, Space Science Reviews, 120, 95

Roming, P. W. A., Kennedy, T. E., Mason, K. O., et al. 2005b, Space Science Reviews, 120, 95

Schonfelder, V., Aarts, H., Bennett, K., et al. 1993, Astrophysical Journal Supplement Series

Singer, S., Aiello, W. P., Conner, J. P., & Kbebesadel, R. I. 1969, IEEE Transactions on Nuclear Science, 16

Tavani, M. 2002, 211

Tavani, M. 2019, Rendiconti Lincei. Scienze Fisiche e Naturali, 30, 13

Tavani, M., Bulgarelli, A., Piano, G., et al. 2009, Nature, 462, 620

Terrell, J. 1989, Journal of the British Interplanetary Society, 42, 309

Terrell, J., Fenimore, E. E., Klebesadel, R. W., & Desai, U. D. 1982, The Astrophysical Journal, 254, 279

Thompson, D. J. 2015, Comptes Rendus Physique, 16, 600, gamma-ray astronomy / Astronomie des rayons gamma

Tsoulfanidis, N. & Landsberger, S. 2021, Measurement and Detection of Radiation, 5th edn. (CRC Press)

Ubertini, P., Lebrun, F., Di Cocco, G., et al. 2003, Astronomy & Astrophysics, 411, L131

Ubertini, P. e. a. 1997, The Transparent Universe, Proceedings of the 2nd INTEGRAL Workshop held 16-20 September 1996, St. Malo, France. Edited by C. Winkler, T. J.-L. Courvoisier, and Ph. Durouchoux, European Space Agency, 1997., p.599

Vedrenne, G., Atteia, J.-L., & Cominsky, L. 2010, Gamma-Ray Bursts: The Brightest Explosions in the Universe, Vol. 63 (Springer)

von Kienlin et al., A. 2003, SPIE Conf. Proc., 4851, X-ray and Gamma-ray Telescopes and Instruments for Astronomy

Winkler, C., Courvoisier, T. J. L., Di Cocco, G., et al. 2003, Astronomy & Astrophysics, 411, L1

Wolter, H. 1952, Annalen der Physik, 445, 286

Woosley, S. E. 1993, in American Institute of Physics Conference Series, Vol. 280, Compton Gamma-ray Observatory, ed. M. Friedlander, N. Gehrels, & D. J. Macomb, 995–1002

Woosley, S. E. & MacFadyen, A. I. 1999, Astronomy & Astrophysics Supplement, 138, 499

Zhang, B., Fan, Y. Z., Dyks, J., et al. 2006, The Astrophysical Journal, 642, 354